

University of Nottingham
UK | CHINA | MALAYSIA

Modelling the Vibrational Spectroscopy of Carbon Nanomaterials

Pritesh M. Tailor, MSci

A thesis submitted for the degree of

Doctor of Philosophy

July 2018

Abstract

An empirical force-field based on the Murrell-Mottram potential is developed to model the vibrational spectroscopy of carbon nanomaterials. The resultant potential accurately simulates the structure and vibrational frequencies of carbon nanomaterials. When combined with the Empirical Bond Polarisability model it is able to simulate the Raman spectroscopy of single walled carbon nanotubes and graphene. A wide variety of systems are studied including the Raman spectroscopy of carbon nanotube junctions, nanocones and stone-wales defects. Three different approaches to model carbon nanomaterials are investigated, namely finite, periodic and tethered in simulations and their effect on computing the structure and vibrational properties of carbon nanomaterials is examined. The vibrational spectroscopy and properties of carbon nanotubes under strain is then studied and frequency-strain relationships are determined.

This new potential is then extended to model multi-layer carbon nanomaterials through the inclusion of dispersion interaction. The new potential is shown to accurately describe the structure and frequencies of few-layer graphene and graphite, and subsequently, multi-walled carbon nanotubes, carbon nanomotors and graphitic nanofibres are studied.

Publications

The work presented in this thesis has been published in part of the following refereed paper:

1. "An empirical force field for the simulation of the vibrational spectroscopy of carbon nanomaterials"
   Pritesh M. Tailor, Richard J. Wheatley and Nicholas A. Besley
   Carbon, 2017, **113**, 299-308.

2. "Simulation of the Raman spectroscopy of multi-layered carbon nanomaterials."
   Pritesh M. Tailor, Richard J. Wheatley and Nicholas A. Besley
   Phys. Chem. Chem. Phys., 2018, **20**, 28001-28010.

Acknowledgements

Firstly, I wish to express my gratitude and appreciation to my supervisors, Prof. Nicholas Besley and Dr. Richard Wheatley, for there help, guidance and unequivocal support throughout my PhD studies. In particular, Nick who gave me the opportunity to experience computational chemistry early on in my chemistry career, where he shared his interest and taught me about a field that was once foreign to me. Without no doubt, I would not have found my interest and enthusiasm in computational chemistry without his involvement.

Secondly, I would like to thank the Engineering and Physical Sciences Research Council (EPSRC) for funding the project, and to the University of Nottingham for access to their High-Performance Computing service.

Lastly, I would like to express my sincere gratitude to my family and friends who have endlessly supported and encouraged me throughout all my challenges both academic and personal, and without them, I would not be where I am today.

Contents

1 Introduction **2**

1.1 Nanotechnology 2

1.2 Principles of Raman Spectroscopy 5

1.3 Raman Spectroscopy of Carbon Nanomaterials 9

2 Theoretical Methods **16**

2.1 Empirical Potentials 16

2.1.1 Force-Field Methods 16

2.1.2 Empirical Potentials for Modelling Carbon 18

2.1.3 Murrell-Mottram Potential 21

2.2 Calculation of Vibrational Frequencies within the Harmonic Approximation 24

2.3 The Empirical Bond Polarisability Model 29

2.4 Kohn-Sham Density Functional Theory 32

2.5 Software Implementation 41

3 An Empirical Force Field for the Simulation of the Vibrational Spectroscopy of Carbon Nanomaterials **46**

3.1 Introduction 47

3.2 Development of Force-Field, Random Search Parameterisation 51

3.3 Results 56
3.3.1 Structure 56
3.3.2 Experiment Vs Theoretical 57
3.3.3 Radial Breathing Mode 61
3.3.4 G-Band Modes 65
3.3.5 Vibrational Density of States 69
3.3.6 Graphene 71
3.3.7 Stone-Wales Defects 72
3.3.8 Carbon Nanotube Junctions 78
3.3.9 Carbon Nanocones 82
3.3.10 Conclusions 86

4 Modelling Methods: Periodic, Finite or Tethered? 87

4.1 Introduction 87
4.2 Nanotubes 90
4.3 Graphene 101
4.4 Conclusion 105

5 Strained Nanotubes 107

5.1 Introduction 107
5.2 Zig-Zag and Armchair Nanotubes 111
5.3 Chirality 114
5.4 Vibrational Density of States 116
5.5 Conclusions 118

6 Modelling of Multi-Layer Carbon Nanomaterials 119

6.1 Introduction 119
6.2 Modelling Dispersion Interaction 121

6.3 Development of Dispersion Parameters, Random Search Parametrisation 124
6.4 Few-Layer Graphene 127
6.5 Multi-Wall Carbon Nanotubes 129
6.6 Coaxial Nanomotor 140
6.7 Graphitic Nanofibres 145
6.8 Conclusions 151

7 Concluding Remarks and Future Directions 153

Chapter 1

Introduction

In this section an overview of the main background and origins of nanotechnology is given, the theory of Raman spectroscopy as a tool for investigating molecular and material properties is presented and an introduction to carbon nanomaterials focusing on their structure and vibrational spectroscopy.

1.1 Nanotechnology

Since Richard Feynman's lecture in 1959, "There's plenty of room at the bottom: An invitation to enter a new field of physics" [1] the idea of miniaturisation he introduced has evolved into nanotechnology. The prefix *nano* in the metric scale is 10^{-9} meters, a level at where we look at materials from the atomic and molecular perspective. Today, nanotechnology has become a leading scientific field in both academic research and industry. This is because it combines knowledge from the fields of Physics, Chemistry, Biology, Medicine, Informatics, and Engineering.

Nanoscale science exploits and utilises phenomena, properties, and re-

sponses of nanoscale objects and materials. The range of sizes generally lie between 1 and 100 nm and at these scales, particularly below 5 nm, the properties of matter can differ significantly from its bulk state owing to quantum-scale effects, which can play an important role in its properties. Hence the goals of nanotechnology include the design, manipulation, building and production as well as the development of nanoscale materials and their applications through controlling the shape and size, response properties and functionality of these structures. The assembly of such materials will allow us to form electronic and mechanical devices on the order of less than 100 nm.

Nanotechnology is an emerging technology that has the possibility to advance the existing base of well-established products. It presents the capability to create a plethora of new 21^{st} century devices with totally new characteristics and functions with enormous potential in a wide range of applications. Advanced nanoscale materials are expected to have a huge and long-term impact on human life in the future through not just scientific breakthroughs, but also economical, ethical and societal aspects. Nanotechnology research will likely continue into the future and lead to new levels of knowledge of materials at such small scales. This new understanding will undoubtedly enable us to bridge the link between man-made materials and nature. At the nanoscale, humans have only had the last hundred years or so, whereas nature has had millions to master the art of efficiency, functionality and operation at the nanoscale to fully exploit it. Hence much of the inspiration and drive in nanotechnology comes from the natural world around us.

The future of nanotechnology is becoming more promising from its various industrial uses, great innovations are foreseen in information and communication technology, biology and biotechnology, medicine and medical technology and metrology to name a few. Significant applications of nanosciences and nanoengineering lie in the fields of pharmaceutics, cosmetics, processed food, chemical engineering, high-performance materials, electronics, precision mechanics, optics, energy production, and environmental sciences. It has the potential to revolutionise many commercial technologies including many day-to-day products like metals, ceramics, polymers, smart textiles, cosmetics, sunscreens, electronics, paints and varnishes.[2]

Nanotechnology is clearly a science with huge potential and great expectations. Nanomaterials bring new possibilities for tailoring the optical, electronic, mechanical, chemical and magnetic properties. In order for nanotechnology to reach its full potential, the capability to characterise these complex nanosystems is required. Highly sophisticated nanoscale precision metrology tools are required to achieve this. The advances in nanomaterials necessitate parallel progress of the nanometrology tools and techniques in both experimental and theoretical approaches. Examples of important nanometrology tools include spectroscopic and microscopic techniques such as Raman spectroscopy,[3] X-ray photo-electron spectroscopy,[4] scanning probe microscopy[5] and transmission electron microscopy.[6] The continued development of these methods has led to better spectral and spatial resolution, contrast and sensitivity for elements and molecular species, with capabilities to work in situ, at ambient air and/or in liquid surround-

ings.[7–9] Alongside this, theoretical treatment of these techniques are essential to enable in-depth interpretation and assignment of features and processes observed in experimental spectra and micrographs.

The work presented in this thesis focuses on the theoretical treatment and simulations of carbon nanomaterials. In particular, models to simulate the Raman spectroscopy of carbon nanomaterials to aid in the characterisation and understanding of this widely investigated class of nanomaterials. These materials have many potential applications including conductive and high-strength composites; energy storage and energy conversion devices; sensors; field emission displays and radiation sources; hydrogen storage media; and nanometer-sized semiconductor devices.[10]

1.2 Principles of Raman Spectroscopy

Raman spectroscopy[11] is one of the most important and widely used analytical techniques in chemistry and materials science. It is primarily used to obtain chemical information on the structure and bonding in materials. It is a technique in which many forms of a sample can be studied from solids, powders and surfaces to solutions, liquids and gases. It also has the ability to interrogate materials under a range of conditions such as varying temperature and pressure. Consequently, this technique has found a variety of uses across many scientific fields.

In Raman spectroscopy, an incident photon of a single colour (frequency) is scattered by a material. Most of the light is elastically scattered off with no change in colour (Rayleigh scattering), but a small fraction

is inelastically scattered with a slightly different colour and this is known as Raman scattering. This originates from either a decrease in frequency called a Stokes Raman scattering (if the light loses energy to the material) or from an increase in frequency (if the light gains energy from the material) called an anti-Stokes Raman scattering. The process can be regarded as taking place by an excitation of the material to a wide range of higher energy virtual states and the subsequent return of the material to a lower state; the net energy change is then carried away by the photon that is scattered and observed.

At the atomic level, we can interpret the Raman effect as the interaction of the electric field of the incident light, distorting and polarising a molecule or material's electron cloud, inducing a dipole moment, causing it to undergo transitions to a higher energy "virtual state". Raman scattering results in the release of a scattered photon with a different energy to the incident photon; the difference in energy is equal to the discrete vibrational transitions a molecule or material can undergo. The transitions accompanying Rayleigh and Raman scattering mechanisms are illustrated in figure 1.1. It is important to note in the Raman mechanism that light is scattered not absorbed and the molecule is never excited to a higher electronic state, and the "virtually excited" description is a misrepresentation of the process. This can often lead to confusion between the difference between fluorescence and Raman. The key difference can be easily proven experimentally whereby fluorescence can be quenched whereas Raman scattering cannot since a molecule never absorbed the light to be in an excited state.

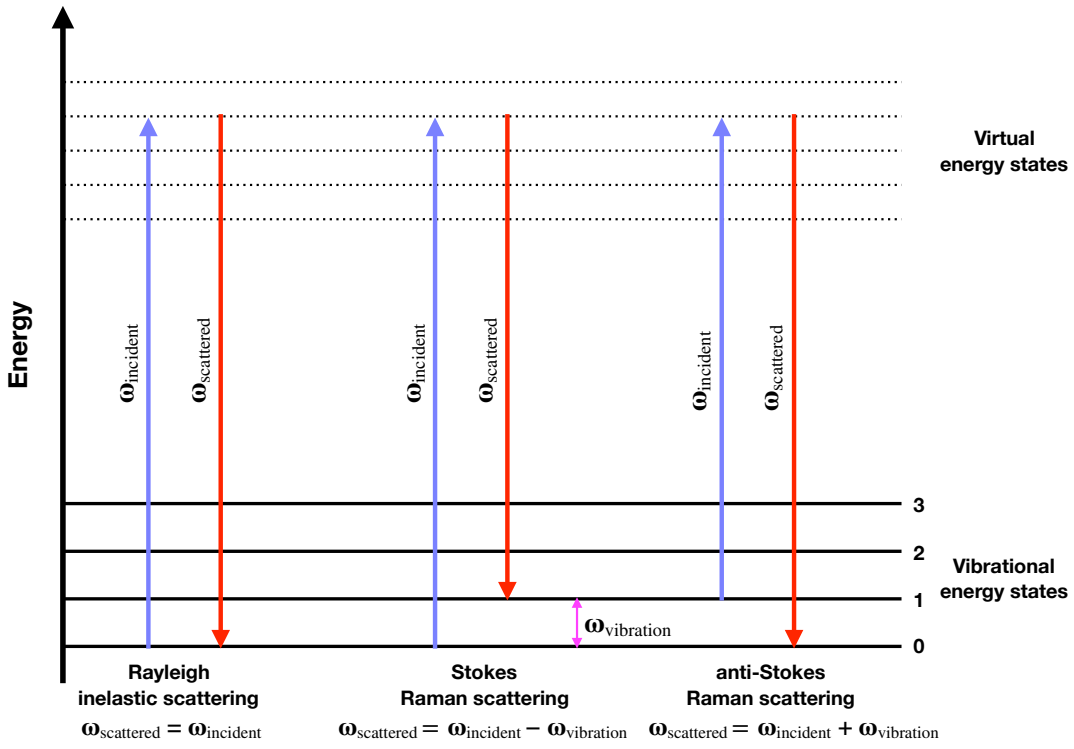


Figure 1.1: The different possibilities of light scattering: Rayleigh scattering (no exchange of energy: incident and scattered photons have the same energy), Stokes Raman scattering (atom or molecule absorbs energy: scattered photon has less energy than the incident photon) and anti-Stokes Raman scattering (atom or molecule loses energy: scattered photon has more energy than the incident photon).

A Raman spectrum is usually measured as a function of frequency (or Raman shift) with an associated intensity. The shifts in the frequencies of the Raman scattered light is characteristic of the system being measured and hence by plotting the intensity of this "shifted" light against frequency, a Raman spectrum is generated (an example is shown in figure 1.2), providing a unique fingerprint enabling the characterisation of materials. At room temperature, the thermal population of vibrationally excited states is

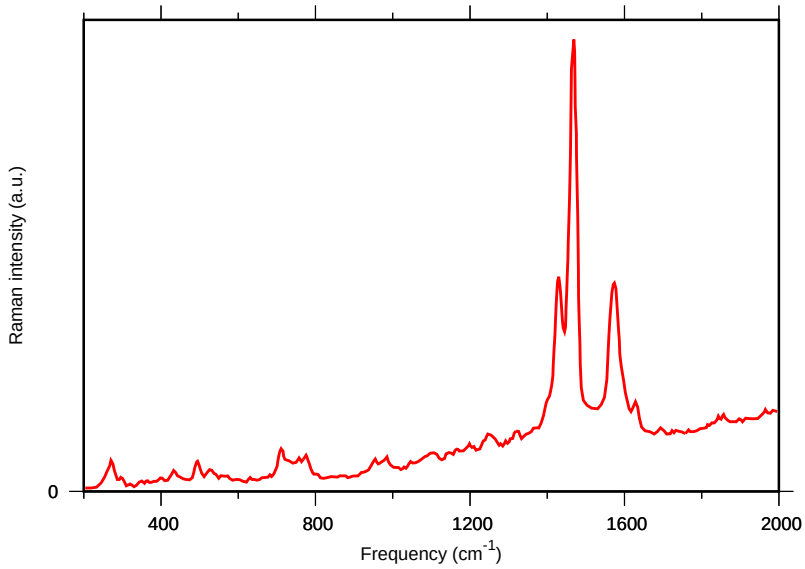


Figure 1.2: An example Raman spectrum of a C_{60} film.[12]

normally low. Therefore, the initial state is usually the ground vibrational state, and the scattered photon will have lower energy than the exciting photon. This Stokes shifted scattering is what is usually observed in Raman spectroscopy experiments.

The intensity of a Raman vibrational transition depends on the corresponding vibrational mode and the change in polarisability during its vibrational mode coordinate. More quantitatively, the Raman intensity of a mode is proportional to the square of the derivative of polarisability, $\boldsymbol{\alpha}$ with respect to the vibrational mode coordinate, $\mathbf{q}$.

$$I_{Raman} \propto \left(\frac{\partial \boldsymbol{\alpha}}{\partial \mathbf{q}} \right)^2 \tag{1.1}$$

Hence only vibrations with an associated change in polarisability will be observed in Raman spectroscopy. Raman spectroscopy is a complemen-

tary technique to infrared spectroscopy where vibrational modes associated with a change in dipole moment are observed. Consequently, Raman spectroscopy can probe vibrational modes that are IR inactive. The frequency of the vibrational transitions depends on the mass of the atoms involved in the vibration and the strength of the bonds involved, providing insight into structure and bonding in materials as well as information about the environment and its effect on the system of interest.

1.3 Raman Spectroscopy of Carbon Nanomaterials

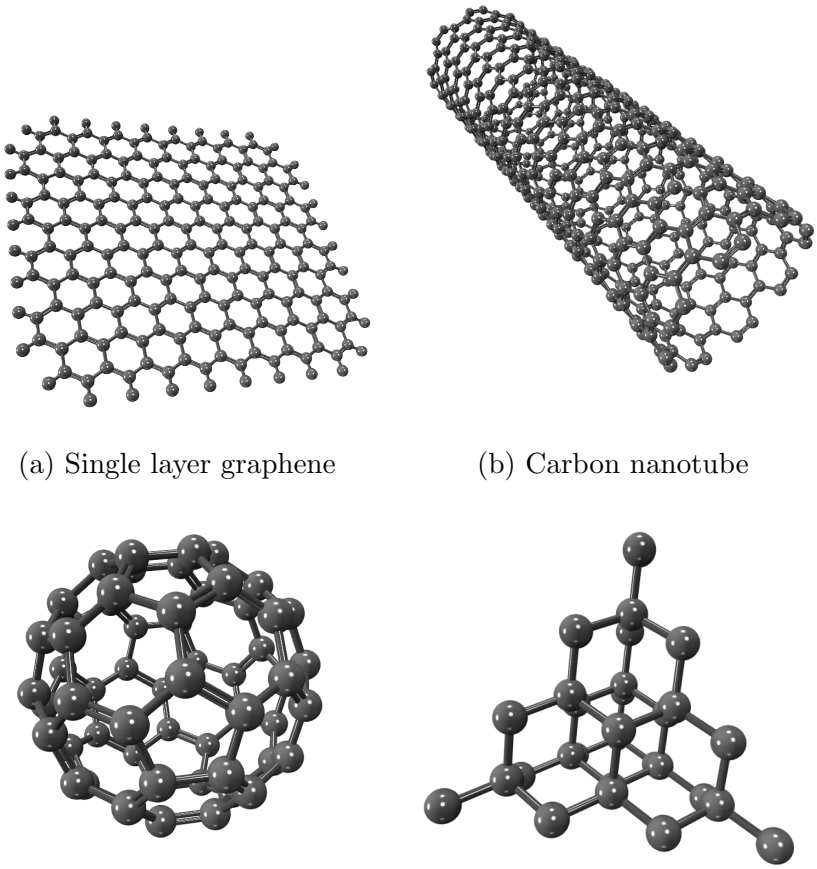
In recent years carbon nanomaterials have revolutionised the field of material science and this has been recognised by Nobel prizes in two separate fields. The first award was the Nobel prize in chemistry in 1996 for the discovery of fullerenes,[13] and more recently the 2010 Nobel prize in physics for groundbreaking experiments regarding the two-dimensional material graphene.[14] Carbon occurs in many forms and the dependence of its properties on each form is linked to the special and unique structure it adopts, making carbon a truly versatile building block for nanomaterials. The reason carbon has this nature originates from its distinct types of valence bonding modes it can take part in, referred to as hybridisation states from a chemist's perspective. For this reason, carbon has been investigated for more than half a century without exhausting novel science and challenges. With the dawn of nanoscience, the search for new properties for carbon nanostructures tailored for modern applications has become increasingly important. Individual carbon nanomaterials offer a wide range of useful

properties, for example, electrical conductance, thermal resistance, and exceptional strength, making them very interesting materials for use in a broad range of industries and disciplines for applications in the physical sciences and engineering.

The high-level of interest in the processing, modification, and customisation of these carbon materials has created a strong demand for techniques that can be used to characterise them. Raman spectroscopy is a method well suited to characterise key elements of these materials. Raman is very sensitive to highly symmetric covalent bonds with little or no natural dipole moment. The carbon-carbon bonds that make up these materials fit this criterion perfectly and as a result, Raman spectroscopy is highly sensitive to these materials and able to provide a wealth of information about their structure, bonding and environments as well providing non-equilibrium properties.

Raman spectroscopy has played an important role in the study and characterisation of graphitic materials, historically it has been widely used over the last four decades to characterise pyrolytic graphite, carbon fibres,[15] glassy carbon, pitch-based graphitic foams,[16,17] nanographite ribbons,[18] fullerenes,[19] carbon nanotubes[20,21] and graphene.[22] A major advantage of Raman spectroscopy that has allowed its broad application is that it's a non-destructive and contactless measurement.

There are a wide variety of different carbon nanostructures possible, all of these materials are made up of pure carbon and are referred to as



(a) Single layer graphene

(b) Carbon nanotube

(c) Fullerene

(d) Diamond

Figure 1.3: Representative structures of some carbon allotropes.

allotropes. The range of these structures starts with the well-known diamond and graphite, and continues on to encompass fullerenes, graphene and carbon nanotubes (see figure 1.3) as well as their multi-layer (or few-layer analogues) such as multi-wall carbon nanotubes (see figure 6.1).

The focus of this thesis is carbon materials comprised of sp^2 nanocarbons such as graphene and carbon nanotubes. Raman spectroscopy can give information about size, clustering of the sp^2 phase, the presence of sp^2-sp^3 hybridisation and the presence of chemical impurities, elastic constants, defects and other crystal disorder properties, edge structure, strain,

number of graphene layers, nanotube diameter, chirality, curvature, and finally determine the metallic vs semiconducting behaviour. Hence Raman has become an indispensable and routinely used tool for the study of these materials.

To understand the link between structure and the Raman spectroscopy of sp^2 carbon nanomaterials it is important to first define and understand the geometrical properties and structures of these systems. Graphene is a 2-dimensional single carbon layer in a honeycomb lattice arrangement with a planar hexagonal network of carbon atoms based on purely sp^2 bonding. If we stack up sheets of graphene, we get its bi-, tri-, few-layer analogues and eventually 3-dimensional graphite are formed. Alternatively, rolling up a single graphene sheet leads to the formation of 1-dimensional carbon nanotubes which are seamless cylinders of graphene with nanometer-size diameters and can consist of single or concentric multi-layers. The bonding in carbon nanotubes has some sp^3 character owing to the curvature in the tubular structure. Subsequently, this leads to topological constraints in the circumferential direction, and the small amount of sp^3 bonding causes the force constant in the circumferential direction to be slightly weaker than along the nanotube axis.

Although the basic shape of a carbon nanotube is cylindrical, we need two indices (n, m) to fully identify and characterise a carbon nanotube. The rolling of a single graphene layer into an idealised single-walled carbon nanotube can be viewed as being formed by rolling up a graphene sheet along the chiral vector (n, m), where n and m are numbers of the two lattice

vectors a_1 and a_2 of graphene needed to construct the chiral vector, C_h, see figure 1.4. The chiral vector, C_h, is given by,

$$C_h = na_1 + ma_2 \tag{1.2}$$

The length of C_h equals the circumference of the resulting single walled

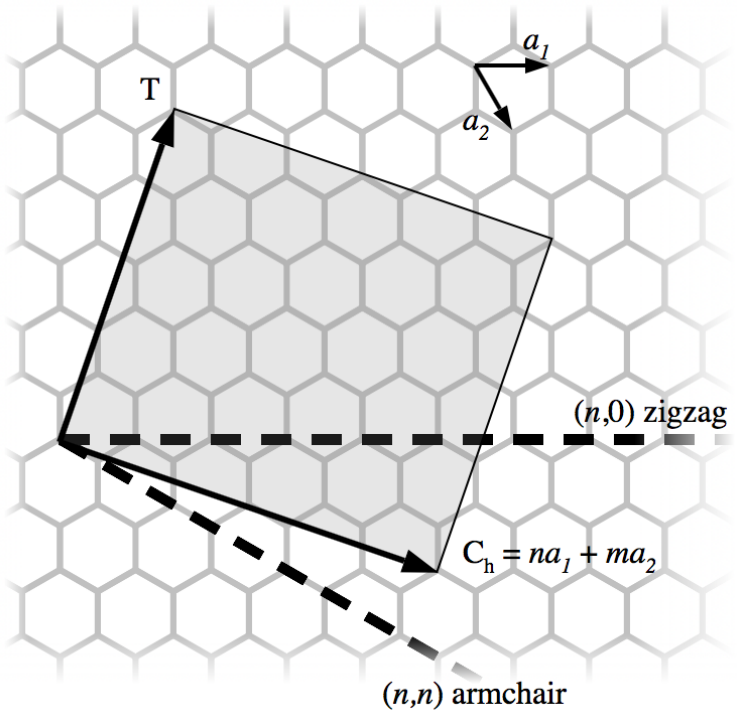


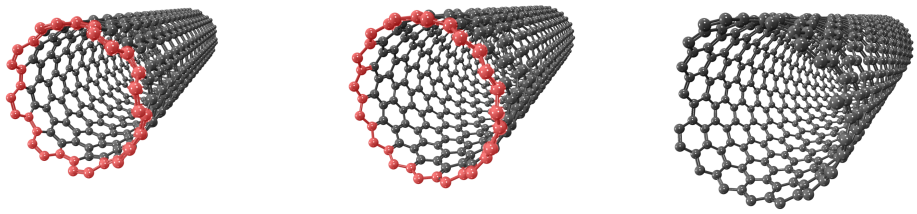
Figure 1.4: The chiral vector of a (6,2) single-walled carbon nanotube. Rolling up the graphene sheet along this chiral vector forms the chiral (6,2) nanotube. The translational vector, T, is perpendicular to the chiral vector. The two lattice vectors of graphene, a_1 and a_2, are also shown. The achiral nanotubes (n, n) and $(n, 0)$ are commonly referred to as armchair and zig-zag nanotubes, respectively.

carbon nanotube. Thus, the carbon nanotubes's diameter d is given by:

$$d = \frac{|C_h|}{\pi} = \frac{a_0}{\pi}\sqrt{n^2 + nm + m^2} \tag{1.3}$$

Here, $a_0 = 2.46$ Å, which is the lattice constant of the graphene honeycomb

lattice. All physical properties of a given carbon nanotube ultimately depend on the two numbers n and m, and different atomic structural motifs result from various choices. The translational vector (T) is perpendicular to the chiral vector and thus parallel to the tube axis. The two-dimensional symmetry of graphene means that (n, m) is equivalent to (m, n), therefore by convention n is always set larger than or equal to m. Depending on the values of n and m, single wall carbon nanotubes can be achiral or chiral: (n, n) have armchair edges and $(n, 0)$ have zig-zag edges and both of these nanotube types are achiral. General carbon nanotubes of the form $n > m > 0$ are chiral, examples of these structures are shown in figure 1.5.



(a) Armchair $(8, 8)$ (b) Zig-zag $(0, 15)$ (c) Chiral $(15, 3)$

Figure 1.5: Example structures of achiral and chiral carbon nanotubes.

The (n, m) indices of a carbon nanotube, can be also used to characterise their electronic structure, where for metallic tubes, the indices satisfy $(n - m = 3q)$ where q is integer values including 0 and for semiconducting, q, takes non-integer values. Likewise, the individual constituents of multi-wall nanotubes or single-wall nanotube bundles can be metallic or semiconducting as well.

Raman spectroscopy is an ideal probe to interrogate carbon nanomaterials in order to characterise the structural and electronic properties of

a carbon nanotube and graphene. Key modes in the Raman spectroscopy of carbon nanotubes and graphene are the G-band, D-band and the radial breathing mode (RBM) (only in carbon nanotubes). The G-band arises from planar vibrations of the carbon atoms and is the most intense band, and is present in both graphene and carbon nanotubes. For carbon nanotubes this band can split into the G^+ and G^- bands, which correspond to in-plane movements along and perpendicular to the carbon nanotube axis. The G-band can be used to determine whether a carbon nanotube is metallic or semiconducting, and allows for the qualitative assignment of the chiral indices of a carbon nanotube. The RBM corresponds to the coherent expansion and contraction of carbon atoms in the radial direction, and the frequency of this mode is known to depend on the diameter of the carbon nanotube. A further very weak band is the disorder-induced D-band, which is associated with sp^3 defects and its intensity can be linked to defect disorder.[23] The visual representations and details of these modes are given in chapter 3.

Chapter 2

Theoretical Methods

This chapter introduces the background to the theoretical and computational methods utilised and applied in this thesis. This includes a description of empirical potentials including existing carbon-carbon potentials with a focus on the Murrell-Mottram Potential, the calculation of vibrational frequencies, the empirical Bond Polarisabilty Model and density functional theory. The information in this chapter has been based on a number of sources, including *Introduction to Computational Chemistry* by F. Jensen[24] and *Essentials of Computational Chemistry* by C. Cramer.[25] Following this, a section detailing the implementation of these theories is presented including the algorithms and software logistics.

2.1 Empirical Potentials

2.1.1 Force-Field Methods

In order to study the spectroscopy of molecules and materials, we need to accurately describe how atoms in molecules and materials interact. This is commonly achieved using quantum chemical methods. However, these

types of methods are of high complexity are too computationally expensive to be applied carbon nanomaterials due to the extremely large system sizes in both time and computational requirements. Alternatively, in the context of vibrational spectroscopy, we can purely describe the way atoms interact using force-field methods with a simplified model, which enables us to model these large systems at the fraction of the computational cost and complexity in quantum chemical methods.

Force-field methods employ empirical potentials to provide a convenient and computationally inexpensive route to model the energy of a given nuclear configuration. This provides access to the potential energy surface, bypassing the need to solve the Schrödinger equation. This is achieved by approximating the potential between atoms with parametric functions of the nuclear coordinates and fitting the parameters to experimental or high-level computational data. In these potential models, systems are made of only atoms and electrons are not considered explicitly. Consequently, the parameters chosen for the empirical potentials must explicitly describe the bonding and behaviour between atoms as opposed to being a natural result of solving the electronic Schrödinger equation.

Through the use of empirical potentials it is possible to computationally study the structural and chemical phenomena of large complex systems. This includes the effects of finite temperature by means of statistical mechanics allowing the exploration of the potential and hence thermodynamics, which are currently inaccessible to large systems through quantum mechanical methods. Most notably, three key simulation scenarios are en-

abled:

- Static analysis of a potential energy surface by locating the minima and saddle points. This corresponds to modelling the system at a temperature of 0 K, where systems are in their ground electronic, vibrational and rotational states. This allows "static" properties to be analysed such as structural parameters, conformational energy barriers and normal mode analysis.

- Molecular dynamics simulations, which enables us to predict the motion and study the time evolution of a large number of atoms in real time. This method requires numerical integration of Newton's equations of motion, enabling us to study materials and biological systems for up to several nanoseconds, under a variety conditions.

- Monte-Carlo simulations, which generate random configurations with a Metropolis selection procedure ensuring that a proper Boltzmann ensemble is generated. This surveys the potential independently of time. Indeed, it is not suitable for studying time-dependent phenomena or properties depending on momentum but it overcomes the issue of becoming trapped in energy wells within molecular dynamics simulations.

2.1.2 Empirical Potentials for Modelling Carbon

Empirical potentials for describing carbon-carbon interactions are amongst several of the most highly developed and most used across chemistry and material science. The potentials developed for carbon followed two dis-

tinct strategies to describe its complex interactions. The first is through many-body expansions of the potential by describing successive orders of interactions (two-body, three-body,...) and secondly through the use of bond order formalisms. Each of these methods has their own advantages and disadvantages in simulation and accuracy and are suited to different applications.

Currently, the most popular of potentials for carbon include firstly the Reactive Bond Order Potential (REBO) developed by Brenner *et al.*[26] and its successor Adaptive Intermolecular REBO potential[27] (AIREBO), and secondly the Reactive Force-Field by Van Duin *et al.*[28] These potentials describe the hybridisation states of carbon as well as accounting for bond formation and dissociation, subsequently, this allows for the modelling of chemical reactions. The REBO interaction potential can be summarised by the following equation:

$$E_b = \sum_i \sum_{j>i} [V_R(r_{ij}) - b_{ij} V_A(r_{ij})] \tag{2.1}$$

$V_R(r_{ij})$ and $V_A(r_{ij})$ are pair-additive repulsive and attractive interactions that represent all interatomic repulsion and attraction from valence electrons, respectively. The quantity r_{ij} is the distance between pairs of nearest-neighbour atoms i and j, and b_{ij} is the bond order between atoms i and j. $V_R(r_{ij})$, $V_A(r_{ij})$, and b_{ij} take to the following form,

$$V_R(r_{ij}) = f^c(r_{ij})\Big(1 + \frac{Q}{r_{ij}}\Big) A e^{(-\alpha r_{ij})} \tag{2.2}$$

$$V_R(r_{ij}) = f^c(r_{ij}) \sum_{n=1,3} B_n e^{(-\beta_n r_{ij})} \tag{2.3}$$

and,

$$b_{ij} = \frac{1}{2}(b_{ij}^{\sigma-\pi} + b_{ji}^{\sigma-\pi} + \Pi_{ij}^{RC} + b_{ij}^{DH}) \tag{2.4}$$

$$b_{ij}^{\sigma-\pi} = \left(1 + \sum_{k \neq i,j} f_{ik}^{c}(r_{ik}) g_{ijk}(\theta_{ijk})\right)^{-\frac{1}{2}} \tag{2.5}$$

Where $f^c(r_{ij})$ is a cut-off function, Q, A and α are fitted parameters for the pairwise repulsive interactions. B_n and β_n are fitted parameters for the pair wise attractive interaction from different hybridisation states i.e. molecular triple, double and single bonds, and hence the sum of $n = 1, 3$. b_{ij} is designed to describe changes in atomic hybridisation. $g_{ijk}(\theta_{ijk})$ is a bond-bending spline function dependant on angle, θ_{ijk} and the Π_{ij}^{RC} term is relevant for radicals and is zero for closed shell systems. b_{ij}^{DH} is a dihedral bending function that depends on the local conjugation and involves the third nearest neighbour atoms.

$$b_{ij}^{DH} = \frac{T_{ij}}{2} \sum_{k,l \neq i,j} f_{ik}^{c}(r_{ik}) f_{jl}^{c}(r_{jl})(1 - \cos^2[\Theta_{ikjl}]) \tag{2.6}$$

Here Θ_{ijkl} is the dihedral angle of four atoms and T_{ij} describes the rotation about the bonds and depends whether the atoms are conjugated. There are many parameters incorporated in the REBO potential which are described in more detail elsewhere.[26]

By adopting bond order formalisms, where the bond order is empirically determined from the interatomic distances, angles and torsions, the parameterised bond order function is used to introduce many-body effects, chemical bonding and hybridisation effects. Hence the interactions driving chemical bonding are treated implicitly, enabling these methods to simulate reaction chemistry without explicit quantum mechanical calculation.

These potentials are primarily designed with specific types of applications in mind. Indeed the success in these applications comes from the

ability to describe large-scale processes which involve reactions with bond formation, dissociation and changes in hybridisation; properties dependant on the accuracy of the forces and energetics. Such processes include fracture stress in graphene sheets,[29] radiation and thermal damage on carbon nano-structures[28] and as well simulating the effects of ion irradiation damage.[30]

The second set of potentials are those based on many-body expansions of the energy such as the TLHT potential of Takei *et al.*[31] and the Murrell-Mottram potential of Eggen *et al.*[32] The form of these potentials includes two-body and three-body interactions with higher-order contributions to the energy being assumed to be negligible. These potentials have been fitted to the experimental structural and energetic properties as well as vibrational frequencies and elastic constants. Potentials of these form tend to be much simpler and less sophisticated compared with their bond-order counterparts. As a result, they are easier to fit to data and implement in practice. These types of potentials have been used with the goal of simulating the structure and energetic properties as well as the vibrational properties. The above potentials have been applied to simulate bulk properties of diamond and graphite, as well as small carbon clusters.[32]

2.1.3 Murrell-Mottram Potential

The Murrell-Mottram (MM) potential[33] seeks to represent the interaction between atoms through the sum of two-body and three-body contributions to the energy. For a system of N atoms, the potential takes the following

form:

$$E = \sum_{i}^{N} \sum_{j=i+1}^{N} V_{ij}^{(2)} + \sum_{i}^{N} \sum_{j=i+1}^{N} \sum_{k=j+1}^{N} V_{ijk}^{(3)} \tag{2.7}$$

where,

$$V_{ij}^{(2)} = -D(1 + a_2\rho_{ij}) \exp(-a_2\rho_{ij}) \tag{2.8}$$

$$V_{ijk}^{(3)} = DP(Q_1, Q_2, Q_3) \exp(-a_3 Q_1) \tag{2.9}$$

$$\rho_{ij} = (r_{ij} - r_e)/r_e \tag{2.10}$$

The two-body potential $V_{ij}^{(2)}$ is represented by a Rydberg function, where r_{ij} is the distance between atoms i and j. D and r_e are parameters for describing the energy and ground state structures accurately. The terms $\exp(-a_2\rho_{ij})$ and $\exp(-a_3 Q_1)$ are damping functions which are controlled by parameters a_2 and a_3 and ensure the potential converges to zero energy at infinite interatomic separation. $P(Q_1, Q_2, Q_3)$ is a quartic polynomial made up of products and sums of symmetrical Q_i coordinates to describe the three-body interactions in monatomic solids:

$$Q_1 = \frac{1}{\sqrt{3}}(\rho_{ij} + \rho_{ik} + \rho_{jk}) \tag{2.11}$$

$$Q_2 = \frac{1}{\sqrt{2}}(\rho_{ij} + \rho_{ik}) \tag{2.12}$$

$$Q_3 = \frac{1}{\sqrt{6}}(2\rho_{ij} - \rho_{ik} - \rho_{jk}). \tag{2.13}$$

The term Q_1 describes the perimeter of the interaction triangles and Q_2 and Q_3 describe the distortions of the triangles from being equilateral. $P(Q_1, Q_2, Q_3)$ takes the form of:

$$\begin{aligned} P(Q_1, Q_2, Q_3) &= c_0 + c_1 Q_1 + c_2 Q_1^2 + c_3(Q_2^2 + Q_3^2) + c_4 Q_1^3 + c_5 Q_1(Q_2^2 + Q_3^2) \\ &+ c_6(Q_3^3 - 3Q_3 Q_2^2) + c_7 Q_1^4 + c_8 Q_1^2(Q_2^2 + Q_3^2) \\ &+ c_9(Q_2^2 + Q_3^2) + c_{10} Q_1(Q_3^3 - 3Q_3 Q_2^2) \end{aligned} \tag{2.14}$$

with parameters c_0 to c_{10} to be determined for the potential.

The MM potential has been widely applied, and parameters developed to study a wide variety of materials including metallic and non-metallic elements across the periodic table. Metallic elements include but not limited to aluminium, lithium, iron and gold and non-metallic include silicon, carbon, germanium and tin. These have been applied to study several properties of solids including relative stabilities and phase transitions, further studies have looked at surface phenomena such as relaxation and reconstructions as well as the structure, dynamics and growth of clusters. A comprehensive review can be found elsewhere by Murrell and Cox *et al.*[34]

The MM potential was chosen to be used in this work as opposed to the more complex and popular bond order potentials like REBO, AiREBO and Reaxxff. This is because of multiple reasons. The practicality of calculating and implementing second derivatives of the MM potential is much simpler, whereas for bond orders potentials like REBO a piecewise derivative of splines need to be defined as an example. Secondly, fitting coefficients is simpler compared to bond order potentials where they need to be defined for bond order and hybridisation states as well as interaction coefficients and cut-offs for neighbouring lists, to name a few. Thirdly, with a simpler potential form, parallelism in computing energies and derivatives can be easily implemented allowing larger scale simulations. Overall, the MM potential provides an ideal framework with a balance of complexity and practically to achieve the accuracy desired in this study. It enables effective fitting of the potential, easy access to analytical derivatives and

hence efficient calculations of properties.

2.2 Calculation of Vibrational Frequencies within the Harmonic Approximation

To evaluate vibrational frequencies we adopt the quantum harmonic oscillator model, the quantum analogue of the classical harmonic oscillator. Within the classical model, the total energy in the system changes between potential and kinetic energies as the system vibrates. The total energy in the system remains constant and depends only on the spring constant (Hooke's law). This same idea can be used in the context of molecules since an arbitrary potential curve, $V(x)$, (in this case the MM potential) can usually be approximated as a harmonic potential in the vicinity of stationary points corresponding to stable molecular structures and the bonds as harmonic springs. Furthermore, it is one of the few quantum-mechanical systems for which an exact, analytical solution exists. Solving more complex potentials typically requires either complex approximations or numerical approaches to identify the corresponding eigenstates and eigenvalues (i.e., wavefunctions and energies or normal mode vibrations and vibrational frequencies).

The simplest case to demonstrate the model is through a diatomic molecule, where a general potential energy curve can be expanded as a Taylor series in the vicinity of the equilibrium structure where x_0 is the

equilibrium bond length:

$$V(x) = V(x_0) + \left.\frac{dV(x)}{dx}\right|_{x_0}^{x} (x - x_0) + \frac{1}{2!}\left.\frac{d^2V(x)}{dx^2}\right|_{x_0}^{x} (x - x_0)^2 + ... + \frac{1}{n!}\left.\frac{d^nV(x)}{dx^n}\right|_{x_0}^{x} (x - x_0)^n \quad (2.15)$$

Within the harmonic approximation we truncate this expansion at the quadratic term or second order, leaving:

$$V(x) = V(x_0) + \left.\frac{dV(x)}{dx}\right|_{x_0}^{x} (x - x_0) + \frac{1}{2!}\left.\frac{d^2V(x)}{dx^2}\right|_{x_0}^{x} (x - x_0)^2 \quad (2.16)$$

Where the term $V(x_0)$ is constant, and $\left.\frac{dV(x)}{dx}\right|_{x_0}^{x} (x - x_0)$ is equal to zero since we assume we are at an equilibrium structure where the forces equal zero. Consequently, $V(x)$ becomes,

$$V(x) = \frac{1}{2!}\left.\frac{d^2V(x)}{dx^2}\right|_{x_0}^{x} (x - x_0)^2 \quad (2.17)$$

The energy constant $V(x_0) = 0$ and displacement $x = x - x_0$ and hence the harmonic force constant with respect to cartesian nuclear displacement x, where $k = \frac{d^2V(x)}{dx^2}$, we can simply write:

$$V(x) = \frac{1}{2}kx^2 \quad (2.18)$$

It is important to note that this approximation is most valid for areas in the vicinity of x_0. This is suitable since we consider that most chemical systems of interest are at sufficiently low temperatures that their lowest vibrational levels are occupied where the harmonic approximation is most applicable. The harmonic approximation represents a vast simplification and neglects the true anharmonic nature of bonds. In reality, chemical bonds dissociate as they are stretched longer and the spacing between vibrational levels decreases with increasing quantum number, whereas the harmonic oscillator has an infinite number of levels which are all equally

spaced.

Once the harmonic potential in equation 2.18 is obtained we then utilise this potential to solve the nuclear Schrödinger equation assuming the Born-Oppenheimer approximation (in a.u.):

$$\left[-\frac{1}{2\mu}\frac{\partial^2}{\partial x^2}+\frac{1}{2}kx^2\right]\Xi(x)=E\Xi(x) \tag{2.19}$$

Where μ is the reduced mass, Ξ the wavefunction and E is the total energy. The solutions to this equation allow us to calculate vibrational energy levels and the associated wavefunctions which are products of Hermite polynomials and Gaussian functions. The vibrational energy levels are given by,

$$E_n=(n+\frac{1}{2})h\omega \tag{2.20}$$

where n is the vibrational quantum number and the vibrational frequency, ω are related to the force-constant by

$$\omega=\frac{1}{2\pi}\sqrt{\frac{k}{\mu}} \tag{2.21}$$

In the harmonic oscillator model transitions are only allowed for $\Delta n = \pm 1$ and as indicated by equation 2.20, all energy levels are equally spaced. Hence all that is needed to evaluate the harmonic frequencies is the second derivatives of the potential energy with respect to the nuclear displacement, k.

For the case of polyatomic molecules of N atoms, the multi-dimensional Taylor series is truncated in a similar way leading to the multi-dimensional analogue of 2.15,

$$\left[-\sum_i^{3N}\frac{1}{2m_i}\frac{\partial^2}{\partial x_i^2}+\frac{1}{2}(\mathbf{x}-\mathbf{x}_{eq})\mathbf{H}(\mathbf{x}-\mathbf{x}_{eq})\right]\Xi(\mathbf{x})=E\Xi(\mathbf{x}) \tag{2.22}$$

where $\mathbf{x}$ is the matrix of the atomic co-ordinates, $\mathbf{x}_{eq}$ defines the equilibrium structure and $\mathbf{H}$ is the Hessian matrix containing force constants with respect to all $3N$ nuclear cartesian displacements.

$$\mathbf{H}_{ij} = \frac{\partial^2 V}{\partial x_i \partial x_j} = \begin{bmatrix} \frac{\partial^2 V}{\partial x_1 \partial x_1} & \frac{\partial^2 V}{\partial x_1 \partial x_2} & \frac{\partial^2 V}{\partial x_1 \partial x_3} & \cdots & \frac{\partial^2 V}{\partial x_1 \partial x_{3N}} \\ \frac{\partial^2 V}{\partial x_2 \partial x_1} & \frac{\partial^2 V}{\partial x_2 \partial x_2} & \frac{\partial^2 V}{\partial x_2 \partial x_3} & \cdots & \frac{\partial^2 V}{\partial x_2 \partial x_{3N}} \\ \frac{\partial^2 V}{\partial x_3 \partial x_1} & \frac{\partial^2 V}{\partial x_3 \partial x_2} & \frac{\partial^2 V}{\partial x_3 \partial x_3} & \cdots & \frac{\partial^2 V}{\partial x_2 \partial x_{3N}} \\ \vdots & \vdots & \vdots & \ddots & \vdots \\ \frac{\partial^2 V}{\partial x_{3N} \partial x_1} & \frac{\partial^2 V}{\partial x_{3N} \partial x_2} & \frac{\partial^2 V}{\partial x_{3N} \partial x_3} & \cdots & \frac{\partial^2 V}{\partial x_{3N} \partial x_{3N}} \end{bmatrix} \tag{2.23}$$

Equation 2.22 can be solved through a matrix transformation into a unique set of mass dependent spatial coordinates, it is then possible to separate this $3N$-dimensional equation into $3N$ one-dimensional Schrödinger equations which are identical to equation 2.19. To do this we must first mass-weight the Hessian, $\mathbf{H}_{ij}$, obtaining the mass-weighted Hessian matrix $\mathbf{G}_{ij}$,

$$\mathbf{G}_{ij} = \frac{1}{\sqrt{m_i m_j}} \mathbf{H}_{ij} \tag{2.24}$$

This matrix is transformed through diagonalisation to obtain, matrix $\mathbf{P}$ and $\mathbf{K}$.

$$\mathbf{G}_{ij} = \mathbf{PKP^{-1}} \tag{2.25}$$

Where,

$$\mathbf{P} = \begin{bmatrix} x_{1,1} & x_{1,2} & x_{1,3} & \ldots & x_{1,3N} \\ x_{2,1} & x_{2,2} & x_{2,3} & \ldots & x_{2,3N} \\ x_{3,1} & x_{3,2} & x_{3,3} & \ldots & x_{3,3N} \\ \vdots & \vdots & \vdots & \ddots & \vdots \\ x_{3N,1} & x_{3N,2} & x_{3N,3} & \ldots & x_{3N,3N} \end{bmatrix} \tag{2.26}$$

and,

$$\mathbf{K} = \begin{bmatrix} \lambda_1 & 0 & 0 & \dots & 0 \\ 0 & \lambda_2 & 0 & \dots & 0 \\ 0 & 0 & \lambda_3 & \dots & 0 \\ \vdots & \vdots & \vdots & \ddots & \vdots \\ 0 & 0 & 0 & \dots & \lambda_{3N} \end{bmatrix} \tag{2.27}$$

Each column of matrix $\mathbf{P}$ corresponds to a molecular vibration known as a vibrational normal mode of the system, each associated with its harmonic oscillator wave function. Matrix $\mathbf{K}$ is a diagonal matrix of the square root of the force constants (or eigenvalues) λ_i corresponding to each normal mode. Since $\lambda_i = \frac{k}{\mu}$, the vibrational frequencies can be calculated from:

$$\nu_i = \frac{\sqrt{\lambda_i}}{2\pi} = \frac{1}{2\pi}\sqrt{\frac{k_i}{\mu}} \tag{2.28}$$

Since equation 2.22 is over $3N$ degrees of freedom there will be three translational and three rotational modes, in the case of linear molecules there are only two rotational modes. The eigenvalues associated with these modes should be close to zero and their closeness to zero can be used as a diagnostic of how well optimised a structure is. The remaining $3N - 6$ modes correspond to vibrations and all positive frequencies indicate a minimum stationary point has been found and one or more imaginary frequencies indicate a transition state structure has been found.

It is common to apply scaling factors to the computed harmonic frequencies. This is for the following two reasons. Firstly is the neglect of the true anharmonic nature of bonds in molecules which leads to a lowering of frequencies and secondly errors in the model force-field used in the calculation of the harmonic potential. The application of scaling factors

corrects for these errors leading to experimentally comparable frequencies, and compensates for these approximations in a computationally inexpensive way.

2.3 The Empirical Bond Polarisability Model

The empirical Bond Polarisability Model[35] (BPM) provides a convenient and computationally inexpensive framework for the calculation of non-resonant Raman spectra intensities.

Within the BPM, the first assumption is that the total polarisability of a molecule can be modelled in terms of single bond contributions, which are assumed to be independent of the chemical environment and hence transferable between compounds. Each particular bond is assigned a polarisation parallel to the bond, $\alpha_{\parallel}$, and a polarisation perpendicular to the bond, $\alpha_{\perp}$. Thus, the polarisabilty contribution of a bond, b, is given by, $\Pi^{b}_{\alpha\beta}$,

$$\Pi^{b}_{\alpha\beta} = \tfrac{1}{3}(\alpha_{\parallel} + 2\alpha_{\perp}) + (\alpha_{\parallel} - \alpha_{\perp})\left(\frac{R_{\alpha}R_{\beta}}{R^2} - \tfrac{1}{3}\delta_{\alpha\beta}\right) \tag{2.29}$$

where α and β are cartesian coordinates and R is the vector connecting two atoms. The second key assumption in this model is cylindrical symmetry around the bond's axis and that any perturbation from cylindrical symmetry arises from the effects of the chemical environment of the bond. The third final assumption is that the polarisabilty of bond, depends only on its length R.

The mean static polarisability of a molecule, which is defined as, $\overline{\alpha}$,

$$\overline{\alpha} = \frac{1}{3}(\alpha_{xx} + \alpha_{yy} + \alpha_{zz}) \tag{2.30}$$

can then be calculated by summing up the mean of the individual bond polarisabilities, $\bar{\Pi}$,

$$\bar{\Pi} = \Pi_{xx} + \Pi_{yy} + \Pi_{zz} \equiv \tfrac{1}{3}(\alpha_{\parallel} + 2\alpha_{\perp}) \tag{2.31}$$

for all the bonds in a molecule. Hence the mean static polarisability of a molecule with K bonds can be calculated as:

$$\overline{\alpha} = \sum_{b=1}^{K} \Pi_{xx} + \Pi_{yy} + \Pi_{zz} \tag{2.32}$$

Using this model, the contribution of a bond's derivative to the the polarisability derivative with respect to atomic displacement can be calculated as, $\dfrac{\partial \Pi^{b}_{\alpha\beta}}{\partial u_{\ell\gamma}}$, where $u_{\ell\gamma}$ is the γth cartesian component of the ℓ atom. This is dependant on only 4 parameters, $\alpha_{\parallel}(B)$, $\alpha_{\perp}(B)$, $\alpha'_{\perp}(B)$ and $\alpha'_{\parallel}(B)$ for a bond, B. The use of one perpendicular parameter implicitly assumes the cylindrical symmetry of the bond.

The BPM can then be extended for the empirical calculation of the non-resonant Raman scattering intensities since derivatives of the polarisability can then be evaluated. For an N atom harmonic system, the Raman intensities calculated through the BPM are given by,

$$I_{\eta'\eta}(\omega) = C\omega_L\omega_S^3 \sum_{f=1}^{3N} \frac{\langle n(\omega_f)\rangle + 1}{\omega_f} \left| \sum_{\alpha\beta} \eta'_{\alpha}\eta_{\beta}P_{\alpha,\beta,f} \right|^2 \times \delta(\omega - \omega_f) \tag{2.33}$$

where C is a frequency independent constant; ω_L and ω_S are the incident and scattered light frequencies; $\omega \equiv \omega_L - \omega_S$ is the Raman shift; η'_{α} and η_{β} are unit vectors along the incident and scattered polarisation directions;

$\langle n(\omega_f)\rangle \equiv [exp(\beta\hbar\omega_f) - 1]^{-1}$ is the Boltzmanns distribution function of vibrational mode f at temperature $T = (k_b\beta)^{-1}$. The subscripts α and β represent cartesian components of the vectors or tensor and $P_{\alpha,\beta,f}$ is the derivative of the polarisability tensor along vibrational normal mode coordinate f, and is given by

$$P_{\alpha,\beta,f} = \sum_{\ell\gamma} \left[\frac{\partial P_{\alpha\beta}}{\partial u_\gamma(\ell)}\right]_0 \chi_\gamma(\ell|f) \qquad (2.34)$$
$$(\gamma = x, y, z, \ell = 1, ..., N, f = 1, ..., 3N)$$

where $P_{\alpha\beta}$ is the electronic polarisation and the derivative is performed with respect to the γth cartesian displacement, $u_\gamma(\ell)$, for ℓth atom. The term $\chi_\gamma(\ell|f)$ is the γth component of the unit vectors of the fth normal mode of the ℓth atom.

The term $P_{\alpha,\beta,f}$ is approximated by a sum of the bond polarisation contributions as follows,

$$\begin{aligned} P_{\alpha,\beta} = \frac{1}{2}\Bigg[& -\sum_{\ell B}\left\{\frac{\alpha'_\parallel(B) + 2\alpha'_\perp}{3}\right\}\delta_{\alpha\beta} \\ & + \left\{(\alpha_\parallel(B) - \alpha_\perp(B)\right\}\left(\frac{R_\alpha(\ell,B)R_\beta(\ell,B)}{R(\ell,B)^2} - \frac{1}{3}\delta_{\alpha\beta}\right)\Bigg] \end{aligned} \qquad (2.35)$$

where is B is the bond which is connected to the ℓth atom and $\mathbf{R}(\ell, B)$ is the corresponding vector from atom ℓ to the neighbouring atom ℓ' specified by B. The quantities $R_\alpha(\ell, B)$ and $R_\beta(\ell, B)$, are the α and β components of the length $R(\ell, B)$. $\alpha_\parallel(B)$ and $\alpha_\perp(B)$ are the static molecular bond polarisabilities for the bond, B, in the directions perpendicular and parallel to the bond, it is assumed that $\alpha_\parallel(B)$ and $\alpha_\perp(B)$ are only a function of bond length $R(\ell, B)$.

Within the BPM, the polarisability derivatives with respect to a normal mode $\overrightarrow{\chi_f}$ are evaluated via,

$$\begin{aligned} P_{\alpha\beta,f} &= -\sum_{\ell,B}\left[\frac{\mathbf{R_0}(\ell|B)\cdot\overrightarrow{\chi}(f|\ell)}{R_0(\ell,B)^2}\right] \\ &\times \left\{\left(\frac{\alpha'_{\parallel}(B)+2\alpha'_{\perp}}{3}\right)\delta_{\alpha\beta} + (\alpha'_{\parallel}(B)-\alpha'_{\perp}(B)) \times \left(\frac{R_{0\alpha}(\ell,B)R_{0\beta}(\ell,B)}{R_0(\ell,B)^2} - \frac{1}{3}\delta_{\alpha\beta}\right)\right\} \\ &+ \left(\frac{\alpha_{\parallel}(B)-\alpha_{\perp}(B)}{R_0(\ell,B)}\right) \\ &\times \left\{\frac{R_{0\alpha}(\ell,B)\chi_{\beta}(\ell|f)-R_{0\beta}(\ell,B)\chi_{\alpha}(\ell|f)}{R_0(\ell,B)} - \frac{\mathbf{R_0}(\ell,B)\cdot\overrightarrow{\chi}(f|\ell)}{R_0(\ell,B)} \times \frac{2R_{0\alpha}(\ell,B)R_{0\beta}(\ell,B)}{R_0(\ell,B)^2}\right\} \end{aligned} \tag{2.36}$$

If equation 2.36 is expanded, the first term would represent the change in the isotropic part of the polarisability induced by bond stretching, the second term would represent the corresponding change in the anisotropic part of the polarisabilty and the third term would be the change in the poloarisabilty from bond rotation.

where $\alpha'_{\parallel}(B)$ and $\alpha'_{\perp}(B)$, the radial derivatives of $\alpha_{\parallel}(B)$ and $\alpha_{\perp}(B)$, are:

$$\alpha'_{\parallel}(B) = \frac{\partial\alpha_{\parallel}(B)}{\partial R(\ell,B)}, \text{ and } \alpha'_{\perp}(B) = \frac{\partial\alpha_{\perp}(B)}{\partial R(\ell,B)} \tag{2.37}$$

The values of $\alpha_{\parallel}(B)$, $\alpha_{\perp}(B)$, $\alpha'_{\parallel}(B)$ and $\alpha'_{\perp}(B)$ in this study are given as a function of the bond length between carbon-carbon atoms. The following values for flat graphite[36] are utilised: $\alpha_{\parallel} - \alpha_{\perp} = 0.32$ Å^3, $\alpha'_{\parallel}(B) + 2\alpha'_{\perp} = 7.55$ Å^2 and $\alpha'_{\parallel}(B) - \alpha'_{\perp} = 2.60$ Å^2 and for carbon nanotubes[37] $\alpha_{\parallel} - \alpha_{\perp} = 0.04$ Å^3, $\alpha'_{\parallel}(B) + 2\alpha'_{\perp} = 4.70$ Å^2 and $\alpha'_{\parallel}(B) - \alpha'_{\perp} = 4.00$ Å^2.

2.4 Kohn-Sham Density Functional Theory

The strategies for developing empirical potentials usually follow two main approaches. The first is fitting parameters to experimental data such as bond lengths from crystallography or thermochemistry data, and the second is using ab initio data. Although throughout this thesis the use of

empirical potentials is the focus, we use density functional theory to generate reference data used for fitting the MM potential in the parameterisation with the goal of producing a force-field to simulate accurate vibrational frequencies using the MM potential.

Two strategies could be taken to achieve this using DFT. The first is directly fitting to frequencies produced by DFT and minimising the error. This method is convenient but inherently flawed, since directly fitting to frequencies does not allow for vibrational mode reordering to happen during fitting. This is because it requires the assumption that vibrational modes are already correctly ordered for the empirical potentials parameters before fitting. This leads to a small proportion of vibrational modes being correctly fitted to its DFT counterpart and others fitted to the wrong modes. The second method is fitting to the hessian matrix, which avoids the aforementioned issue of assuming vibrational modes are correctly ordered before fitting. This is because the hessian matrix takes into account all modes and there dependencies on each other with no a priori of ordering, hence all modes are simultaneously fitted by minimising the error in the hessian matrix between DFT and an empirical potential. This method is utilised in chapter 3.2 to fit the MM potential and further explained.

Density functional theory (DFT) provides a computationally low-cost ground state electronic structure method in which the energy is completely determined by the electron density, ρ. The basis for DFT comes from the Hohenberg-Kohn theorems[38] which state that there exists a one to one correspondence between the electron density of the system and the energy,

and the ground state energy can be determined variationally. A more intuitive view of DFT comes from the following arguments:[24]

1. The integral of the density defines the number of electrons.

2. The cusps in the density define the position of nuclei.

3. The heights of the cusps define the corresponding nuclear charges.

The significance of the Hohenberg-Kohn theorems is best illustrated by comparison to wavefunction methods. The wavefunction, Ψ, for a N electron system is dependent on $4N$ variables, three spatial (r_N) plus one spin coordinate (s_N) for each electron. The electron density is the square of the wavefunction integrated over $N-1$ electron coordinates and each spin coordinates (where $x_N = r_N, s_N$).

$$\rho = N \int |\Psi(x_1, x_2, x_3, .., x_N)|^2 ds_1 dx_2 ... dx_N \tag{2.38}$$

It is dependent on three spatial coordinates regardless of the system of interest. Accordingly, while the complexity of the wavefunction increases with system size DFT remains dependent on only its three spatial coordinates of the density.

The problem with DFT is that although it has been proven that different densities yield different ground state energies, the functional that connect these two quantities are not fully known. Hence the challenge for DFT is the design of functionals to connect accurately the electron density with the energy.

Within DFT under the Born-Oppenheimer approximation the total energy functional, $E[\rho]$ is divided into three parts:

1. The kinetic energy, $T[\rho]$.

2. The nuclei-electron interaction, $V_{ne}[\rho]$.

3. The electron-electron interaction, $V_{ee}[\rho]$.

The $V_{ee}[\rho]$ term may be further divided into the Coulomb and exchange contributions to the energy, $J[\rho]$ and $K[\rho]$, implicitly including the correlation energy across all terms.

In this formulation of DFT, the Hohenberg-Kohn theorem provides the framework to calculate the energy using the electron density of an atomic or molecular system, however, only the form of the $V_{ne}[\rho]$ and $J[\rho]$ are known through their classical expressions. Attempts to approximate the rest of these terms in an orbital-free formulation have not shown sufficient accuracy for applications.[39,40] If such functionals were found, the full potential of DFT would be recognised.

To overcome this issue, Kohn-Sham re-introduced orbitals,[41] since the inaccuracy of orbital free models comes from the poor representation of the kinetic energy functional, where ϕ_i is an orbital.

$$\rho = \sum_{i=1}^{N_{elec}} |\phi_i|^2 \tag{2.39}$$

In the Kohn-Sham formalism, the kinetic energy is split into two parts, the non-interacting kinetic energy, $T_{ni}[\rho]$ and a correction to the kinetic energy, taking into account the interacting nature of electrons. Consequently, $E[\rho]$ becomes,

$$E[\rho] = T_{ni}[\rho] + V_{ne}[\rho] + J[\rho] + E_{xc}[\rho] \tag{2.40}$$

where,

$$E_{xc}[\rho] = (T[\rho] - T_{ni}[\rho]) + (V_{ee}[\rho] - J[\rho]) \tag{2.41}$$

$E_{xc}[\rho]$ is known as the exchange-correlation functional and this contains all the terms that are unknown. The first parentheses is the correction to the non-interacting kinetic energy and can be considered the kinetic correlation energy resulting from the interacting nature of electrons. The last term contains all non classical contributions to the electron-electron interaction including the exchange energy. The challenge of Kohn-Sham DFT is finding accurate approximations for this exchange-correlation functional. Although $E_{xc}[\rho]$ contains a small contribution to the energy, it is essential for this to be approximated well to obtain chemical accuracy.

Several approximations of the $E_{xc}[\rho]$ exist, the simplest functional is known as the local density approximation (LDA), which was proposed by Kohn and Sham.[41] $E_{xc}^{LDA}[\rho]$ depends purely on the electron density ρ and it is assumed that the density can be treated as a uniform electron gas. Consequently, the LDA exchange-correlation functional, $E_{LDA}[\rho]$, is local, and only depends on the density at the position $\mathbf{r}$ and can be summarised as,

$$E_{xc}^{LDA}[\rho] = \int \rho(\mathbf{r})\epsilon_{xc}[\rho(\mathbf{r})]d\mathbf{r} \tag{2.42}$$

where $\epsilon_{xc}[\rho(\mathbf{r})]$ is the exchange-correlation energy per particle of a uniform electron gas and its energy per particle is weighted with the probability $\rho(\mathbf{r})$ that there is an electron at this position in space. Writing $E_{xc}[\rho]$ in this way defines the LDA, the quantity $\epsilon_{xc}[\rho(\mathbf{r})]$ can be further split into

exchange and correlation contributions,

$$\epsilon_{xc}[\rho(\mathbf{r})] = \epsilon_x[\rho(\mathbf{r})] + \epsilon_c[\rho(\mathbf{r})] \tag{2.43}$$

where $\epsilon_x[\rho(\mathbf{r})]$ represents the exchange energy and $\epsilon_c[\rho(\mathbf{r})]$ the correlation energy.

The next class of exchange-correlation functional are the generalised gradient approximation (GGA) functionals which improve on LDA. These functionals depend upon both the electron density and the gradient of the electron density, $\nabla\rho$. Including a dependence on the gradient of the electron density aims to account for the inhomogeneity of electron density and these functionals can be summarised as,

$$E_{xc}^{GGA}[\rho] = \int \rho(\mathbf{r})\epsilon_{xc}[\rho(\mathbf{r}), \nabla\rho]d\mathbf{r} \tag{2.44}$$

GGA functionals are usually based on LDA functionals, with an additional correction that relies on the electron density gradient. An example of a GGA functional is the BLYP functional.[42,43]

Meta-GGA (mGGA) functionals take this one step further. These are potentially more accurate then GGA functionals and introduce a dependence on the second derivatives of the density (the laplacian), $\nabla^2\rho$ or the related orbital kinetic energy density $\tau(\mathbf{r}) = \frac{1}{2}\sum_{i=1}^{occ}|\nabla\phi_i|^2$ and are summarised as,

$$E_{xc}^{mGGA}[\rho] = \int \rho(\mathbf{r})\epsilon_{xc}[\rho(\mathbf{r}), \nabla\rho, \nabla^2\rho(\mathbf{r})]d\mathbf{r} \tag{2.45}$$

Common examples of meta-GGA functionals include TPSS[44], M06-L[45] and M11-L.[46]

Table 2.1: A table of exchange-correlation functionals.

Level	Name	Variables	Examples
1	Local density	ρ	LDA, LSDA
2	GGA	$\rho, \nabla\rho$	BLYP, OLYP, PBE
3	Meta-GGA	$\rho, \nabla\rho, \nabla^2\rho$ or τ	TPSS, M06-L,KT1
4	Hybrid-GGA	$\rho, \nabla\rho, \nabla^2\rho$ or τ, HF exchange	B3LYP,M06,PBE0
5	Generalised RPA	$\rho, \nabla\rho, \nabla^2\rho$ or τ HF exchange and virtual orbitals	OEP2

A further class of exchange-correlation functional are hybrid functionals. These functionals incorporate a combination of contributions from Hartree-Fock exchange, which is exact, in addition to exchange and correlation from DFT, a general example could be:

$$E_{xc}^{hybrid}[\rho] = E_c^{DFT}[\rho] + (1-a)E_x^{DFT}[\rho] + aE_x^{HF}[\rho] \tag{2.46}$$

The weighting of each of these sources by variable, a, can be fitted to experimental or high-level ab initio data.

Each of these approximations aims to build on the former and generally increases in chemical accuracy and complexity. The improvements achieved through GGA and hybrid functionals have had a large impact in DFT since they enabled high enough accuracy for chemical applications. Table 2.1 shows commonly used functionals and their level on Jacob's ladder of classification as well as their dependencies.

As shown, a result of Kohn-Sham's formulation of DFT head lead to a plethora of models for the $E_{xc}[\rho]$ being developed at all of the levels of Jacob's ladder. Many of these functionals included empirical parameters such as the range and proportion of Hartree-Fock exchange energy

and hence enabled us to fit the functionals to experimental and ab initio datasets for optimal accuracy. This has resulted in many functionals being optimised for there specific purposes, for example, the range separated functionals such as CAM-B3LYP[47] has been designed for the accurate description of charge transfer in TDDFT, Van der Waals functionals, such as VV10,[48] have been designed to accurately account for dispersion interactions which are not described by local DFT functionals, moreover many others have been fitted to high accuracy to replicate large data sets and properties including structure, thermochemistry, ionisation potentials etc...

In practice, to use Kohn-Sham DFT we must first find a representation of the orbitals in equation 2.39. This is achieved through the use of basis sets. Commonly used basis sets are made of either Slater-type orbitals (STOs), which have a function with a radial dependence of form $e^{-\alpha r}$, or Gaussian-type orbitals (GTOs), which have a radial dependence of the form $e^{-\alpha r^2}$. STOs accurately represent the features of hydrogen atomic orbitals, with a cusp at $r = 0$ and exponential decay, however they are computationally expensive to use for molecular systems. A single GTOs does not closely represent the features of a STO due to the wrong behaviour at $r = 0$ and shows slow exponential decay, they are much simpler to use and hence faster. Contracted basis functions of these GTOs provide a practical solution to this problem. These functions use a linear combination of GTOs to reproduce the features of the STO, at a much lower computational cost.

In this study, the Split Valence (Pople) basis sets are used.[49] These take into account that Chemistry is primarily concerned with valence electrons

and so it is most important to obtain a flexible description of these electrons. This is addressed by the basis sets through the use of more functions to describe the valence orbitals than core orbitals.

In order to compute energies and hence properties, we must use our basis sets to find the orbitals, ϕ_i, which minimise the energy, E, recasting equation 2.40 as an orbital expression for the density we have:

$$\begin{aligned} E[\rho(\mathbf{r})] &= \sum_{i}^{N}\left(\left\langle \phi_i|-\frac{1}{2}\nabla_i^2|\phi_i\right\rangle - \left\langle \phi_i|\sum_{k}^{nuclei}\frac{Z_k}{|\mathbf{r}_i-\mathbf{r}_k|}|\phi_i\right\rangle\right) \\ &+ \sum_{i}^{N}\left\langle \phi_i|\frac{1}{2}\int\frac{\rho(\mathbf{r}')}{|\mathbf{r}_i-\mathbf{r}'|}d\mathbf{r}'|\phi_i\right\rangle + E_{xc}[\rho(\mathbf{r})] \end{aligned} \tag{2.47}$$

where N is the number of electrons, and the density is constructed from orbitals from a Slater determinant wavefunction, which leads to a set of one-electron Kohn-Sham secular equations. These can be iteratively solved to find the ground state density of system by minimising the Kohn-Sham orbitals using the self-consistent field procedure to find the ground state energy. Derivatives of the Kohn-Sham energy can be used to calculate properties such as harmonic frequencies using second derivatives of the energy.

One of the most popular exchange-correlation functionals in Kohn-Sham DFT is the hybrid B3LYP functional[50–53] which has shown to be one of the most successful in overall performance with wide applicability. The functional is expressed as,

$$\begin{aligned} E_{xc}^{B3LYP} &= (1-a)E_x^{LSDA} + aE_x^{HF} + bE_x^{B88} \\ &+ (1-c)E_c^{LSDA} + cE_c^{LYP} \end{aligned} \tag{2.48}$$

where a, b and c are free parameters which were optimised to 0.20, 0.72

and 0.81. E_x^{HF} is Hartree-Fock is exchange, E_x^{LSDA} is the local spin density approximation exchange (LSDA),[52] bE_x^{B88} is the B88 exchange functional,[50] E_c^{LSDA} the local correlation functional of Vosko, Wilk, and Nusair (VWN)[52] and E_c^{LYP} the correlation functional of Lee, Yang and Parr (LYP).[51] In particular with relevance to this study, the combination of the B3LYP functional and 6-31G(d) Pople split valence basis set is one of the recommended levels of theory for predicting vibrational frequencies of molecular systems in terms of accuracy and computational cost when using electronic structure methods has been utilised here.[54,55]

Calculations using DFT in this thesis were performed in the Q-Chem software package.[56] The structures were optimised and frequencies evaluated at the B3LYP/6-31G* level of theory with the standard quadrature grid, 50 point Euler-Maclaurin radial grid with a 194 point Lebedev angular grid.

2.5 Software Implementation

In this thesis, all MM simulations were carried out within a newly developed in-house code in Fortran90. The code has three principle functions, firstly geometry optimisation to find the equilibrium structure, secondly vibrational analysis within the harmonic approximation to evaluate vibrational frequencies and associated normal modes, and lastly, Raman spectra simulations utilising the BPM.

The calculations presented are based upon the MM potential. To enable efficiency and speed with the geometry optimisation and vibrational

analysis, analytical first derivatives of the MM potential were derived for the rapid evaluation of forces to allow quick geometry optimisation and second derivatives for the Hessian matrix for vibrational analysis. Analytical derivatives are much faster than numerical derivatives based upon energies, and this difference grows rapidly as the system size increases. Furthermore, ambiguity regarding the step size within the numerical derivative methods is removed. The percentage speedup in evaluating the Hessian with analytical derivatives is demonstrated in figure 2.1 (performed in serial on an Intel core i7-3635QM processor), showing the percentage speedup for a series of Fullerenes, where for example, C_{26} is 1200 % faster.

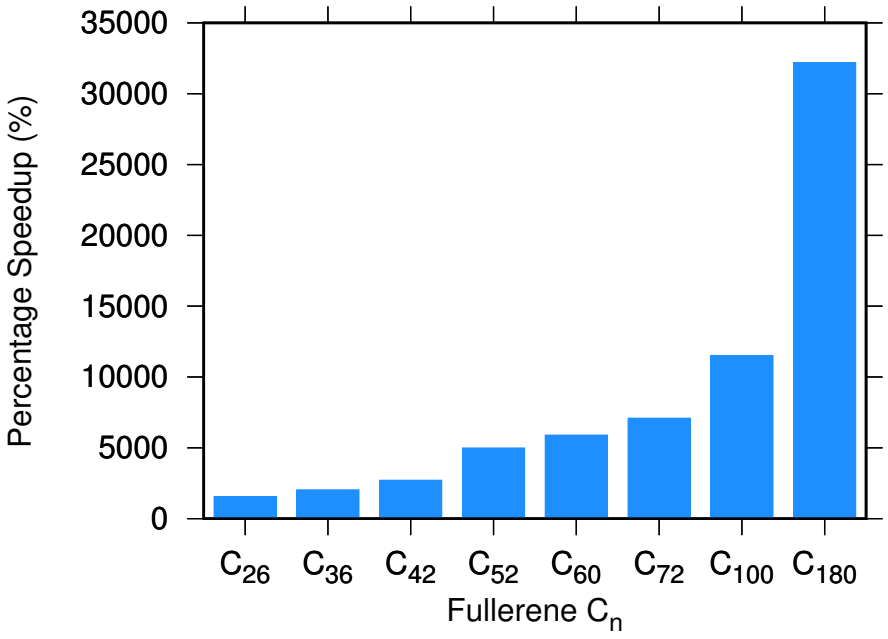


Figure 2.1: Percentage speedup in the vibrational analysis for increasing sized Fullerenes from numerical to analytical second derivatives.

Furthermore, a cut-off in the potential was implemented after parameterisation in chapter 3.2, via benchmarking errors in frequencies. Figure

2.2 shows the percentage speed up for frequency analysis and the root mean square error (RMSE) in frequencies from a fully interacting system with varying cut-off lengths. The cut-off does significantly reduce the computation time for the Hessian, however, it is only possible to implement spatial cut-offs in a consistent manner for off-diagonal elements, therefore diagonal elements gain no speed up. Although figure 2.2 does show no error in the frequencies up to very small distances, the cut-off was chosen to be at least 8 Å for consistent treatment of this parameter when the additional dispersion interaction term was included.

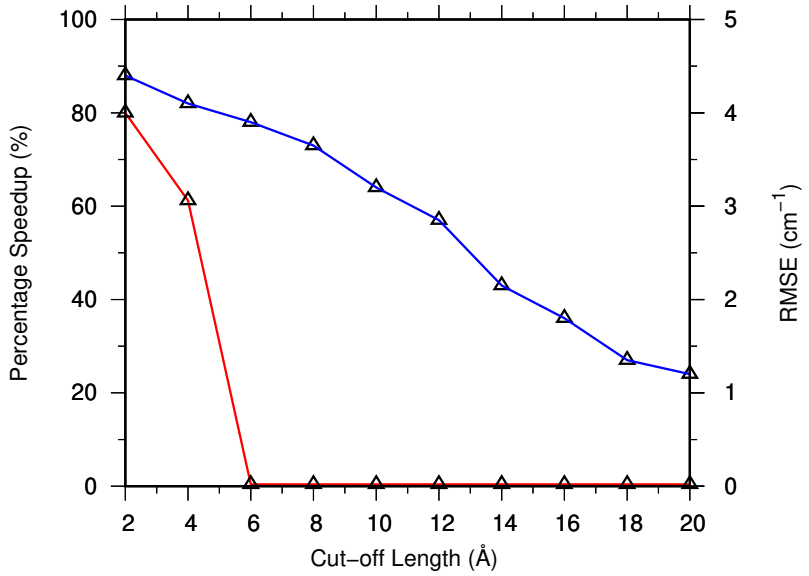


Figure 2.2: Percentage speedup (blue) and RMSE in frequencies (red) in vibrational analysis with increasing cut-off size relative to a fully interacting system (no cut-off).

To further allow larger scale modelling, the code was then optimised and parallelised. This required profiling CPU time which revealed as expected,

the first and second derivative routines as the most expensive parts of the calculations. Subsequently, these routines were made parallel to accelerate the code using OpenMP threading, enabling multi-core architectures to be exploited by the code and hence allow larger systems to be studied with the MM potential.

The geometry optimisation utilises the iterative conjugate gradient algorithm to minimise the energy, E, and find the equilibrium structure as a function of the atomic coordinates, $\mathbf{x_i} = (x_1, x_2, x_3, ..., x_{3N})$. In this technique the search direction given by gradient information from both current, i, and previous, $i-1$, iterations.

The first step in this algorithm utilises the steepest descent method providing the initial direction i.e. using $\mathbf{x_0}$ and $\mathbf{g_0} = \nabla E(\mathbf{x}_0)$ and is given by,

$$\mathbf{x}_{i+1} = \mathbf{x}_i - k_i \mathbf{g}_i \tag{2.49}$$

The conjugate gradient method is then invoked for the subsequent steps for the above formula, where $\mathbf{g}_i$ is given by,

$$\mathbf{g}_i = \nabla E(\mathbf{x}_i) + \beta_n \mathbf{g}_{i-1} \tag{2.50}$$

The implementation here uses the Fletcher-Reeves formula[57] to calculate the value of β,

$$\beta_i = \frac{|\nabla E(\mathbf{x}_i)|^2}{|\nabla E(\mathbf{x}_{i-1})|^2} = \frac{\mathbf{g}_i^t \mathbf{g}_i}{\mathbf{g}_{i-1}^t \mathbf{g}_{i-1}} \tag{2.51}$$

The algorithm is then iterated until the displacement and gradient threshold criteria is met.

Following geometry optimisation with energy gradient convergence of 10^{-8} E_h Å^{-1}, vibrational analysis is performed. The $3N \times 3N$ Hessian matrix calculated using analytical second derivatives and then mass-weighted and diagonalised using the math kernel library (MKL). The vibrational modes and frequencies are then used to simulate Raman spectra, where polarisability derivatives are calculated in order to evaluate Raman intensities. This generates a stick spectrum which is then normalised and convoluted with Lorentzian functions. Additionally, these modes and frequencies are also binned to evaluate the vibrational density of states. The vibrational modes are then formatted and printed to enable visualisation in mainstream software such as IQmol and Visual Molecular Dynamics (VMD).

In order to study infinite systems, periodic boundary conditions were implemented. This implementation used the minimum image convention, with a potential cut-off distance that always is always less than or equal to half the box length. Isotopic effects of including ^{13}C in naturally occurring abundances were explored and showed to have negligible effects on the computed spectra. The MM potential was further extended with the addition of dispersion interaction and more details of this are given in chapter 6. All calculations utilising the MM potential in chapters 3, 4, 5 and 6 were performed on a desktop computer with a quad core Intel Xeon CPU E5-1620 processor with 32GB of RAM.

Chapter 3

An Empirical Force Field for the Simulation of the Vibrational Spectroscopy of Carbon Nanomaterials

In this chapter, an empirical force field for carbon based upon the Murrell-Mottram potential is developed for the calculation of the vibrational frequencies of carbon nanomaterials. The potential is parameterised using data from density functional theory calculations through a Monte-Carlo Hessian-matching approach, and when used in conjunction with the empirical bond polarisability model it provides an accurate description of the non-resonant Raman spectroscopy of carbon nanotubes and graphene. With the availability of analytical first and second derivatives, the computational cost of evaluating harmonic vibrational frequencies is a fraction of the cost of corresponding quantum chemical calculations, and makes the accurate atomistic vibrational analysis of systems with thousands of atoms

possible. Subsequently, the non-resonant Raman spectroscopy of carbon nanotubes and graphene, including the role of defects, carbon nanotube junctions and carbon nanocones is explored.

3.1 Introduction

Although Raman spectroscopy is used routinely to study carbon nanotubes and graphene based materials, the prediction of the Raman spectroscopy of these systems is a challenge for computational methods. The accurate calculation of the vibrational frequencies and associated spectroscopy of carbon nanomaterials can potentially aid the interpretation of experimental measurements and allow the relationship between the molecular structure and the observed features to be explored. Simulation of vibrational spectroscopy using quantum chemical methods, such as density functional theory, is well established. However, the computational cost of these methods makes them impractical for the study of large systems such as carbon nanotubes. This can be overcome for the simulation of pristine nanotubes through the use of periodic boundary conditions, but the use of periodic boundary conditions to study realistic carbon nanotubes that are non-uniform and contain vacancies and defects is limited since such calculations would require large unit cells. Furthermore, periodic boundary conditions are not suitable for studying systems such as nanotube junctions which are inherently non-periodic.

Several groups have reported DFT based harmonic frequency calculations of the infrared and Raman spectroscopy of fullerenes, including

C_{60} and C_{70}.[58–62] Further calculations have also been performed for related systems such as [n]cycloparaphenylene[63,64] and a nanotorus.[65] DFT calculations have been used to study the Raman spectroscopy of zig-zag nanotubes of varying diameter,[66] accurately reproducing the diameter dependence of the RBM, although these calculations only considered one unit cell capped with hydrogen atoms. Such small model systems would not be expected to describe other bands such as the G-band accurately. Another study employed DFT to study the vibrational spectroscopy of ultra-small diameter nanotubes[67] and Yumura *et al.* reported DFT calculations of the vibrational frequencies of relatively large nanotubes, consisting of up to 120 carbon atoms, and studied the effects of the end caps on the spectra.[68] Recently the Raman spectroscopy of zig-zag nanotubes with lengths of up to 2.15 nm were studied using DFT, with larger tubes studied using a Cartesian coordinate transfer technique.[69] The calculations reproduced the dependence of the frequency of the RBM with the tube diameter, but larger tubes were required to describe the G-band modes accurately. It was found that the G-band was more sensitive to the presence of defects, and there was a reduction in the intensity of the RBM on the introduction of a Stone-Wales (SW) defect. These studies represent the current limit of what can be achieved through direct non-periodic DFT calculations.

The Raman spectroscopy of nanotubes including the effect of Stone-Wales and di-vacancy defects on the spectra has also been studied,[70] using plane-wave based periodic DFT with the Raman intensities computed using the empirical BPM.[71] Other related approaches have been reported and used to study the Raman spectra of liquids.[72] Other work has studied the

effect of the Raman excitation profile for carbon nanotubes under torsion or uniaxial strain.[73] Computationally less expensive methods that have been applied to study the vibrational spectroscopy of carbon nanotubes include tight-binding DFT, which has been applied to study the vibrational spectra of fullerenes,[74,75] and force constant based methods.[37,76–78] Calculations of the resonant Raman spectroscopy of carbon nanotubes using a non-orthogonal tight-binding model have been reported, and the influence of point defects on the spectra studied.[79,80]

Ideally, it would be possible to model the vibrational spectroscopy of these systems efficiently without the constraints of periodicity, providing an accurate description of experiment and opening the opportunity for the role of edges and defects to be explored. Empirical potentials provide a solution to this problem. The attraction of this approach for studying the vibrational spectroscopy of these systems is evident by comparing the associated computational cost with a DFT calculation. On a single processor, a B3LYP/6-31G* calculation of the harmonic frequencies of C_{60} and C_{70} requires over 40,000 and 60,000 seconds, respectively. Similar calculations using the empirical MM potential take two and three seconds, representing a many thousand-fold decrease in computational time. Furthermore, the use of empirical potentials alleviates the memory requirements of using quantum chemical methods, allowing systems of thousands of atoms to be studied routinely. However, for empirical potentials to be a viable method for simulating the vibrational spectroscopy of these systems, the accuracy of quantum chemical methods needs to be retained.

In this work we study the vibrational spectroscopy of carbon based materials using an empirical potential. The parameterisation of the well-known potentials, such as the REBO[26] potential, focuses on energetics and structure and does not consider the vibrational properties. As a consequence of this, its been shown in a recent study that the REBO potential performed poorly in describing the vibrational frequencies of C_{60} and carbon nanotubes.[81] It was found that to achieve an adequate description of the IR spectrum of C_{70} and the RBM and G-band of carbon nanotubes, it was necessary to treat high and low-frequency modes separately through two parameter sets. The calculation of vibrational frequencies has implications beyond simulating IR and Raman spectra. Vibrational frequencies provide an indirect probe of the potential energy surface, providing a measure of the curvature of the surface, and it is an open question as to whether empirical potentials which do not produce satisfactory agreement with experimental frequencies can provide accurate molecular dynamics. Vibrational analysis normally takes place at stable structures, as such vibrational frequencies provide a way of assessing how well the force field models the energy around the minimum energy structure.

Here we develop an empirical potential based upon the MM potential that is designed to predict the vibrational frequencies of carbon based materials. Analytical first and second derivatives of the MM potential have been implemented and the potential parameterised via a Monte-Carlo based Hessian matching approach. When combined with the empirical BPM it provides a fully empirical method for modelling the Raman spectroscopy of carbon nanotubes and graphene. The implementation of analytical first

and second derivatives allows accurate atomistic vibrational analysis and simulation of the Raman spectroscopy of systems with greater than 10,000 atoms. Subsequently, the Raman spectroscopy of graphene and carbon nanotubes with defects, junctions and nanocones is explored.

3.2 Development of Force-Field, Random Search Parameterisation

The MM potential has been used extensively to study the structure of metal clusters, as such several parameter sets already exist.[82–88] A parameterisation for carbon has been reported by Eggen *et al.*,[32] wherein the potential was fitted to the vibrational frequencies and elastic constants of diamond, to the cohesive energy and intra-layer spacing of graphite in addition to other structural data. The potential was then applied to study the structure of a wide range of carbon clusters and fullerenes. Vibrational frequencies for selected carbon clusters including C_{60} were computed, and it was found that low frequencies were underestimated and higher frequencies overestimated.

As was noted in the work of Eggen *et al.*, small carbon clusters and fullerenes will both have π-bonding electronic effects, which are missing in diamond which has only sp^3 carbons. Consequently, in order to describe the vibrational spectroscopy of carbon nanotubes and graphene-based materials correctly, it is necessary to revisit the parameterisation of the potential. The work of Hands *et al.*[89] is illustrative of force field based studies, and

assessed several existing force fields and developed a new force field wherein the 13 force constants contained within the force field were fitted to the experimental values for the Raman active vibrational modes. This type of model will naturally reproduce the data to which it was fitted (the optically accessible modes) and was able to account for the full spectrum, but what about the hundreds of other optically silent modes? What about taking into account that harmonic frequencies should be naturally overestimated by theory and shouldn't directly reproduce the experimental frequencies?

In order to construct a new set of parameters for the MM potential designed to accurately model the structure and vibrational frequencies of sp^2 based carbon materials, we have used a Monte-Carlo structure and Hessian-matching approach. The Hessian matrix is the key component for the computation of accurate vibrational frequencies and normal modes, and contains all the information required for vibrational analysis within the harmonic approximation. This approach provides a more rigorous fitting methodology than mentioned previously since it goes beyond Hands *et al.*, by considering the entire vibrational behaviour by including all modes rather than just those that can be seen experimentally. This is a similar idea to force-matching approaches, where an empirical potential is parameterised to replicate forces computed from quantum chemical calculations by a Monte-Carlo minimisation of the root mean square deviation (RMSD) between the forces.[90,91] Recently, the use of Hessian data in the parameterisation of force fields has been exploited by Grimme[92] with the aim of an accurate and specific potential for a single molecule in a particular electronic state with little transferability. The key advantages of this

approach is that we avoid any bias being introduced with respect to any specific vibrational modes being fitted, furthermore the mode re-ordering is allowed easily during the change in parameters during the fitting.

New parameters for the MM potential were determined by a Monte-Carlo based minimisation of the RMSD of the unscaled Hessian matrix for C_{60}, computed using DFT with the B3LYP exchange-correlation functional and 6-31G* basis set within the constraint that a low RMSD for the structure is also achieved. $\mathrm{RMSD}^{\mathrm{Hessian}}$ and $\mathrm{RMSD}^{\mathrm{Structure}}$ are computed by:

$$\mathrm{RMSD}^{\mathrm{Hessian}} = \sqrt{\frac{1}{3N \times 3N} \sum_{i}^{3N} \sum_{j}^{3N} (\mathbf{H}_{ij}^{DFT} - \mathbf{H}_{ij}^{MM})^2} \tag{3.1}$$

and

$$\mathrm{RMSD}^{\mathrm{Structure}} = \sqrt{\frac{1}{3N} \sum_{i}^{3N} (\mathbf{x}_{i}^{DFT} - \mathbf{x}_{i}^{MM})^2} \tag{3.2}$$

C_{60} was chosen since it captures many of the structural elements present in sp^2-based carbon materials, and it is sufficiently small for the calculation of the Hessian matrix using DFT. Previous studies have shown that the B3LYP/6-31G* level of theory provides a good description of the structure and vibrational frequencies of fullerenes.[93]

In the fitting, the parameter D in equations 2.9 and 2.10 was not varied from the value of 6.298 eV from the work of Eggen *et al.* Where this value corresponds to the typical bond energy of a carbon-carbon double bond. The c_i parameters were confined to the range -200 to $+200$,

the a_i parameters between 1.5 and 10.0, r_e was allowed to vary between 1.1 and 1.5 Å since this range contains acceptable values for the bond lengths of C_{60}. 10,000 sets of randomly chosen initial parameters were generated, and then for each of these sets of parameters, the $RMSD^{structure}$ and $RMSD^{Hessian}$ were minimised using the following procedure: Each parameter is perturbed randomly by an amount between -5 and $+5$ for the c_i coefficients and between -0.05 and 0.05 for the remaining parameters, and the change is accepted if both the $RMSD^{structure}$ and $RMSD^{Hessian}$ decrease. This was continued until there was no further decrease in $RMSD^{structure}$ and $RMSD^{Hessian}$, and was repeated three times for each starting condition. The 1200 sets of parameters with lowest $RMSD^{Hessian}$ that satisfied the condition $RMSD^{structure} < 0.03$ Å were refined further using a similar procedure with the magnitude of the variation in the parameters reduced by a factor of 100. The final results showed several sets of parameters with similarly low $RMSD^{structure}$ and $RMSD^{Hessian}$. These parameters were then tested in the simulation of a Raman spectrum for a nanotube. The final parameters chosen are shown in table 3.1, and correspond to $RMSD^{structure} = 0.014$ Å and $RMSD^{Hessian} = 0.37\ E_h$ Å^{-2}. It is currently difficult to judge the magnitude of $RMSD^{Hessian}$ with no other reference data to compare to in the literature unlike the $RMSD^{structure}$.

With regards to the new parameters shown in table 3.1 with the new potential referred to as MM^{Vib}, there is a significant reduction in the value of r_e between the original Murrell-Mottram potential for carbon and the new parameters reflecting the change from sp^3 to sp^2 carbons and the presence of carbon-carbon double bonds. Some of the c_i coefficients change

Table 3.1: Parameters for the Murrell-Mottram potential from the work of Eggen *et al.* (MM^{Eggen}) and the new parameters determined in this work (MM^{Vib}).

Parameter	MM^{Eggen}	MM^{Vib}
D/ eV	6.298	6.298
r_e/Å	1.570	1.313
a_2	8.200	7.428
a_3	8.200	8.072
c_0	8.087	7.788
c_1	-13.334	3.917
c_2	26.882	-17.503
c_3	51.646	51.427
c_4	12.164	99.263
c_5	51.629	39.772
c_6	25.697	70.505
c_7	5.964	73.262
c_8	7.306	3.831
c_9	2.208	65.696
c_{10}	13.707	85.307

significantly, however, the potential depends on the cumulative effect of these parameters and it is difficult to determine any physical relevance from the change in any one of these coefficients. The RMSD in the Hessian is significant, but as shown later it is sufficiently low to provide an accurate description of the vibrational frequencies of carbon nanotubes and graphene. The vibrational frequencies are computed within the harmonic

approximation, and it is well known that this leads to an overestimation of the vibrational frequencies. Consequently, it is customary to apply a linear scaling to computed harmonic frequencies. For B3LYP/6-31G* a scaling factor of about 0.96 is optimal,[55] for the frequencies computed with the re-parameterised MM^{Vib} potential we find a scaling factor of 0.90 to be suitable which is closer to the scaling factors used for Hartree-Fock theory calculations. We note that overestimating the experimental frequencies at the harmonic level is to be expected since if the calculations were extended to anharmonic frequencies, for example via vibrational perturbation theory, this would lead to a decrease in the computed frequencies.

3.3 Results

3.3.1 Structure

The new parameters from MM^{Vib} find carbon nanotubes and graphene to be stable structures as demonstrated by the absence of imaginary frequencies. The previous parameterisation of the MM potential for carbon did not produce sp^2 carbon as stable structures, but rather tetrahedrally distorted coordination of carbon atoms in a tubular arrangement. This is unsurprising since the parameters were fitted to the properties of diamond and its tendency to produce diamond is evident. For nanotubes with diameters greater than that of a (10,10) nanotube, the predicted C-C bond lengths are 1.43 Å, consistent with a value of approximately 1.427 Å observed in experiment. For small diameter nanotubes the strain arising from the high curvature results in a greater deviation in the bond lengths. For graphene the new potential gives bond lengths of 1.42 Å at the centre of a model

5 nm by 5 nm flake, again this compares well to literature values. At the edges of the flake, bonds lengths deviate from 1.42 Å with edge effects becoming more prominent and differentiation between the bond lengths of double and single bonds is evident. Overall, this shows that the parameters fitted to C_{60} are able to provide a reliable description of the minimum energy structures of large carbon nanotubes and graphene.

3.3.2 Experiment Vs Theoretical

The most important consideration for the empirical methodology presented here is whether it can successfully reproduce experimental results. Figure 3.1 shows the Raman spectrum computed with the empirical model along with a typical experimental spectrum of a carbon nanotube reported by Sanchez *et al.*[94] The experimental data is compared with a calculation using a pristine finite (6,6) 8 nm long nanotube consistent with experiment. The spectrum reported shows no evidence of a D-band (expected at $\sim$1300 cm^{-1}) since it is an essentially defect-free carbon nanotube as noted in the report. Firstly, the RBM is predicted accurately in comparison with the experimental RBM. The calculated frequency is at 301 cm^{-1} close to the experiment value at 295 cm^{-1}. In experiment the two G-band peaks lie at 1518 and 1591 cm^{-1} with a splitting $\Delta\omega_G = 73$ cm^{-1} compared with calculation at 1523 and 1610 cm^{-1} with a splitting of $\Delta\omega_G = 83$ cm^{-1}. Overtone bands at higher frequency than the G-band observed in experiment are not present in the fundamental harmonic frequency analysis presented here. The RBM and G-bands will be looked at in further detail in sections 3.3.3 and 3.3.4.

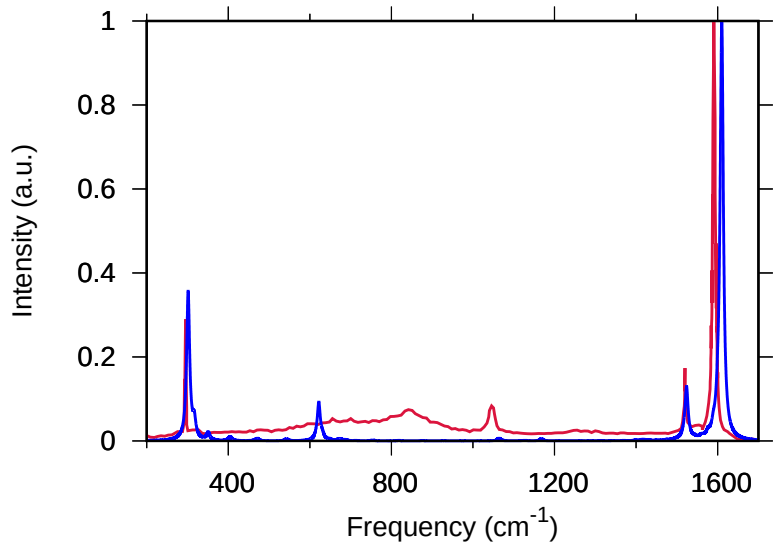


Figure 3.1: A comparison of a typical experimental Raman spectrum of a (6,6) carbon nanotube (red) compared with a simulated spectrum using MM^{Vib} and the BPM (blue).

Overall the relative intensities between the calculated bands match experiment quite well, even though the BPM parameters were designed for periodic systems. The calculated spectrum shows a potential intermediate frequency mode (IFM)[95–97] at 621 cm^{-1} with low intensity that is not observed in the experimental spectrum, IFMs are usually found between between 400-1100 cm^{-1} but are only seen under special circumstances, for example when surface enhanced Raman spectroscopy is used. There is a band seen at 1050 cm^{-1} in experiment. In the simulated spectra, there are bands with very low intensity nearby this band which could potentially be associated with modes that are perturbed by the platinum surface. In the experiment their intensities are being enhanced, which not considered in these calculations.

Another experimental comparison with the work of Souza *et al.*[98] is shown in figure 3.2. These Raman spectra were assigned to a sample made up of predominantly (12,9) and (10,9) semiconducting carbon nanotubes and are compared with there corresponding spectra simulated using MM^{Vib} with tube lengths of 8 nm. The RBMs of the (10,9) and (12,9) were assigned to 172 cm^{-1} and 190 cm^{-1}, and MM^{Vib} predicts frequencies of 175 cm^{-1} and 191 cm^{-1} in very good agreement. The experimental G-band frequencies for G^- and G^+ lie at 1567 and 1595 cm^{-1}, with a splitting of $\Delta\omega_G = 28$ cm^{-1}. MM^{Vib} for (12,9) nanotube predicts a G^- and G^+ at 1609 and 1638 cm^{-1} with a splitting of $\Delta\omega_G = 29$ cm^{-1} and for (10,9) predicts G^- and G^+ at 1599 and 1635 cm^{-1} with a splitting of $\Delta\omega_G = 36$ cm^{-1}. Overall the relative intensities between the calculated bands match experiment quite well with a small overestimation of the G-band but accurate splittings.

Overall the model successfully provides Raman spectra comparable with experiment. The model nanotubes used were 792 atoms ((6,6) 8 nm), 1491 atoms ((10,9) 8 nm) and 1332 atoms ((12,9) 8 nm), which wouldn't be possible by quantum mechanical calculations such as DFT. The errors seen in the bands were on the order of $\sim$15 cm^{-1} which is similar to what is usually expected with DFT methods. One noticeable feature of the RBM for finite nanotubes is that there is some distortion to the perfect radial expansion at the ends of the tube, while within a periodic (infinite) tube framework, the displacements of the atoms are perfectly radial and symmetrical, this is revisited later in section 4.2. A consequence of this is that the Raman intensities associated with the spectra for the finite tubes could lead to

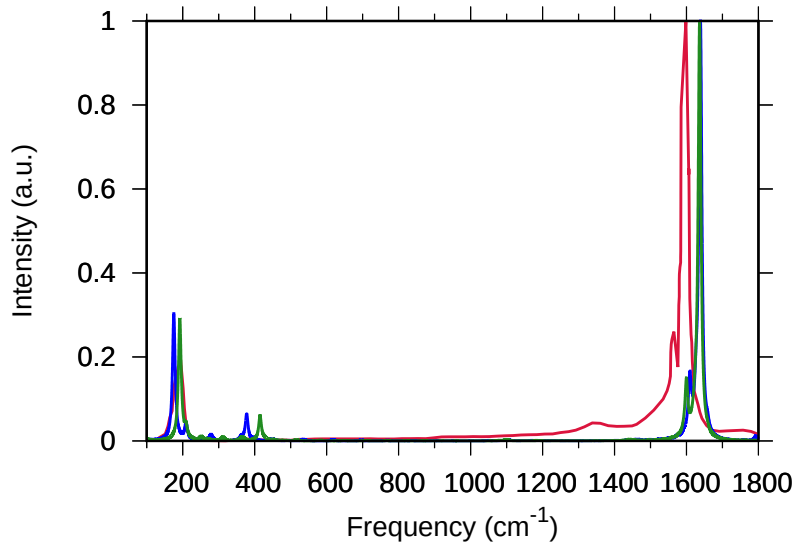


Figure 3.2: A comparison of a typical experimental Raman spectrum from a mixture of (12,9) and (10,9) carbon nanotubes (red) compared with the simulated spectra using MM^{Vib} and the BPM of (12,9) (blue) and (10,9) (green) nanotubes.

over/underestimations of the intensities by the BPM parameters that were parameterised based upon periodic (infinite tube) calculations.

An important aspect of experiment to comment here is that often resonant Raman is often employed.[23,99] In resonant Raman, the incident laser in experiment has a beam energy that coincides with that of an electronic transition of the carbon nanotube, this provides both an enhancement in intensities of particular modes such as the RBM and also allows specific indices of tubes to be chosen to target in a sample. The intensities may differ from those which are calculated using the BPM since it is a non-resonant theory, however, it does provide a good comparison regardless for

identifying and gaining insight into Raman active modes.

3.3.3 Radial Breathing Mode

The RBM is one of the most important modes in the Raman spectroscopy of carbon nanotubes. The RBM corresponds to the coherent expansion and contraction of carbon atoms in the radial direction as illustrated in figure 3.3, and the frequency of this mode is known to depend on the diameter of the carbon nanotube. This dependence comes from the fact

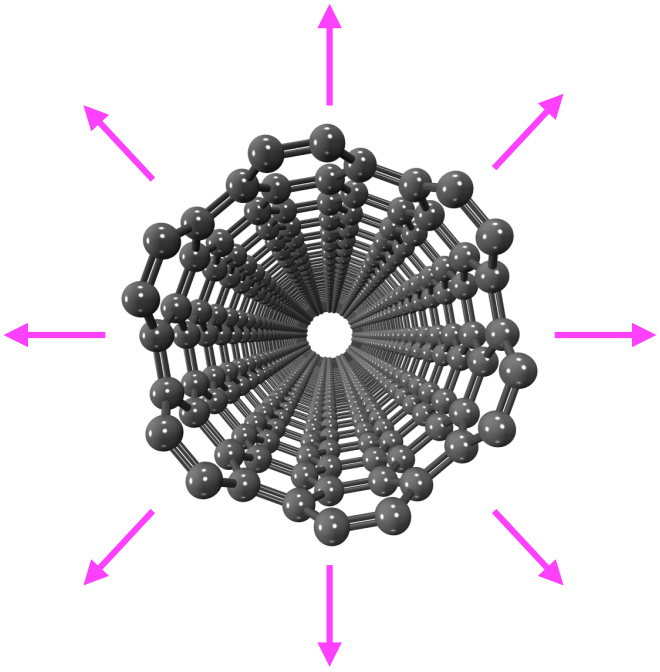


Figure 3.3: Representation of the radial breathing mode.

that the mass of all the carbon atoms along the circumferential direction is proportional to the diameter.[20] The RBM is commonly used to determine carbon nanotube diameters and their distributions in experimental samples. The frequency of the RBM is known to follow an inverse relationship with the diameter (d_t), the following empirical relationships are commonly used

in the literature:[100,101]

$$\omega_{RBM} = \frac{A}{d_t} \tag{3.3}$$

$$\omega_{RBM} = \frac{A}{d_t} + B \tag{3.4}$$

For ω_{RBM} in cm^{-1} and d_t in nm, A is known to lie between 220 and 260 nm cm^{-1} , and B typically has values 0-20 cm^{-1}.[100–102] Figure 3.4 shows the variation of the RBM frequency computed using MM^{Vib} with diameters for a set of nanotubes including both armchair and zig-zag motifs. Fitting

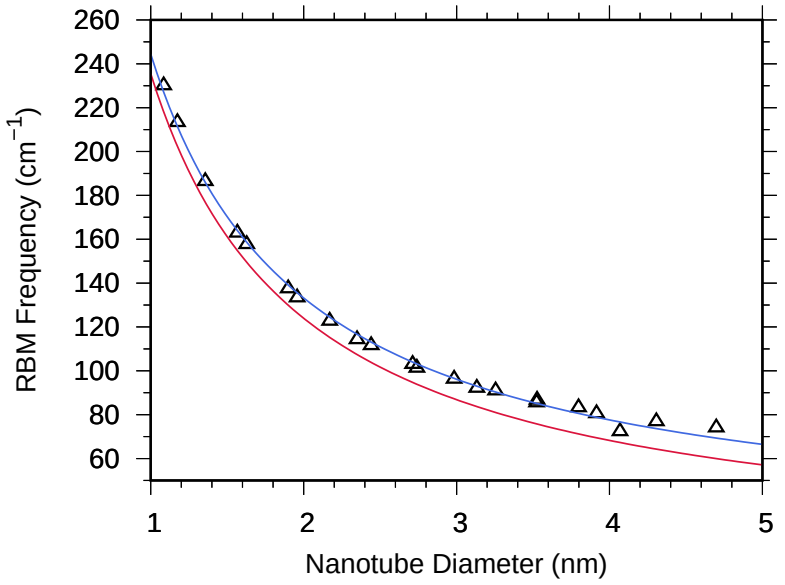


Figure 3.4: Variation of the ω_{RBM} with nanotube diameter. Triangles: calculated frequencies with MM^{Vib}, blue line: $\omega_{RBM} = \frac{222.0}{d_t} + 21.5$, red line: $\omega_{RBM} = \frac{223.5}{d_t} + 12.5$.

of these frequencies to equation 3.3 gives a value of 264 nm cm^{-1} for A and to equation 3.4 gives values of $A = 222$ nm cm^{-1} and $B = 21$ cm^{-1}. Also shown are the RBM frequencies given by a commonly used empirical formula $\omega_{RBM} = \frac{223.5}{d_t} + 12.5$. This shows that the potential accurately describes the diameter dependence of the RBM mode observed in experiment,

although the frequencies are a little too high, it provides a good indication that the new potential is modelling the interactions accurately. The calculations also show that the frequency of the RBM converges rapidly with the length of the tube and for nanotubes longer than 10 nm there is little change in the computed RBM frequency.

Table 3.2: A table of RBM frequencies (cm^{-1}) calculated from MM^{Vib} compared with experimentally measured values of assigned carbon nanotubes with index (n, m).[103]

(n, m)	MM^{Vib}	Exp
(18,6)	147	144
(21,0)	151	148
(12,12)	153	151
(16,7)	155	154
(17,5)	158	156
(13,10)	158	156
(18,3)	161	158
(19,1)	162	160
(14,8)	164	161
(11,11)	167	164
(15,6)	169	165
(16,4)	173	169
(17,2)	175	174
(18,0)	176	176
(14,1)	216	210
(11,4)	233	229
(10,5)	238	237
(8,7)	241	239

Table 3.2 shows a comparison of RBM frequencies computed using MM^{Vib} and measured experimentally including a variety of chiral and non-chiral carbon nanotubes. Generally there is good agreement with the high-

est error being 6 cm^{-1} and a mean absolute error between experimental and calculated frequencies of 2.6 cm^{-1}.

3.3.4 G-Band Modes

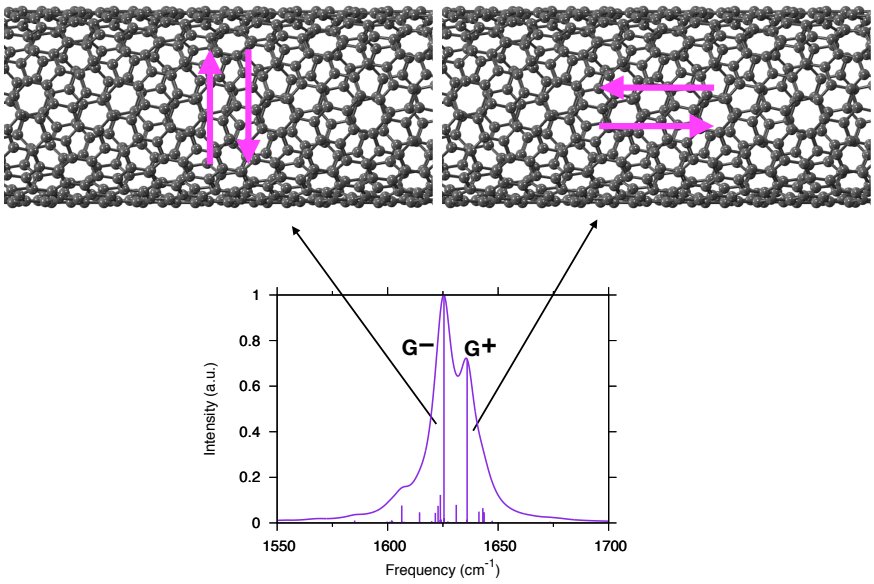
As mentioned previously the G-band in carbon nanotubes has two distinct bands in the 1550 and 1590 cm^{-1} region, these are often called G^- and G^+, where the G^+ corresponds to the higher frequency band and G^- to the lower. The vibrational modes for these bands are associated with in-plane carbon motions. These modes are polarised along the axis and along the tube circumference and are often, respectively, referred to as the longitudinal optical mode, LO, and tangential optical mode, TO. The G^+ peak is usually more intense than the G^-, and its position is largely independent of the tube's diameter, whereas the position of the G^- peak decreases with decreasing tube diameters.

The splitting of the G-band into LO and TO is a result of the different force constants of the chemical bonds along the tube axis and the tube circumference. Consequently, this leads to two different vibrational frequencies for modes polarised along these two directions. From the perspective of rolling graphene to a cylindrical carbon nanotube, the geometrical distortion leads to a change in atomic separation, loss of C-C bond planarity and mixing of σ and π states. The Raman spectra of carbon nanotubes can be characterised by the presence of these two distinct features.

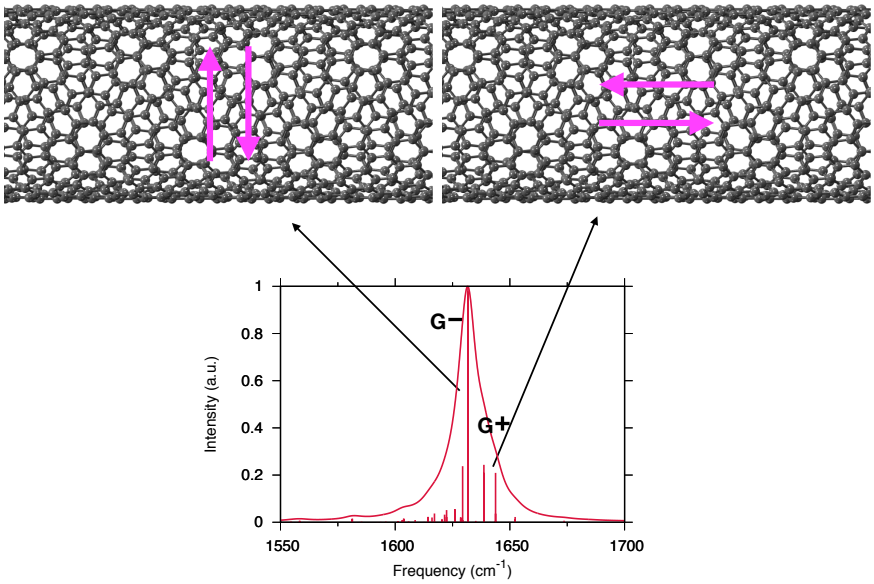
For semiconducting tubes, the G^- corresponds the TO and the G^+ to the LO. The splitting between these two modes is usually explained to

be a result of curvature mentioned previously, where σ - π mixing of C-C bonds along the circumference results in softening of the TO mode relative to the LO mode.[23]

For metallic tubes the G^- corresponds to the LO mode, and the G^+ corresponds the TO mode, the opposite to semiconducting tubes. The splitting between these modes tends to be larger than semiconducting tubes. The reason the LO mode is at a lower frequency is a result of electronic structure effects (or more specifically confinement resulting quantization of the electronic wavefunction due to the curvature) with electron-phonon coupling becoming the dominant effects on the G-band modes, not the mechanical affect of curvature like in semiconducting tubes.[104] This case will be a challenge for the potential developed here since no electronic structure effects are accounted for, apart from its implicit effect from the initial fitting to DFT calculations and the potential is technically fitted to C_{60} which is not metallic.



(a) Semiconducting CNT (15,4) 5 nm.



(b) Metallic CNT (18,3) 5nm.

Figure 3.5: Computed G-band spectra of a metallic and semiconducting carbon nanotube and their relevant G-band vibrational modes.

Figure 3.5 shows the computed G-band and corresponding vibrational modes for two nanotubes of different indices, metallic (18,3) and semiconducting (15,4). The semiconducting case shows the correct mode ordering that we expect, when the TO mode is lower in energy than the LO mode. However, in the case of the metallic tube, we can see incorrect ordering, the TO mode is lower than the LO mode. This is most likely a result of the fact the empirical potential is simply incapable of modelling electronic structure effects like the electron-phonon coupling, which has been rationalised as the origin of the lower LO mode relative to the TO. The use of more complex models by inclusion of hybridisation affects in the potential may alleviate this effect, but since this effect is quantum mechanical, tight binding methods may be more appropriate for this case. In contrast, the semiconducting tube's G-bands are simpler and purely dependent on the curvature/mechanical properties which are captured easily by the potential.

The frequency of both G-bands for semiconducting components changes with the diameter of the nanotube, and this is illustrated in figure 3.6 which shows the variation of the frequency of the G^- and G^+ modes with nanotube diameter for a semiconducting tube. The G^- mode is more sensitive to diameter as expected from curvature softening due to its structure, and as the tube diameter increases the two components of the G-band become closer in frequency. This convergence is observed experimentally, however the small variation in the G^+ frequency could be an artefact of the finite size effects since normally it is observed to be constant in experimental studies.[104]

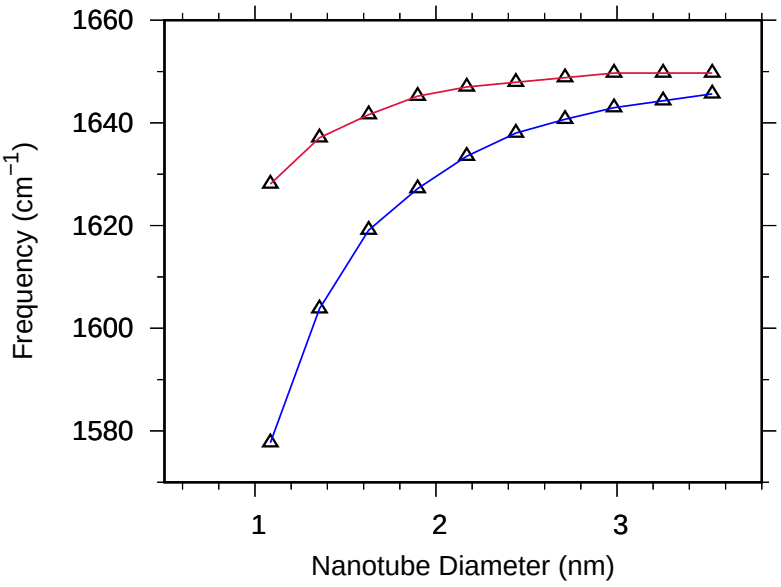


Figure 3.6: Variation of the frequency of the G^+ (red) and G^- (blue) bands with nanotube diameter.

3.3.5 Vibrational Density of States

Calculations of Raman spectra only probe the small number of vibrational modes that have significant intensity. In contrast, the vibrational density of states (VDOS) provides a measure of the complete vibrational spectrum. Unfortunately, experimentally it is a highly challenging measurement and as a consequence scarcely reported in the literature. For finite nanotubes of sufficient length, the calculated VDOS can approach bulk behaviour (see chapter 4.2), hence we have used an extremely long tube of 60 nm here. Figure 3.7 shows the computed VDOS for a (10,10) nanotube with length 60 nm that has 9720 atoms, and a broadening using Lorentzian functions of 20 cm^{-1} is applied. This can be compared with the VDOS measured in experiment from the work of Dresselhaus and Eklund[105] which also corresponds to (10,10) nanotubes. We note that the calculations represent a

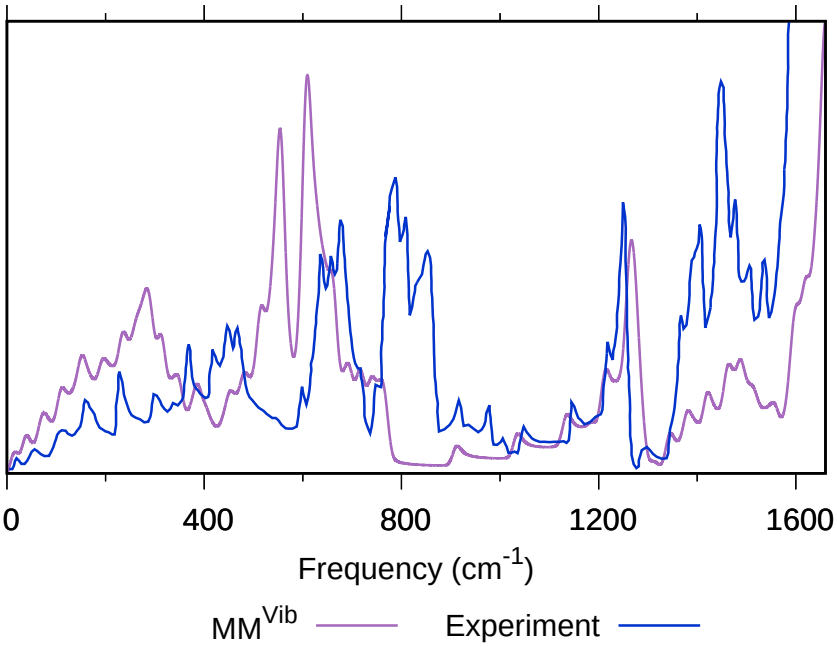


Figure 3.7: The computed VDOS of (10,10) Carbon Nanotubes compared with experimental VDOS by Ekland *et al.*[105]

single pristine carbon nanotube while the experiments are for a nanotube bundle. In general, the calculations qualitatively reproduce the VDOS profile observed in experiment. In some regions of the spectrum, some notable differences are revealed. In particular, the two distinct peaks in the 600 cm^{-1} to 900 cm^{-1} region are predicted to lie at a lower frequency. There are also differences in the 1400 cm^{-1} to 1600 cm^{-1} region. However, the potential is performing reasonably well over the frequency range, although some features are slightly shifted. This may be due to interactions between nanotubes in the bundles changing the frequencies. More importantly, however, it should be noted that this is a metallic tube, and as shown in section 3.3.4 electronic effects can be significant for these tubes. There is currently lack of ab initio data of VDOS analysing the overall affects of

electronic structure on vibrational properties on carbon nanotubes, most efforts have focused primarily on rationalising the ordering of the LO and TO modes.[104]

3.3.6 Graphene

Figure 3.8 shows the comparison of Raman spectra computed using MM^{Vib} and a typical experimental spectrum for graphene. The calculations correspond to a finite 5 nm x 5 nm graphene sheet. There are much fewer features in Raman spectra for graphene, and the spectra are dominated by the G-band. The calculations predict a spectrum in agreement with exper-

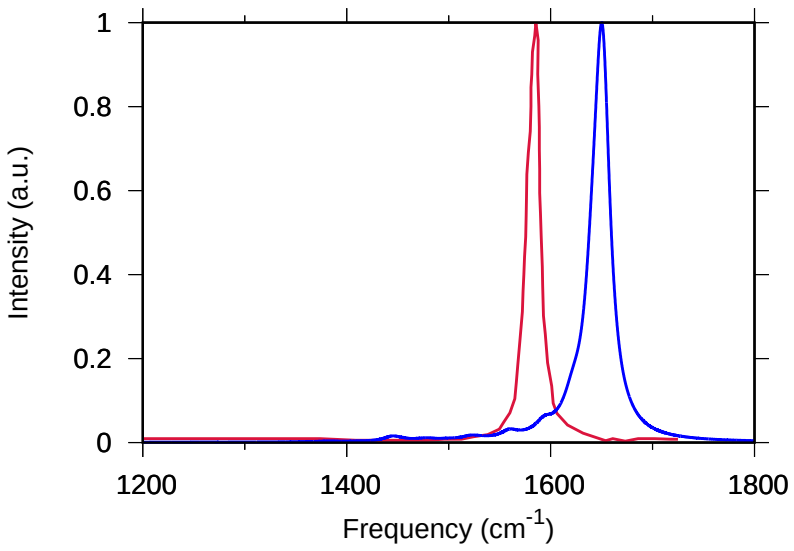


Figure 3.8: A comparison of a typical experimental Raman spectrum of graphene[99] (blue) compared with a simulated spectrum using MM^{Vib} and the BPM (red).

iment, the frequency of the G-band is calculated to be about 1650 cm^{-1} compared with 1585 cm^{-1} in experiment. The agreement with experiment

for this band is not as accurate as found for the carbon nanotubes and may reflect the nature of the fitting of the potential to C_{60}, which is a more appropriate model for nanotubes due to its curved nature than for a flat graphene sheet. However, this does demonstrate a level of transferability. It is also important to note that graphene Raman spectra are often measured on a substrate like silicon dioxide. Often graphene-substrate interaction can lead to changes in its electron structure and distortion of its planar hexagonal geometry including bond lengths with can lead to perturbations in its Raman spectrum.[106,107]

3.3.7 Stone-Wales Defects

The Stone-Wales (SW) rearrangement is 90° rotation of a single carbon-carbon bond (see figure 3.9) which can lead to the formation of two 5-membered rings and two 7-membered rings.[108]

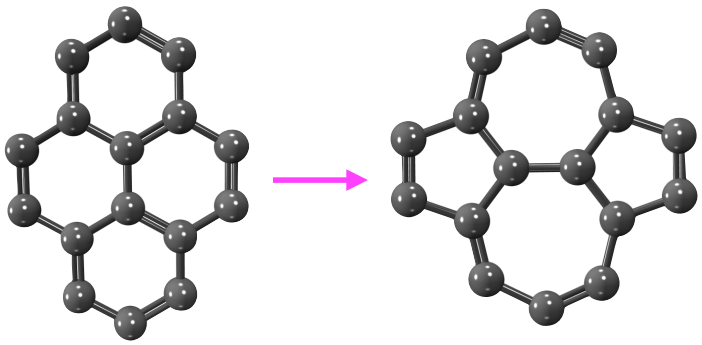
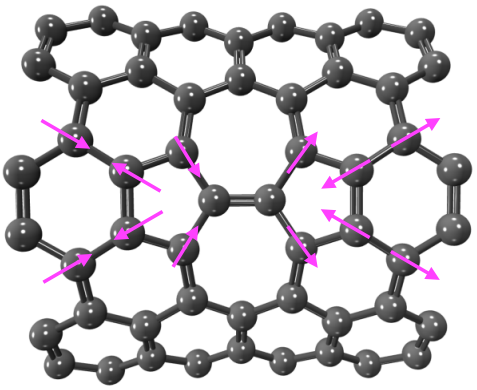


Figure 3.9: A Stone-Wales defect from the 90° rotation of a C-C bond.

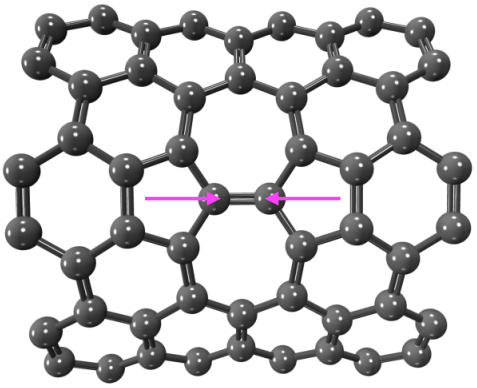
The SW rearrangement is a common defect found in carbon nanomate-

rials and it has been proposed that a localised vibrational mode associated with the defect may form the basis for monitoring the formation of these defects in nanotube growth/formation.[109] Consequently, it is of interest to study how the presence of these defects is reflected in Raman spectroscopy.

For carbon nanotubes, the inclusion of a single SW defect leads to some distinct highly localised modes based purely around the defect area. These defects are illustrated in figure 3.10.



(a) Localised Stone-Wales mode.



(b) Stone-Wales C-C stretching mode.

Figure 3.10: Example localised vibrational modes around a Stone-Wales defect in a (10,10) carbon nanotube.

The computed Raman spectra for (10,10) nanotube are shown in figures 3.11 and 3.14. The first type of vibrational mode lies at ∼1610 cm^{-1} and

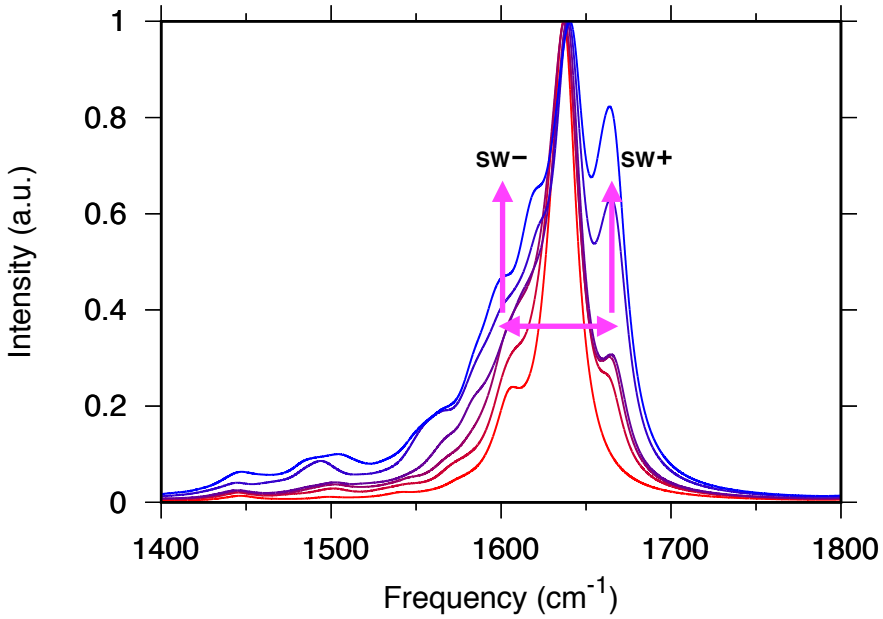


Figure 3.11: Raman spectra of (10,10) nanotube G-band with increasing number of Stone-Wales defects from red being pristine to blue containing 5 defects.

∼1665 cm^{-1} around the G-band in a (10,10) nanotube and is associated with stretching modes of the pentagon defect and these modes correspond local vibrations which just like the G-band vibrate along the carbon nanotube axis and perpendicular to it and as such have been labelled as SW^{-} and SW^{+}, respectively, and are shown in figure 3.12. These modes lead to broadening of the G-band as the intensity of SW^{-} and SW^{+} increases as more SW defects are included in the nanotube. The second most distinct mode corresponds to the C-C stretching mode between the two pentagon defects and is calculated to lie at 1931 cm^{-1} in a (10,10) nanotube. The computed frequency of this mode is consistent with previous work[109] where

the C-C stretching mode between the pentagon defects was computed to lie at 1962 cm^{-1} in DFT based calculations on a narrower diameter (3,3) nanotube. The computed spectra show the effect of the presence of the SW defect on the computed Raman spectra.

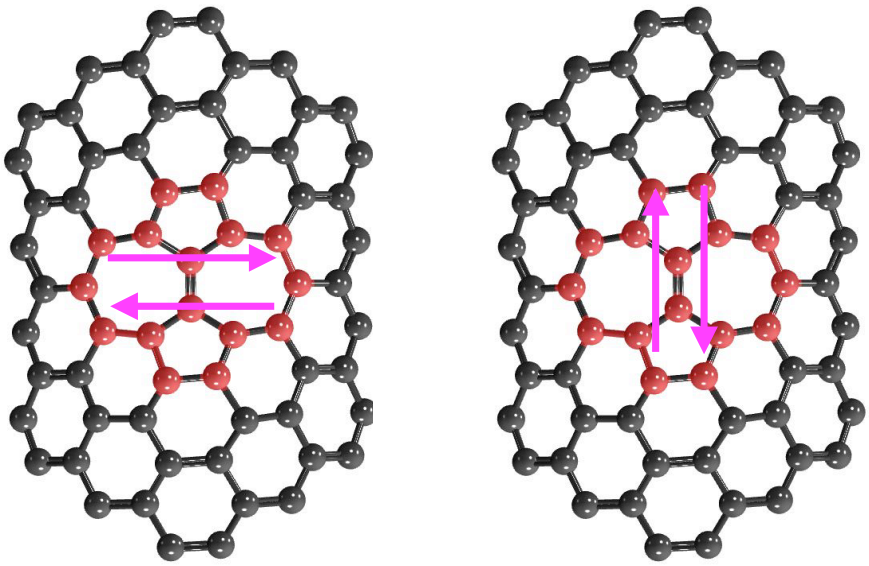


Figure 3.12: Corresponding vibrational localised modes of SW^+ and SW^- bands.

The frequency of the RBM is not affected by the inclusion of the SW defect at low concentration, and we find that the variation of the RBM frequency with diameter is relatively unaffected as shown in figure 3.13. The most significant effect is a small change in A in its diameter relationship, but the $1/d_t$ dependence is still observed. The small variance of the RBM frequency to the presence of a SW defect was also observed in periodic tight binding density functional theory based calculations on a (7,0) nanotube.[80] However, the Raman intensity of this mode is broadened significantly with

higher concentrations of the defect, and the single RBM becomes a collection of Raman active modes in the position of the original RBM (see figure 3.14), these modes are not well resolved after the Lorentzian broadening, reflecting what is likely to be observed experimentally.

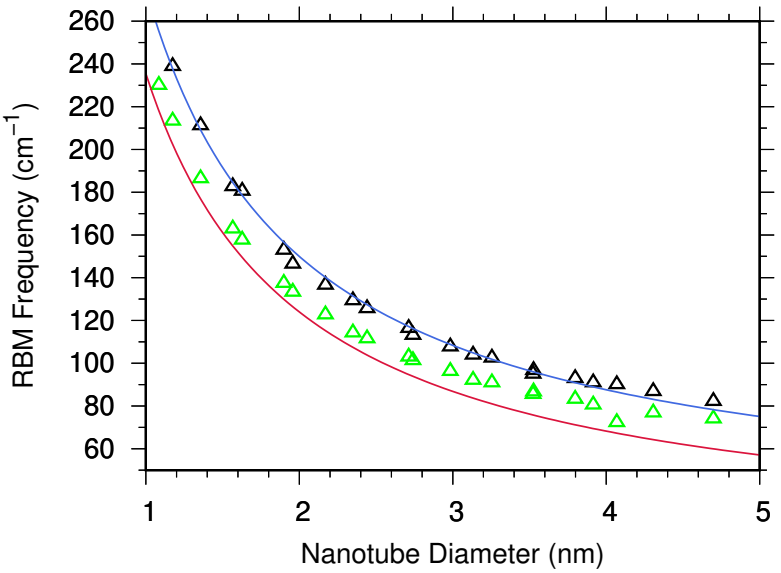


Figure 3.13: Variation of the ω_{RBM} with nanotube diameter. Green triangles: pristine nanotube RBM frequencies, black triangles: calculated SW defect carbon nanotube psuedo-RBM frequencies, blue line: $\omega_{psuedo-RBM} = \frac{249.6}{d_t} + 25.1$, red line: $\omega_{RBM} = \frac{223.5}{d_t} + 12.5$.

.

For graphene, the inclusion of a SW defect leads to long-range buckling in a graphene sheet as shown in figure 3.15. This long-range relaxation effect has been noted and seen in previous investigations[110] where semi-empirical potentials were employed to study SW defects and rationalised to be a mechanism for reducing strain. It was found in these calculations

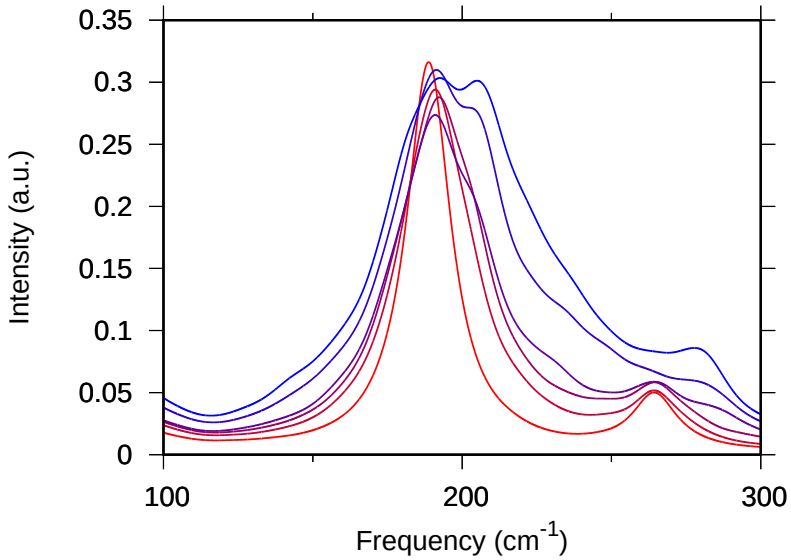


Figure 3.14: Raman spectra of a (10,10) carbon nanotube RBM with increasing number of Stone-Wales defects from red being pristine to blue containing 5 defects.

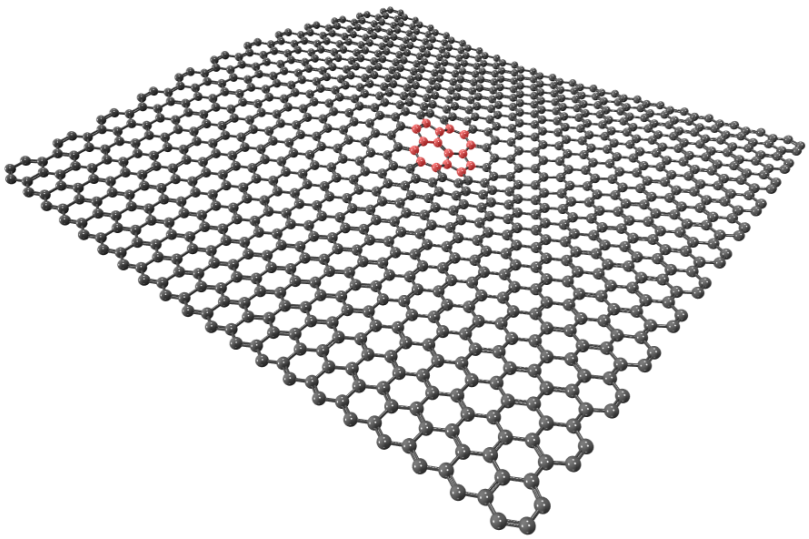


Figure 3.15: The buckling effect of a single Stone-Wales defect in graphene.

that this buckling range can be over 30 Å with periodic boundaries. The simulations here use a finite model showing a similar effect. The pentagon

defects lead to an additional band at higher energy than the G-band as shown in figure 3.16, although the separation is 15 cm^{-1} which is smaller than for the nanotube and so this band is less distinct from the G-band. The C-C stretching mode between the pentagons lies at 1922 cm^{-1} which is lower than calculated for the nanotube. The presence of these new bands in the Raman spectroscopy of nanotubes can provide evidence for the presence of SW defects in graphene samples.[111] Further details can be found elsewhere in *Carbon*, 2017, **113**, 299-308.[112]

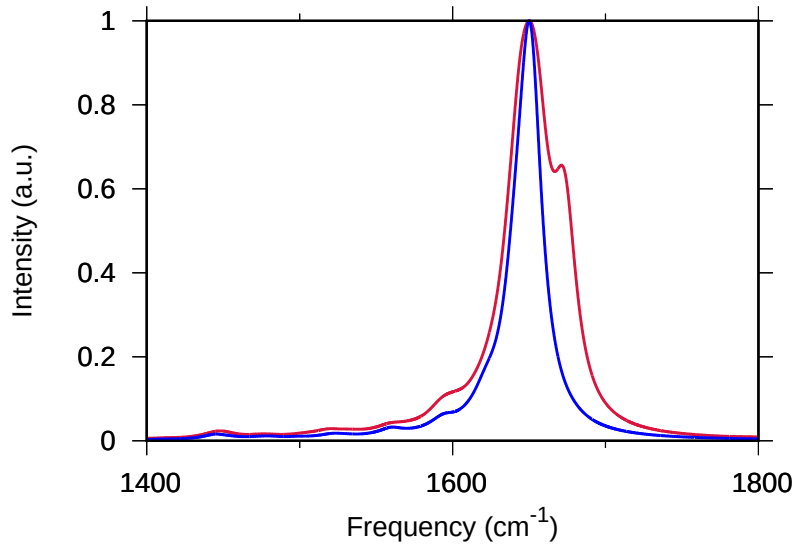


Figure 3.16: Raman spectra of pristine graphene (blue) and graphene with a Stone-Wales defect (red).

3.3.8 Carbon Nanotube Junctions

Junctions are points where two carbon nanotubes of two different chiralities or diameters meet. The connection between two or more different carbon nanotubes is an important step in the development of carbon

nanotube-based electronic devices and nano-scale circuits with new synthetic approaches being developed to produced these structures in a controlled way.[113] Here we look at the Raman spectroscopy of these systems and to see how the presence of a junction manifests itself in its Raman spectrum.

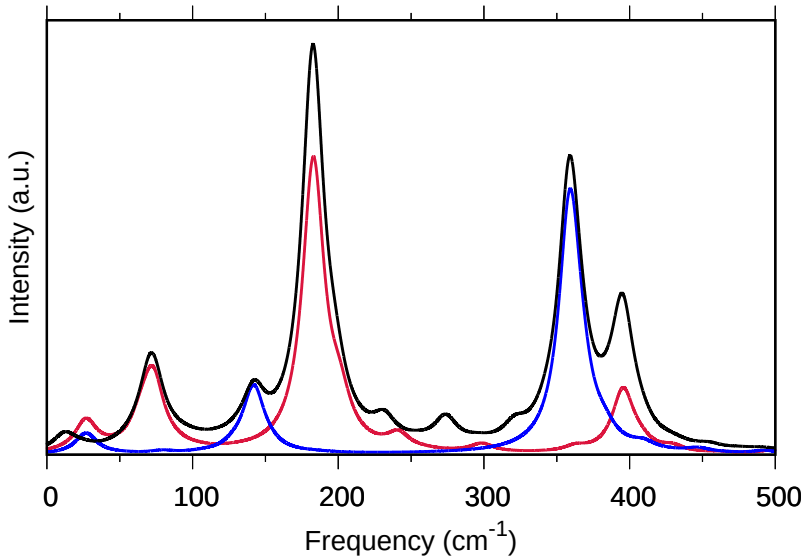


Figure 3.17: A (10,10) to (5,5) non-concentric nanotube junction.

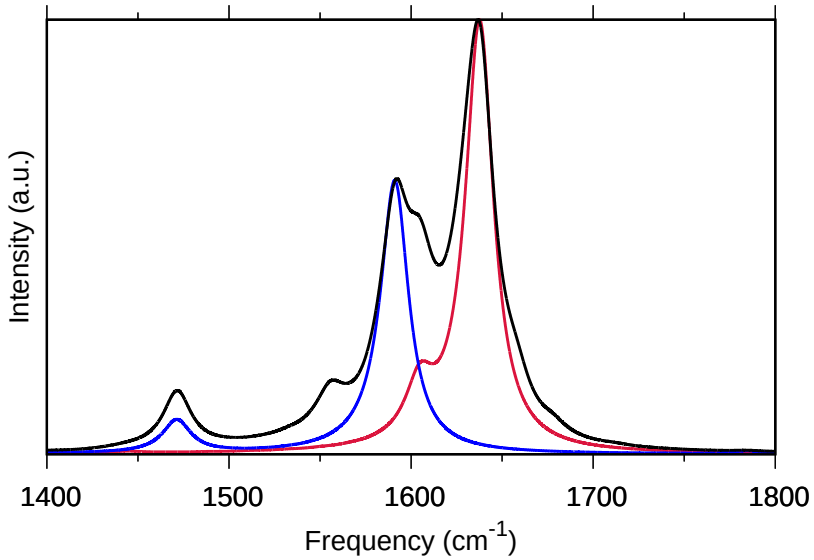
The junction modelled here, shown in figure 3.17, is non-concentric between a (10,10) and (5,5) nanotube, and was generated via the ConTub v1.0 program.[114] Figure 3.18 also shows the computed Raman spectra for the junction system in addition to the Raman spectra for the individual nanotubes. For this junction, the separate nanotubes have distinct RBMs and G-bands, and the resulting Raman spectrum is very similar to a superposition of the Raman spectra for the individual tubes. This indicates that there is little coupling between the vibrational modes of the two nanotubes and they simply act as two independent nanotubes. Vibrational modes associated with the join region between the two carbon nanotubes lie between 1640 and 1670 cm^{-1} which corresponds to the tail of the G-band, however it is difficult to differentiate them from the G-band. The join region between the two nanotubes is constructed from hexagons and no pentagon defects are introduced. Consequently, bands associated with pentagon defects are not observed in this case. The most notable change however in the G-band region is the emergence of a weak band at 1555 cm^{-1} which corresponds to the TO mode which has been shifted up by $\sim$80 cm^{-1}, the weak band

at 1471 cm^{-1} corresponds to a collection of planar modes which have a mixture of TO and LO character.

Other combinations of junctions were also considered including (10,10) to (10,0), with a pentagonal defect for the junction. The same result of a superposition of spectra on the component nanotubes was also seen with a pentagonal mode being indistinguishable owing to its low intensity and overlap with the G-band. Furthermore, modes associated with the join region appeared between 1640 and 1670 cm^{-1}. However, no significant shifts in the G-band were observed.



(a) Raman spectra in 0-500 cm^{-1}.



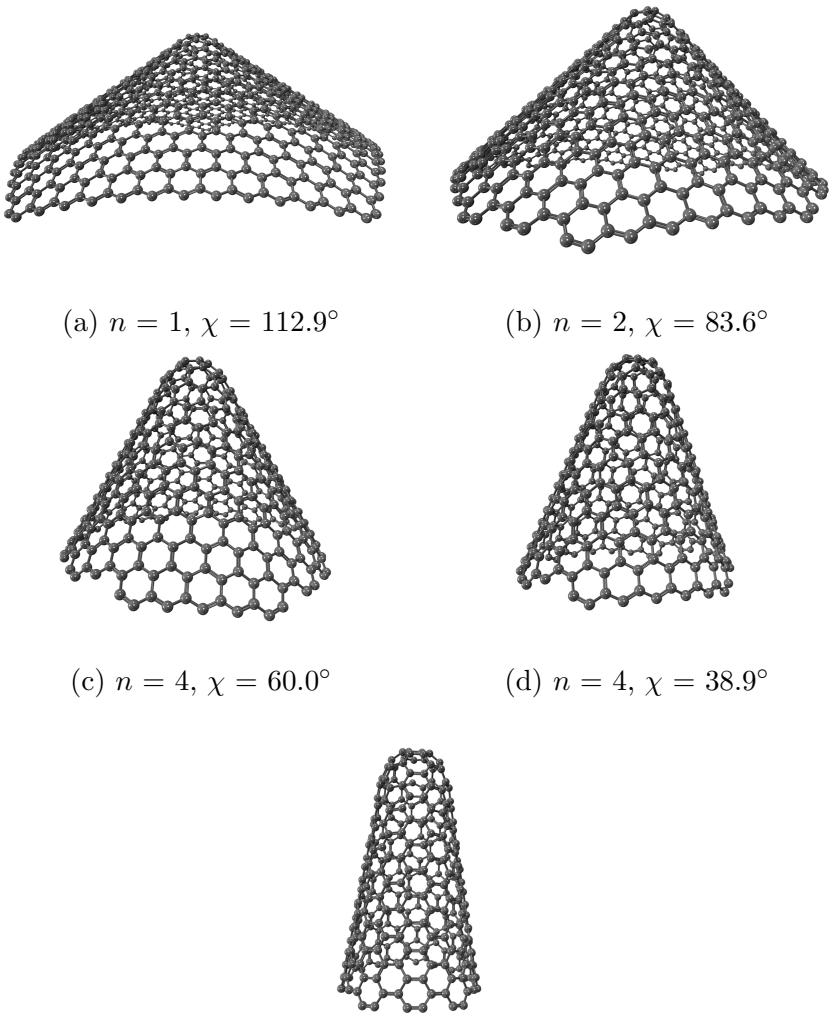
(b) Raman spectra in 1400-1800 cm^{-1}.

Figure 3.18: Computed Raman spectra of (10,10) to (5,5) non-concentric junction (black) and its component nanotubes (10,10)(red) and (5,5)(blue).

3.3.9 Carbon Nanocones

Carbon nanocones are conical carbon nanostructures, which can be thought as curved graphite sheets formed as open cones. These cones are constructed by cutting out sections of graphene at $n \times 60^\circ$ ($n = 1$ - 5) intervals and connecting the resultant edges (shown in figure 3.19). The strain at the cone apex results in n pentagons with apex angles(χ) of 112.9°, 83.6°, 60.0°, 38.9° and 19.2°.[115] Recent research in nanocones has been in the application of these structures for field emission devices exploiting their electronic properties[116,117] and as tips in atomic force microscopy.[118]

There are currently very few studies into the Raman spectroscopy of these systems, however a study by Jorio *et al.*[119] utilised the shift in G-band of these systems to map out the strain over a nanocone through Raman imaging. In this study of nanocones, we examine the lower end of the Raman spectrum to investigate the changes with respect to the apex angle.



(a) $n = 1$, $\chi = 112.9°$

(b) $n = 2$, $\chi = 83.6°$

(c) $n = 4$, $\chi = 60.0°$

(d) $n = 4$, $\chi = 38.9°$

(e) $n = 5$, $\chi = 19.2°$

Figure 3.19: Carbon nanocone structures with apex pentagon number, n and apex angle, χ.

Figure 3.20, shows the Raman spectra of nanocones in the 0 - 400 cm^{-1} region. Here the highest intensity mode in this region corresponds to a conical breathing mode (CBM) in the case of 19.2° ($n = 1$) this is a pure breathing mode as shown in figure 3.21a, or a pseudo-CBM for $\chi = 38.9$ - 112.9° ($n = 2$ - 5), an example is shown in figure 3.21b for apex angle 38.9° ($n = 2$). The likely reason that $n = 1$ has a pure CBM comes from the fact its tight apex makes this structure very similar to a cylinder like

a carbon nanotube, so the mode is almost an RBM.

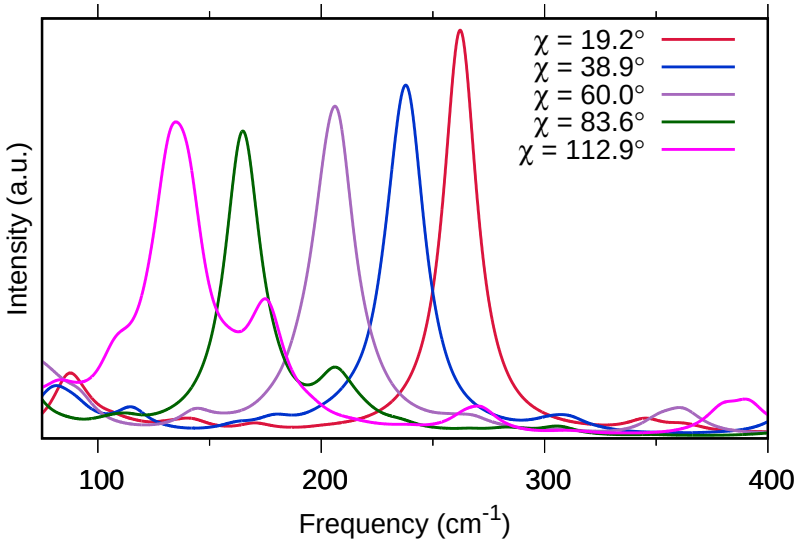


Figure 3.20: Computed Raman spectra of carbon nanocone for $\chi = 19.2$ - 112.9°.



(a) $n = 1$, $\chi = 19.2°$ (b) $n = 2$, $\chi = 38.9°$

Figure 3.21: Carbon nanocone CBMs where a) $\chi = 19.2°$ and b) $\chi = 38.9°$.

Figure 3.22, shows the CBM as a function of apex angle, χ. The frequency of this mode has a linear relationship with apex angle and a linear fitting easily describes this with following equation $\omega_{CBM} = -1.41\chi +$

289.54. Such a relationship could allow for the assignment of carbon nanocones in experiment and determination of distributions.

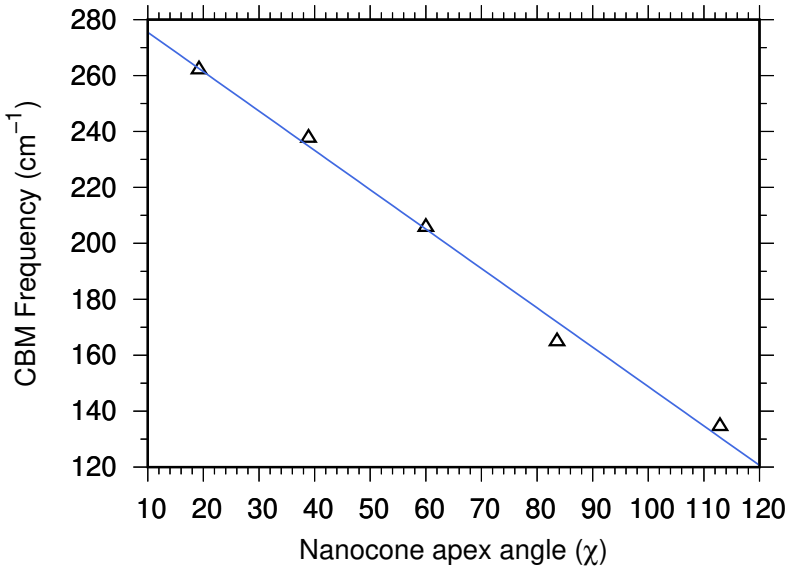


Figure 3.22: Variation of the ω_{CBM} with nanocone apex angle. Triangles: calculated frequencies with MM^{Vib}, blue line: $\omega_{CBM} = -1.41\chi + 289.54$

The G-band positions also shifts with angle, with it varying between 1613 cm^{-1} for $\chi = 19.2°$ and quickly converges to 1648 cm^{-1} for $\chi = 19.2°$. This is unsurprising as we found from MM^{Vib} previously that a typical nanotubes G-band (G$^+$) sits at 1610 cm^{-1} as such small angle cones have structures that are closer to a cylinder have a G-band frequency like that of carbon nanotubes, whereas those with wider angles tend to have much flatter structure close to that of graphene. The relative intensities of the CBM to G-Band is similar to that of a carbon nanotube's RBM to G-band.

3.3.10 Conclusions

The Murrell-Mottram potential has been parameterised to model the vibrational spectroscopy of carbon-based materials such as carbon nanotubes and graphene via a Monte-Carlo based minimisation of the RMSD of the DFT Hessian matrix of C_{60} fullerene. When combined with the bond polarisability model the resulting potential provides a method to simulate the non-resonant Raman spectroscopy that can be applied to systems with thousands of atoms. For carbon nanotubes, the computed Raman spectra accurately reproduce experimental observations. The known dependence of the RBM with the diameter of the nanotube and the nature of the vibrational modes corresponding to the G-band are reproduced, although ordering is incorrect for metallic tubes where electronic structure effects become significant, and a satisfactory approximation to the VDOS is obtained. The effect of Stone-Wales defects on the Raman spectroscopy of carbon nanotubes and graphene has been explored, and new bands are observed that arise from new localised vibrational modes associated with the defect. Carbon nanotube junctions have also been studied and it is shown that the resulting Raman spectra correspond to a superposition of the spectra for the individual nanotubes. Carbon nanocones were shown to have a Raman active conical breathing mode which depends linearly on the apex angle of the nanocone. Overall we have demonstrated that is it possible to simulate the vibrational spectroscopy of carbon nanomaterials using a fully empirical method, allowing accurate spectra to be calculated quickly for large systems which are not affordable with current quantum chemical based methods.

Chapter 4

Modelling Methods: Periodic, Finite or Tethered?

In this chapter we investigate three different approaches to model carbon nanomaterials, namely finite, periodic and tethered in simulations when using empirical potentials. This can be a critical decision and can often depend on what is being modelled with each method having its own advantages and disadvantages. Usually, these decisions are based on the computational cost, the effect of edges and whether bulk or surface properties are desired (or need inclusion). Here we examine these scenarios and their affect on computing the vibrational properties of carbon nanomaterials as well inferring their effect on the overall dynamics of a system.

4.1 Introduction

There are several approaches that can be used to model carbon nanomaterials and each method can potentially impact the results depending on

what is being studied. At the highest level, there is a choice between continuum models and atomistic models. Continuum models are attractive for their low simulation cost of mechanical properties, however, they lack the detailed instrinsic properties of nanotube chirality, and don't account for forces acting on the individual atoms.[120] In this work, we focus on the use of atomistic models in the context of computing vibrational spectroscopy. Here the key choice for carbon nanomaterials is how the edges or ends of the system are treated. The first which was used in the preceding chapter is finite modelling, when the entire system is modelled in a simulation with its edges being present and all atoms are free to move around in space. A second approach is tethered modelling, which is the same as finite except that edge atoms are assigned infinite mass, which effectively fixes the nanotubes/graphene in place in free space. Lastly is periodic modelling, where the entire material is approximated by using a small repetitive representative part called the unit cell using periodic boundary conditions (PBCs). PBCs allow us to approximate an infinite number of unit cells and each cell interacts with its neighbour, this allows us to model carbon nanomaterials as "bulk" giving a better macroscopic representation of its properties. Most notably the biggest difference between periodic and finite method is the absence of edges and the question of how well the finite represents the bulk.

Although here we focus primarily on vibrational spectroscopy and dynamics, these effects can potentially be significant for other simulation objectives. Such as modelling defects, encapsulation and the reactions of inorganic and organic molecules in carbon nanotubes.[121] Numerous ques-

tions arise for each of these scenarios: What is the interaction of defects in periodic simulation and is the unit cell big enough to eliminate this? How different is the stacking order (or angles) of molecules when periodic conditions are used rather than a finite nanotube? Is there a significant difference in energetics in a periodic tube vs finite? Do the properties of a finite simulation approach the periodic at large enough scale whilst preserving any significant effects of edges?

The effect of finite system size is often assessed by performing several calculations with successively larger systems sizes and checking the convergence with respect to the properties of interest. Another factor that requires consideration is highlighted by a recent study by Kotakoski *et al.*[122] is that electronic and mechanical effects can give rise to long-range interactions between single vacancies in carbon nanotubes, which may govern the migration of vacancies. This raises further questions of how these types of interactions manifest in periodically repeated infinite (usually assumed to be non-interacting) and finite models. Furthermore, studies by Ding *et al.*[123] proposed that defects in single wall carbon nanotubes have better stability towards the ends of single wall carbon nanotubes something that is completely neglected in periodic simulation. Similarly, other studies which looked at the monovacancy in graphene have also focused purely on edge effects and found the position of vacancy at the edge was found to be energetically more favourable, and is linked to graphene's self-healing diffusion mechanism to the edge.[124]

With the previous examples in mind, it is very desirable to understand

the effect of the different simulations scenarios on the vibrational spectroscopy of carbon nanomaterial systems. Periodic simulations can provide computational savings but it's important to be able to understand both the advantages and disadvantages as well as when they are appropriate to use. It's evident from previous studies that consideration of these effects can have a large effect on the outcome of the results and conclusions made.

4.2 Nanotubes

In the case of carbon nanotubes, the predominant difference which affects the modelling scenarios described in the previous section relates to the size of system, more specifically the length of the model nanotube used in simulation. It is important to note at this point that the smallest unit cell for a carbon nanotube is not the same as those used in the electronic structure methods. This is due to the form and the range of the MM^{Vib} potential requiring at least 4 Å. Here we first investigate the effects and convergence of the main Raman bands with respect to nanotube length using each of the modelling methods.

Figures 4.1 and 4.2 show the variation of the G-band frequency with respect to length using the three modelling methods. The frequency of the G-band does not show a strong dependence on the length of the carbon nanotube and converges very quickly at 5 nm for each of the three different modelling methods. As expected the periodic modelling is already converged irrespective of length but in the finite and tethered case, the (18,0) tube seems to show a much larger deviation than the (10,10).

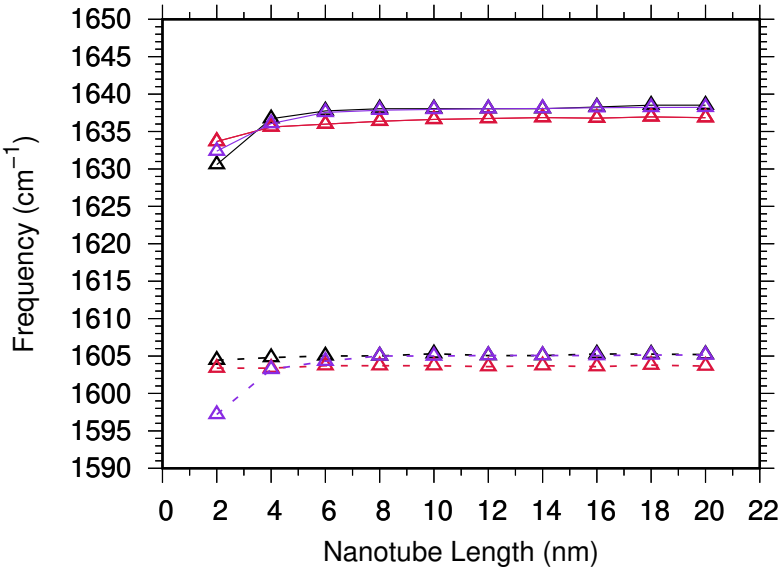


Figure 4.1: A plot of the variation of the G-band frequency of a (10,10) carbon nanotube with length. The three modelling approximations are shown: finite (black), periodic (crimson) and tethered (violet). The G^+ (TO) bands are in solid line and G^- (LO) are in dashed lines.

When comparing the converged values of the G^+ and G^- (or the splitting between the two) we see in all three case it converges to the same value for both the (10,10) and (18,0) tubes. Furthermore, at 5 nm length, these modes are almost converged, moreover we could say the nanotubes vibrational behaviour which relates to in-plane motions is converged across all methods. The G^+ (LO) in the (10,10) tube and the G^+ (LO) in (18,0) have been shifted by 14 cm^{-1} using the approximate linear relations arising from strain (to be discussed in chapter 5), due to strain in the unit cell.

The G-band mode is common across a wide range of carbon nanomate-

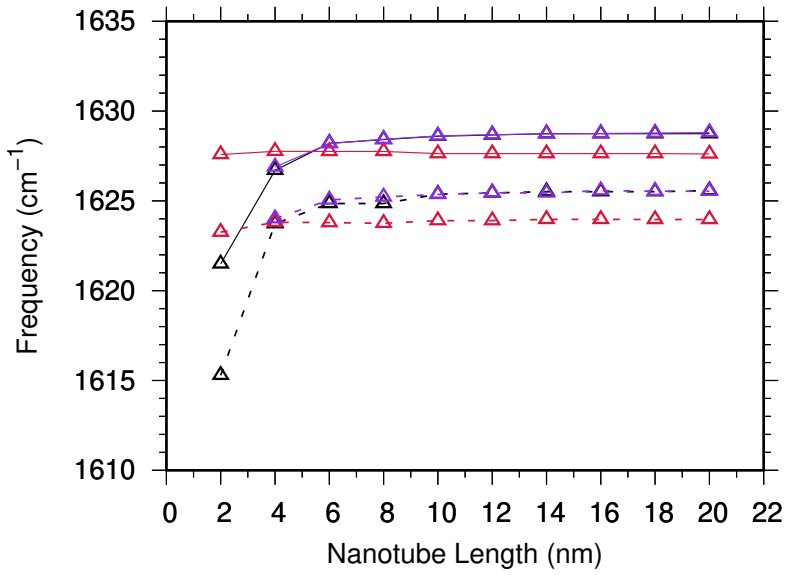


Figure 4.2: A plot of the variation of the G-band frequencies of an (18,0) carbon nanotube with length. The three modelling approximations are shown: finite (black), periodic (crimson) and tethered (violet). The G^+ (LO) bands are in solid line and G^- (TO) are in dashed lines.

rials, hence we should expect its properties to be relatively independent of large-scale structural differences such as that between a carbon nanotube's tubular structure and graphene's planar structure, and more specifically, in this case, the length of the nanotube. Hence quick convergence should be expected since it's a property that mainly derives from the motion of the planar atomic arrangement of hexagons as oppose to the macroscopic tubular structure.

Figures 4.3 and 4.4 show the convergence of the RBM with respect to length. We see in both cases that the RBMs all converge to the same values in all three modelling methods but at a much larger length of 16 nm

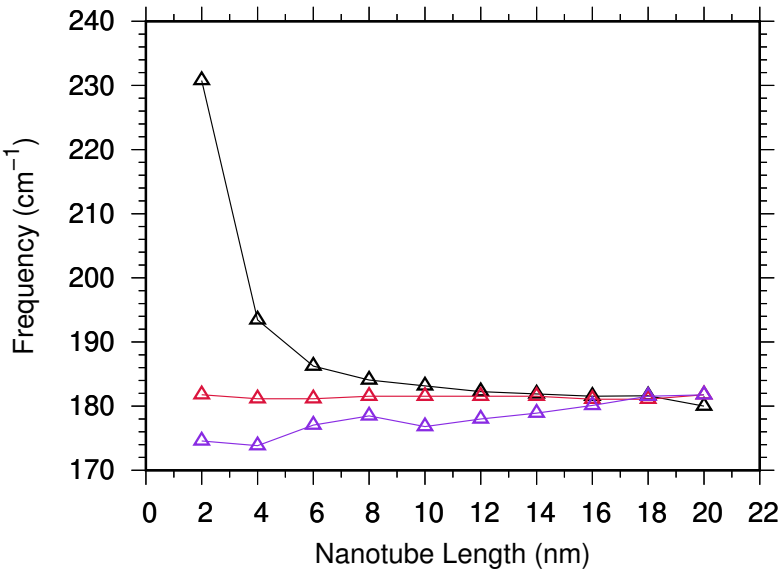


Figure 4.3: A plot of the variation of the RBM frequency with the length of a (10,10) carbon nanotube. The three modelling approximations are shown: finite (black), periodic (crimson) and tethered (violet).

compared to the G-band. In comparison to the G-bands, the RBM requires much longer lengths to converge especially in the finite/tethered case compared to the periodic modelling which is converged at 4 nm. This may be due to the cylindrical structure not being prominent at short lengths to form a true carbon nanotube. Using similar (but opposite) arguments used for the G-band, the RBM is not a result of the hexagonal atomic arrangement but rather its tubular structure that results from rolling up the 1-D graphene lattice. Consequently, this could suggest that simulations utilising short length carbon nanotubes simply are not representative of its true structure. Primarily, this is because its main dynamical features are not fully represented, unless one is interested in in-plane features which arise from the hexagonal lattice that forms a carbon nanotube.

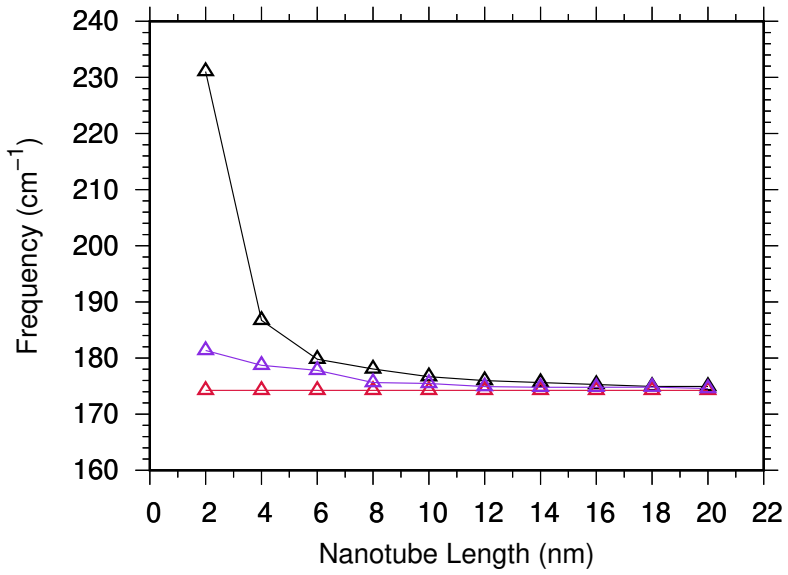
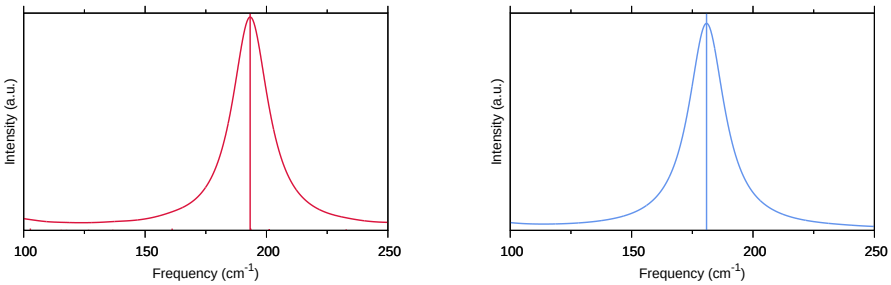


Figure 4.4: A plot of the variation of the RBM frequency with the length of an (18,0) carbon nanotube. The three modelling approximations are shown: finite (black), periodic (crimson) and tethered (violet).

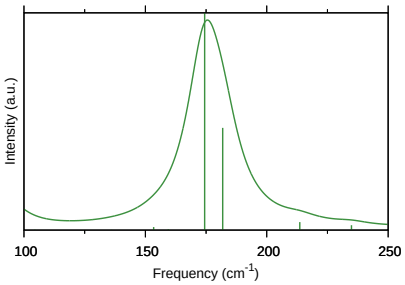
Interestingly, if we look closely at the Raman spectra of the RBM bands of the (10,10) carbon nanotube shown in figure 4.5, we see that for both the periodic and finite cases, we observe a single RBM band as expected. However, in the case of the tethered tube, there is a splitting of this mode. If we look at the RBM normal modes shown in figure 4.6 from each of the different modelling scenarios we see that they are similar in that they are all almost purely radial but also have subtle differences.

In the case of periodic modelling, the normal mode vectors for the RBM are purely radial with no axial components. This is a result of the tube being an infinitely long cylinder with same radii entirely along its structure



(a) Finite

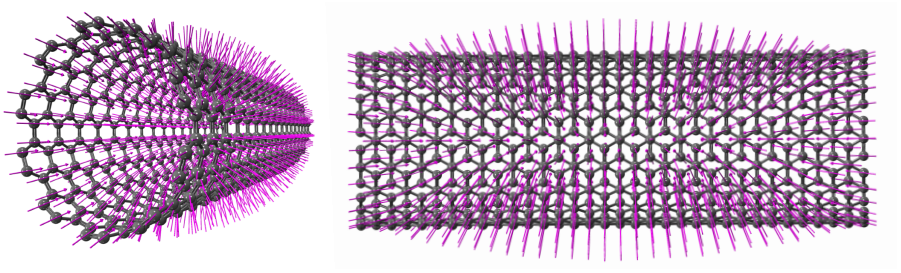
(b) Periodic



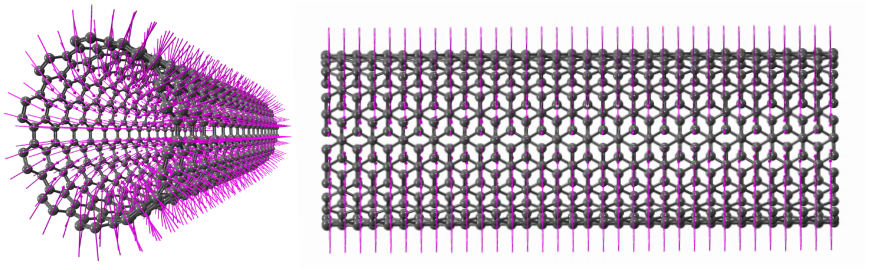
(c) Tethered

Figure 4.5: Raman spectrum of RBM region of a (10,10) carbon nanotube using different modelling methods.

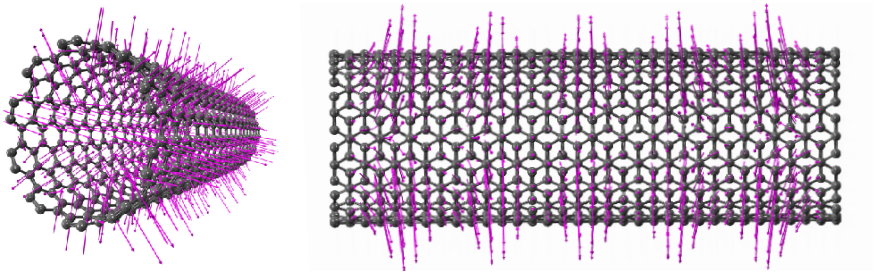
due to the absence of edges. In the case of a finite tube, the RBM still has predominantly radial components but now also small axial contributions which are centred exactly halfway along the carbon nanotube, introducing a small amount of disorder. This can be argued in similar (but opposite) manner to the periodic case where the tube no longer has a perfectly uniform force at every length. This is due to the presence of edges resulting in the tube's diameters also increasing to towards the open ends gradually as shown in figure 4.7. In the case of tethered edges its clear that the two corresponding modes which make up the RBM band are not true RBMs.



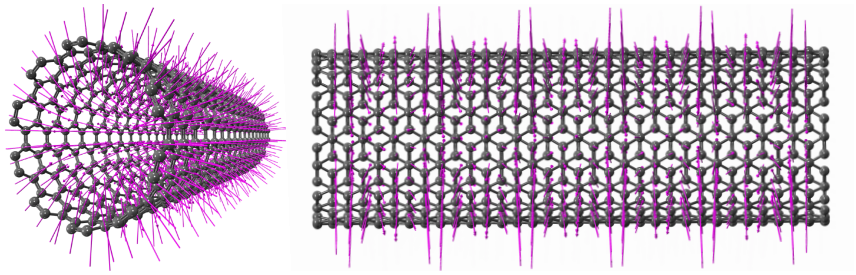
(a) Finite RBM



(b) Periodic RBM



(c) Tethered RBM 1



(d) Tethered RBM 2

Figure 4.6: Vibrational normal modes of the RBM's using different modelling methods.

Experimental studies have measured the Raman spectra of tubes of different lengths and showed no variation in the bands for tubes of length

50 nm, 70 nm and 100 nm tubes. Although these lengths have not been calculated, the calculations presented are converged at 15 nm fitting in line with experimental observations.[125]

Normal mode analysis is often used as an indicator of the overall dynamics of a system, and based on the previous analysis it's clear that the dynamics observed for the three previous RBMs are very different. This shows that such approximations can significantly perturb the way a nanotube moves. It is therefore important that these considerations are made especially for molecular dynamics simulations since the different models could lead to different results.

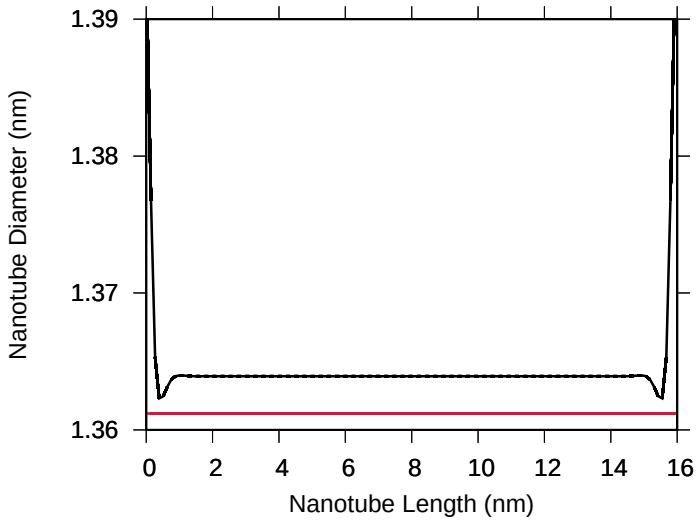


Figure 4.7: A plot of the variation of 16 nm (10,10) carbon nanotubes diameter with length with finite (black) and periodic (red) modelling.

Next, we examine the effect of the different modelling strategies on the vibrational density of states. Figure 4.8 compares the VDOS of a 20 nm

carbon nanotubes using all three modelling methods. It's clear that they all match with the VDOS for periodic calculation being slightly shifted this is likely be a result of a small amount of strain in the unit cell. This convergence is beneficial since it indicates that information such as thermodynamic properties which derive from vibrational behaviour will be independent of the modelling method used.

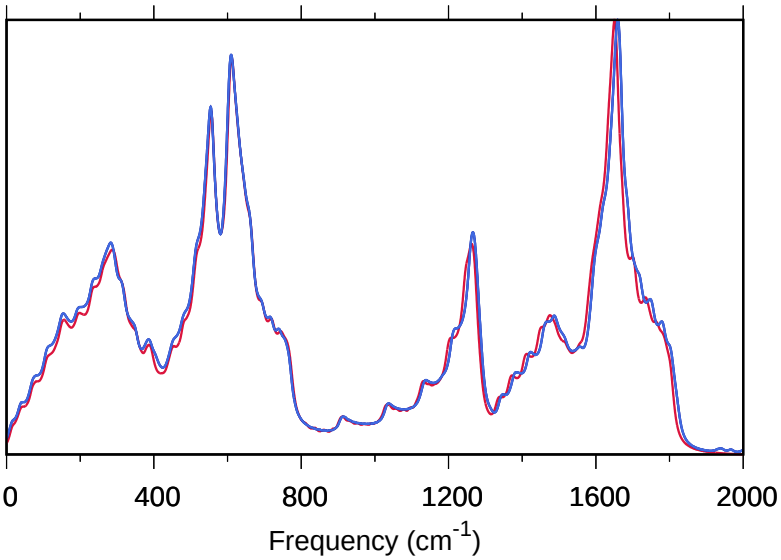


Figure 4.8: The computed VDOS of a 20 nm (10,10) carbon nanotube with periodic (red) and finite (blue).

Figure 4.9 and 4.10 shows the change in the VDOS with respect to length up to 20 nm for a finite and periodic tube. We see that the VDOS is converged at approximately 10 nm and 6 nm, for finite and periodic modelling, respectively. This value for finite is different to the case of the G-band at 6 nm and RBM at 16 nm. Although the VDOS gives an idea of the overall set of modes, it's clear that it can be slightly misleading as

to whether all vibrational properties are converged since finer details are clearly overlooked.

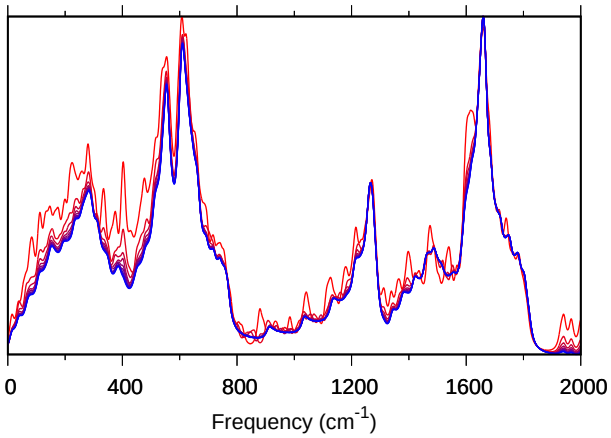


Figure 4.9: The computed VDOS of a (10,10) carbon nanotube with finite modelling with increasing length of nanotube from red to blue.

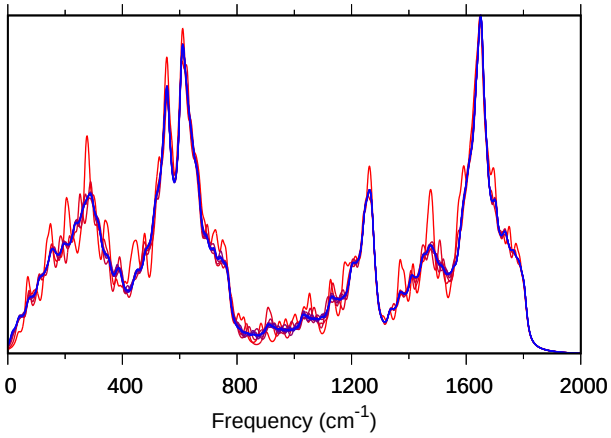


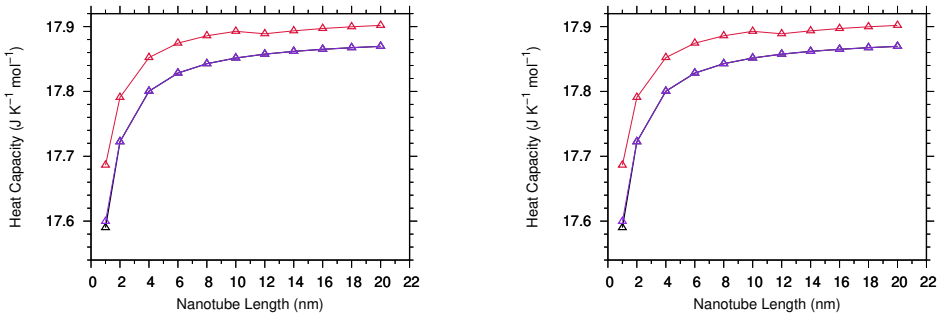
Figure 4.10: The computed VDOS of a (10,10) carbon nanotube with periodic modelling with increasing length of nanotube from red to blue.

Figures 4.11 to 4.12 show heat capacities computed using different

length nanotubes calculated using the different modelling methods at 100K and 200K. Using heat capacities can give a better indication of convergence in the VDOS since it represents the entire sets of modes in a single value. The heat capacities, C_v (constant volume) are calculated using the following formula as used in previous studies of carbon nanotube heat capacity.[126]

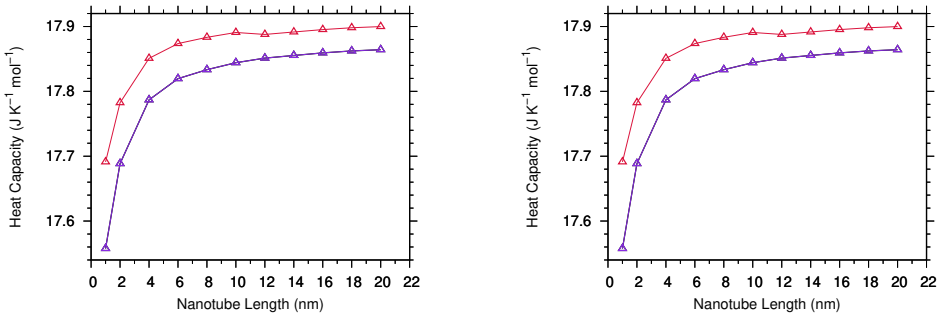
$$C_v = \sum_{i=1}^{3N-4} \left(\frac{\hbar\omega_i}{k_b T}\right)^2 \frac{\exp(\hbar\omega_i/k_b T)}{[\exp(\hbar\omega_i/k_b T) - 1]^2} \tag{4.1}$$

Where $\hbar$ is the reduced Plancks constant, k_b is the Boltzmann constant, T is temperature and ω is the frequency of mode, i. In both cases of a (10,10) and (18,0) carbon nanotube, we see that the heat capacities are almost converged at approximately 16 nm similar to the RBM frequency.



(a) 100 K (b) 200 K

Figure 4.11: A plot of the variation of the heat capacity of a (10,10) carbon nanotube with length at 100 K and 200 K. The three modelling approximations are shown: finite (black), periodic (crimson) and tethered (violet).



(a) 100 K (b) 200 K

Figure 4.12: A plot of the variation of the heat capacity of a (18,0) carbon nanotube with length at 100 K and 200 K. The three modelling approximations are shown: finite (black), periodic (crimson) and tethered (violet).

4.3 Graphene

Graphene like nanotubes can be expected to exhibit variation in properties depending on the modelling method used. Figure 4.13 is a comparison of the Raman spectra of graphene modelled using finite, periodic and tethering methods.

The most significant difference is seen for the finite model of graphene. Here we see a progression of bands which correspond to intra-layer breathing modes (ILBs), the first 2 bands centred at 98.00 cm^{-1} and 234.50 cm^{-1} of the progression correspond to breathing modes with a node in the centre of the graphene sheet (examples are shown in figures 4.14a and 4.14b). The rest of the bands upward from this progression correspond to in-plane modes of increasingly higher sequential orders with nodal planes. This part of the progression is made of modes which go along the bond axis and those

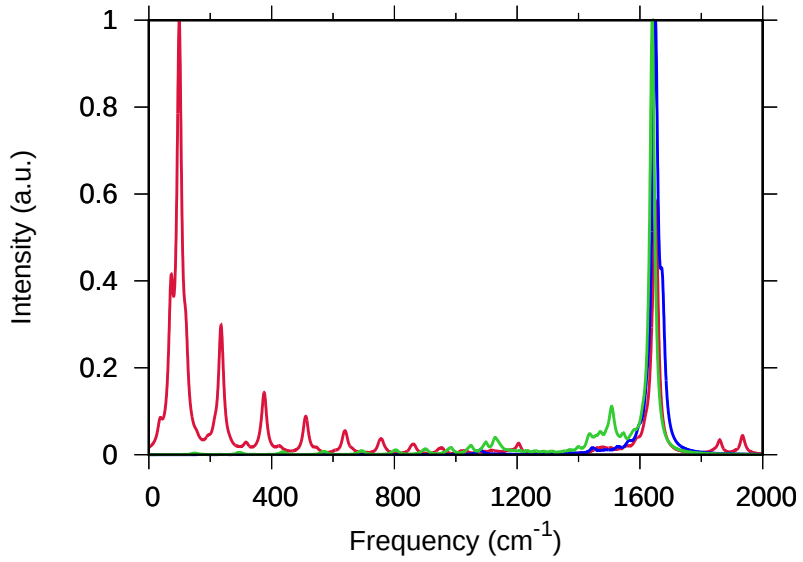
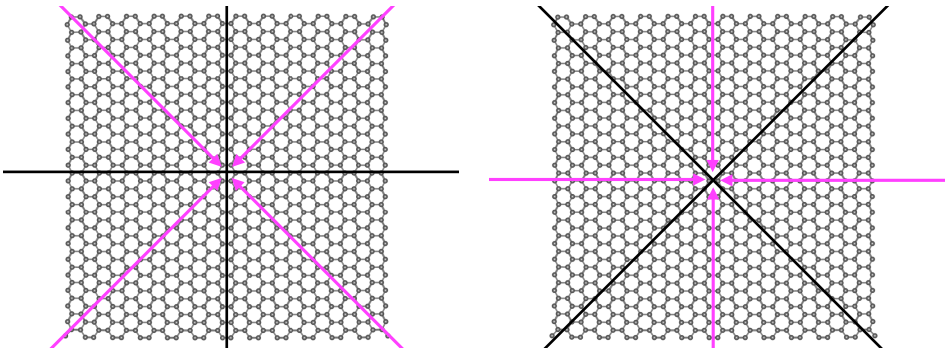


Figure 4.13: A comparison of computed Raman spectra of graphene using finite (red), tethered (blue) and periodic (green) models.

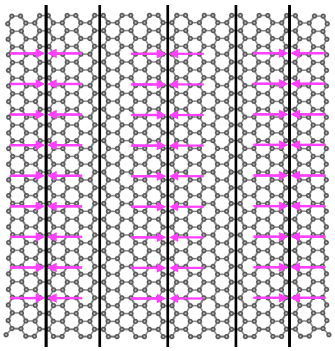
which go against the bond axis (examples shown in figures 4.14c, 4.14d and 4.14e). The higher energy bands correspond to those along the bond axis, and this can be rationalised since stretching co-ordinates are higher in energy than bending modes. This is similar to the case of the splitting of the G-band of carbon nanotubes but has led to significantly smaller splitting in this case of 8 cm^{-1}.

This progression is not seen experimentally and this can be explained when we consider how Raman measurements of graphene are normally made. Usually in experimental measurements, graphene samples are on some form of substrate, usually supported on a silicon surface or samples are "free standing" but are mounted on top of meshed gold grids such that the sides are actually tethered down. Consequently, within the exper-

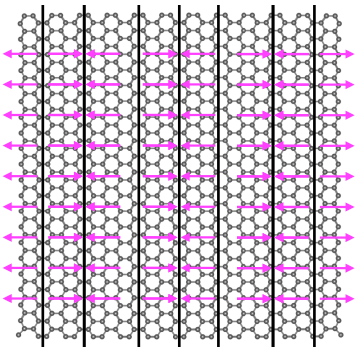


(a) ILB1 (72.16 cm^{-1})

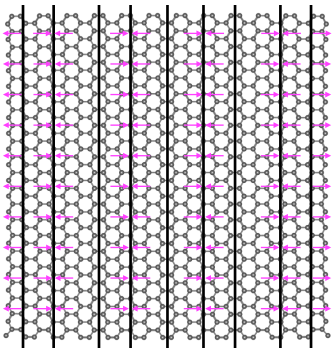
(b) ILB2 (99.90 cm^{-1})



(c) 3 nodes (377.54 cm^{-1})



(d) 4 nodes (513.87 cm^{-1})



(e) 5 nodes (635.90 cm^{-1})

Figure 4.14: Raman spectrum of RBM region of (10,10) using different modelling methods.

imental frame, the area of the Raman laser would be dominated by signals without edges and also are under the influence of them being tethered down. This could likely lead to the complete dampening of such modes. This is more accurately described by periodic or tethered models.

In chapter 3.3.7, we examined the effect of a Stone-Wales defect on graphene in its Raman spectra and structure, here we re-visit this and look at the resultant effects of modelling method on the structure. The calculated Raman spectra showed similar differences to those for pristine graphene sheets. In the case of a finite structure of graphene with a Stone-Wales defect, the entire system is able to relax and "ripple" as far as it needs to fully relax down to its minimum structure. However when we compare to the case of a periodic structure, a different picture emerges where neighbouring unit cells begin to interact. This is not a result of the range of the potential, but rather the induced ripples from the Stone-Wales defect do not relax fully before the next unit cell. Thus artificial strain is induced in the structure. Although the RMSD of the periodic unit with the finite flake is 0.719 Å, the consequence is best shown when considering the longer range affect of the rippling of the periodic cell as shown in figure 4.15. The induced ripples (z-direction) cause channels to form in the structure since they are not fully relaxed.

However, although we observed this affect structurally, the frequency of the Stone-Wales C-C stretching mode remains the same at 1922 cm^{-1}, showing its insensitivity to it's wider rippling. Several calculations in the literature, utilise small units cells when modelling defects like the Stone-Wales defect, as such non-physical stresses can be induced as a result which could cause perturbed results.

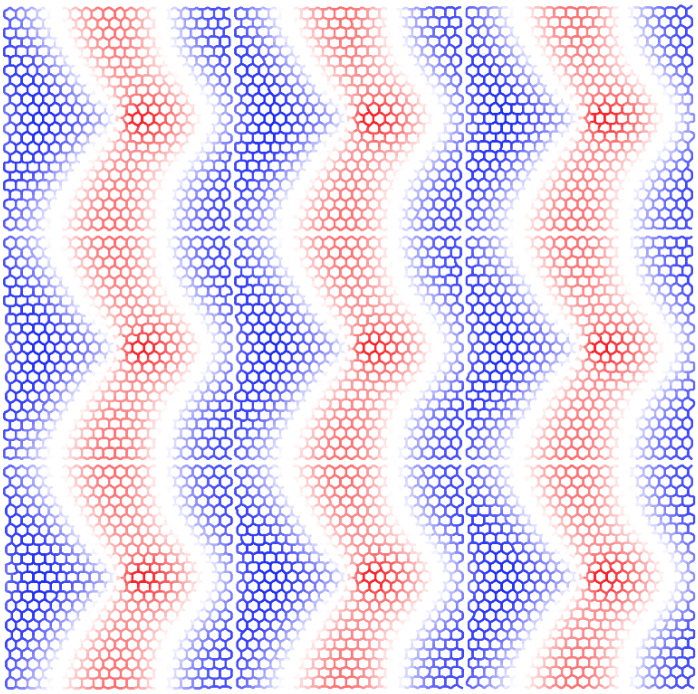


Figure 4.15: A plot of 5 nm x 5 nm graphene unit cell (centre), with repeating units in the 2-D directions, each atom is coloured by the magnitude of its z vector (out of plane) component, positive regions are in blue and negative are in red.

4.4 Conclusion

In this chapter we examined three different modelling scenarios for simulating the vibrational spectroscopy of carbon nanotubes and graphene. Each scenario can result in different structure, normal modes and Raman spectra for both graphene and nanotubes. It was shown that finite modelling at a large enough system size, the frequencies converge to the values of the periodic calculations. However, in the case of finite simulation, it is clear that the presence of edges can influence different bands in Raman spectra and their normal modes. In particular, the rate of convergence for frequencies is dependent on the particular vibrational mode of interest, and

that some of these modes although corresponding to the same band, can look very different depending on the method used. Therefore the size of system should undergo careful consideration depending on the property of interest.

Chapter 5

Strained Nanotubes

In this chapter, we apply MM^{Vib} to study the response of vibrational properties of carbon nanotubes under the influence of uniaxial strain. The dependence on armchair vs zig-zag, diameter and chirality are studied, and no significant differences are found between any of these different types of nanotubes in the shift rates of the Raman active LO band. This is contrary to experimental observations. Further examination of vibrational modes and VDOS show that modes with normal mode vectors along the tube axis in the direction of the applied strain have their frequencies shifted under strain whilst those with normal modes that are perpendicular to the tube axis such as the RBM, remain unchanged.

5.1 Introduction

Raman spectroscopy of carbon nanotubes under strain[127–129] has attracted much attention during the past several years. The Raman response including the shifts in the bands and change in intensities can provide information on the geometric and electronic structure of strained carbon nanotubes,[130]

which has important implications for the application of nanotubes to sensing applications like nano-electromechanical systems (NEMS). Hence understanding their underlying properties and potential for device application is of considerable value. Investigation of the Raman response of different vibrational modes to strain via theoretical methods allows us to explore the physical origin and dependence on tube geometry. Most importantly, the changes observed in Raman spectra from the strain dependence of the molecule to any macroscopic deformation can reveal what the deformation is doing to a material at a molecular level.

In atomic force microscopy (AFM) it is challenging to control the deformation of nanotubes under different forms of strain (such as torsion), as such it has been only been applied in a limited way. Furthermore, the possible types deformations of the nanotubes from AFM manipulation include tube bending, buckling or radial squashing under the AFM tip. To complicate matters further, the use of bundles (or ensembles) which are made up from a distribution of chiralities and diameters often leads to difficulty in characterising the intrinsic behaviour of Raman modes under strain.[131] For example, the expected different responses to strain of different high-energy tangential modes (G-band) or low-frequency modes, which correspond to distinct atomic displacement patterns from different nanotube structures. The main results in the literature generally find that in single-wall nanotubes, the RBM and G-band spectra respond differently to the various forms of strain listed above.

Work by Kong *et al.*,[131] has shown that for nanotubes under uniaxial

strain, the RBM and TO do not have a noticeable response but the other observed LO frequencies are downshifted with the resulting changes in electronic structure being reflected in the Raman intensity changes. However, limitations which affected these measurements were noted, such as deformations of the nanotubes from the AFM manipulation include tube bending, buckling or radial squashing under the AFM tip as well as possible radial compression caused by AFM tip dragging and pressing on the SWNT in addition to the uniaxial strain, as well as substrate interaction. Furthermore, alternative methods by Gao[132] employed crude estimation of relating uniaxial strain and G-band frequency shift rates via nanotubes tethered down by metal electrodes. Although a wide spread of tube structures were studied with respect to the diameters and chiral angle, the dependence of the shift rates are unclear. The results from this study are contrary to that of ab initio calculations and other experiments, this may be a result of different experimental strategies employed and difficulty in applying strain in a controlled manner.

Ab initio studies of uniaxial strain on a variety of nanotubes by Dong *et al.*,[77] found 4 key results:

- The frequencies of the low-frequency Raman active modes almost do not change, while the high-frequency part of the Raman spectra is shifted downward, and was found to be consistent with the available experimental and theoretical results.[133–135]
- The deformation does not change the number of the Raman-active vibrations.
- The rate at which the Raman modes shift is linear and almost the

same for the nanotubes with different radii.

- For any nanotube, those modes with large tangential atomic displacements parallel to the tube axis show largest shifts than tangential with atomic displacements perpendicular to the tube axis (these will have a small elongation/compression upon strain application).

The work here follows the same theoretical procedure for strain simulation as Dong *et al.*[77] Where strain is applied by gradually shrinking and extending unit cell size in the directions of the carbon nanotubes axis, then the carbon nanotube geometries structures are fully optimised before performing further frequency analysis and Raman simulation.

The use of MM^{Vib} enables us to look at specific modes directly for specific single nanotubes free from practical issues and make comparisons between different nanotube types. We can also use this to examine the applicability of the potential in non-equilibrium scenarios. Henceforth in this work, we study the effects of uniaxial strain (shown in figure 5.1) in carbon nanotube systems to rationalise and find links between its structure and vibrational properties. Firstly we compare its effects and relationships

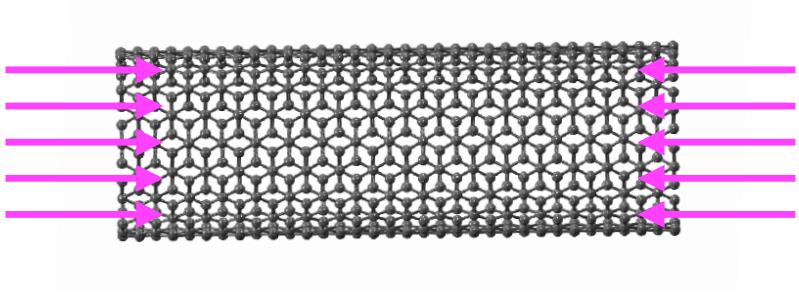


Figure 5.1: A diagram showing the application of uniaxial strain on a carbon nanotube.

with radii and compare zig-zag and armchair nanotubes. Secondly, we look at the dependence of chirality on strain effects, and lastly its effects on the VDOS.

5.2 Zig-Zag and Armchair Nanotubes

Firstly we compare the application of the strain to a non-chiral armchair and zig-zag carbon nanotube. In figures 5.2 and 5.3 the variation of the G-bands and the RBMs of a (10,10) and (18,0) are shown, these are two carbon nanotubes of similar diameter (similar RBMs as well).

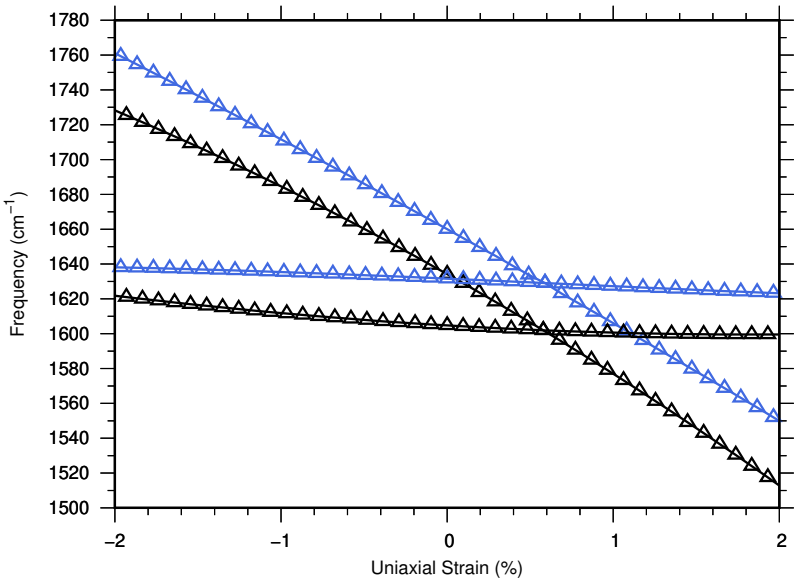


Figure 5.2: A plot of the variation of the G-band frequencies of a (10,10) (black) and (18,0) (blue) carbon nanotube with the application of uniaxial strain.

Positive strain corresponds to stretching of the unit cell and negative to

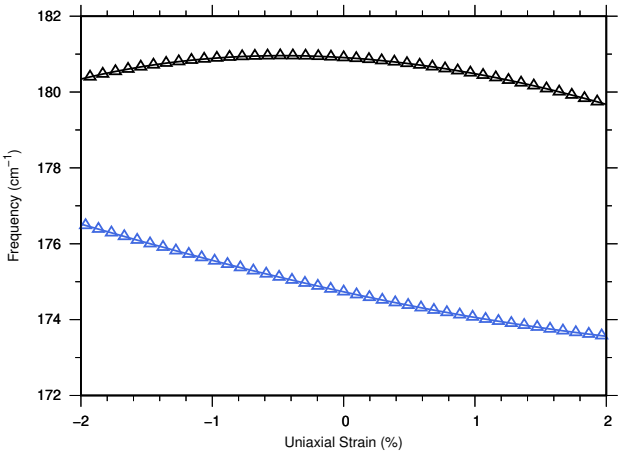


Figure 5.3: A plot of the variation of the RBM frequencies of a (10,10) (black) and (18,0) (blue) carbon nanotube with the application of uniaxial strain.

compression of the unit cell. Focusing on the RBM (figure 5.3), we see no significant variations of this mode with the application of strain and no new modes become Raman active. This is in agreement with experiment since there are no changes of symmetry to the structure. Furthermore, vibrational modes like the RBM which do not have vector contributions along the bond axis parallel to the applied uniaxial strain are unaffected and remain at the same frequency. In contrast, the G-band component with the tangential modes parallel to the nanotube axis, LO, varies significantly in both cases with strain showing both positive and negative shifts in frequency (figure 5.2), consistent with experimental observation. This is rationalised by the fact that the normal modes lie in the direction of the applied strain, and that the compression or extension of bonds leads to large changes in the force constants and frequencies. The G-band component in both cases with the tangential modes perpendicular to the nanotube axis,

TO, show little change or dependence. The shift rate of the G-band, *LO* with strain for the (10,10) armchair is 53.83 $cm^{-1}\%^{-1}$ and zig-zag (18,0) $52.77^{-1}\%^{-1}$ which are very similar considering the differences in the structure of the two systems.

Next, we take a look at the effect of radii on the strain response on carbon nanotubes. Figures 5.4 and 5.5 shows the variation of the G-band, *LO* mode, with uniaxial strain of different diameter nanotubes. Here we see no significant change in the shift rate between any of the tubes regardless of being armchair or zig-zag with a change in diameter.

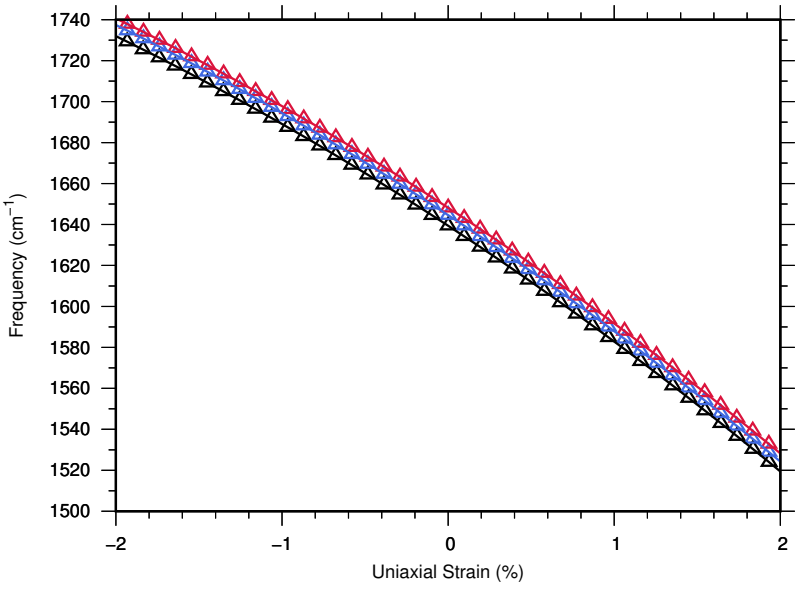


Figure 5.4: A plot of the variation of the G-band, *LO*, with the application of uniaxial strain of three armchair nanotubes of increasing diameter, (10,10) (crimson), (15,15) (blue) and (20,20) (black).

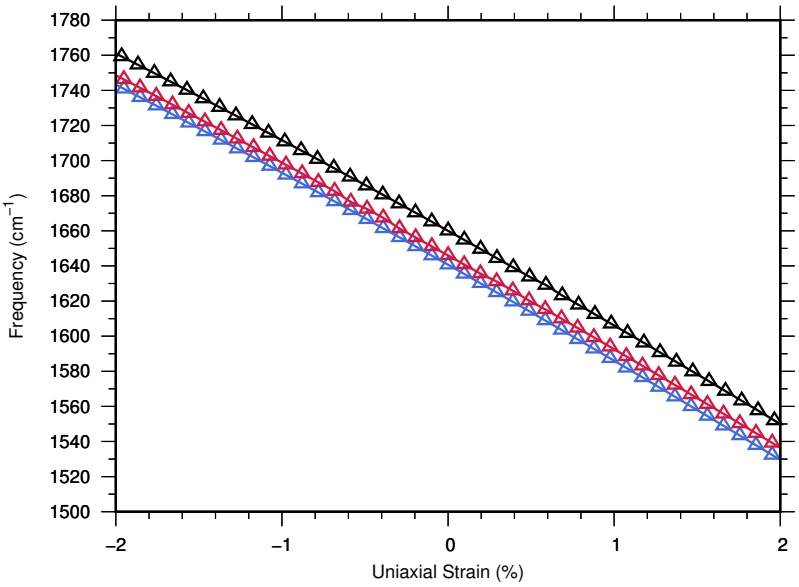


Figure 5.5: A plot of the variation of the G-band, *LO*, with application of uniaxial strain of three armchair nanotubes of increasing diameter, (18,0) (crimson), (27,0) (blue) and (36,0) (black).

5.3 Chirality

Another factor that could affect the response of uniaxial strain is the chirality of the carbon nanotube. Here we examine the strain response when varying the chiral angles whilst keeping nanotube radii's similar. Chiral nanotubes are particularly challenging calculations for electronic structure methods due to the unit cell containing very large numbers of atoms compared to its non-chiral counter-parts. Similar to non-chiral tubes, the G-band mode parallel to the carbon nanotube axis is most sensitive to strain. The results for the variation in the G-band, *LO*, frequency shift rate for varying chiral angles of the tubes are shown in table 5.1. Nanotubes of similar radii have been chosen. The results show that there is no significant

Table 5.1: Variation of *LO* mode frequency shift rates of 7 nanotubes with chirality.

Indices	Chiral angle(°)	*LO* ($cm^{-1}\%^{-1}$)
(17,0)	0.00°	54.63
(16,2)	5.88°	54.63
(15,4)	11.52°	53.74
(14,5)	14.70°	N/A
(13,7)	20.17°	53.49
(11,9)	26.69°	53.13
(10,10)	30.00°	53.49

dependence on the chiral angle. This is in contrast to experiment where large variations are seen for different chiralities.[132] This may be due to electronic structure effects, which are neglected by empirical models. The variation in the shift rates may possibly be a result of the strain inducing large-scale changes in the electronic structure, hence changing bonding modes especially considering that experimentally values vary between 0 and 30 $cm^{-1}\%^{-1}$. Moreover, different chirality tubes may lead to different elongations of bonds in experiments hence will affect the frequencies. The subtle differences of these elongations may not be captured by MM^{Vib} and be a result of changes in hybridisation state.

Within the literature, it has been noted that the intensity of the RBM was found to be very sensitive to strain for metallic carbon nanotubes in contrast to that of the semiconducting nanotubes, whose RBMs were not observed to change at all with strain.[128] Furthermore, none showed

a change in the relative intensity of the G-bands. Although not shown, metallic tubes showed no appreciative change in intensity during the application of strain, whereas semiconducting tubes did show variations, however, the changes of intensity showed no clear pattern or link with the application of strain. Within experimental measurements, normally resonant enhancement (coupled electronic and vibrational Raman transition) is used to amplify signals, which is often chosen to enhance the RBM signal hence experimentally these intensity differences may be exaggerated and not seen here within a non-resonant framework.

5.4 Vibrational Density of States

If we examine changes in the VDOS with the application of strain, we see two distinct regions become apparent as shown in figures 5.6 and 5.7. In both cases for (10,10) and (18,0) nanotubes below 1000 cm^{-1}, there is a region of modes which are generally insensitive to the application strain both negative and positive. In contrast, above 1200 cm^{-1} we see a larger portion of vibrational modes are significantly perturbed upon strain. Based on the previous analysis of the RBM and G-band, in particular, the LO mode, which was vibrating along the direction of the strain, a similar rationale for the effect can be made. Whereby vibrational modes which have a significant contribution of its vector against the direction of the applied strain are shifted more than those that are not. This can indicate a possible method of mechanical control of the vibrational modes and hence properties like heat capacity.

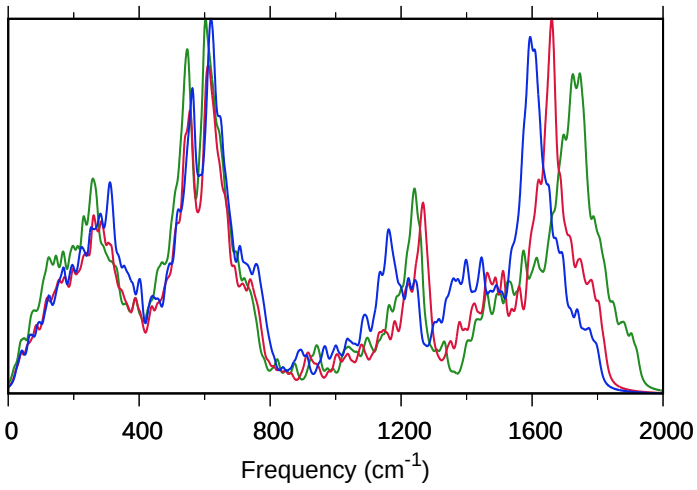


Figure 5.6: A plot of the variation of the VDOS with the application of uniaxial strain of a (10,10) armchair nanotubes with 0 % strain (red), -2% strain (green) and +2% strain (blue).

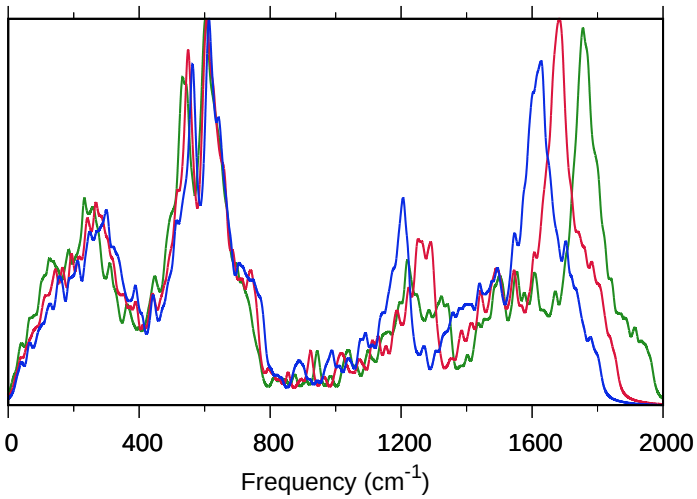


Figure 5.7: A plot of the variation of the VDOS with the application of uniaxial strain of a (18,0) armchair nanotubes with 0 % strain (red), -2% strain (green) and +2% strain (blue).

5.5 Conclusions

The effect of uniaxial strain on the vibrational spectroscopy of carbon nanotubes has been investigated. We find that as found in previous theoretical work, the *LO* mode is sensitive to the uniaxial strain and shifts linearly in response.[77] MM^{Vib} showed no significant differences to the rate of change of the *LO* (or intensities) in response to the applied strain in different diameter and chirality nanotubes as found in previous theoretical work. It is difficult to make an exact comparison of the results here with experiment due to the large spread of results and methodologies in the literature but the comparison of findings with ab initio data shows that MM^{Vib} is performing well.

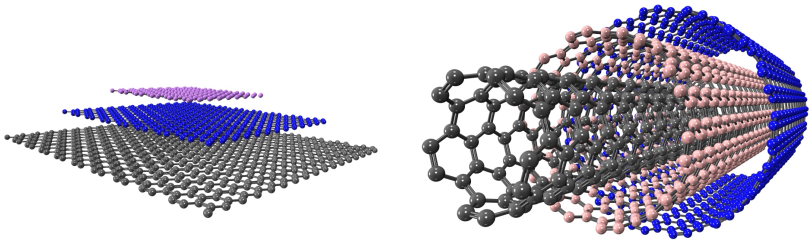
Chapter 6

Modelling of Multi-Layer Carbon Nanomaterials

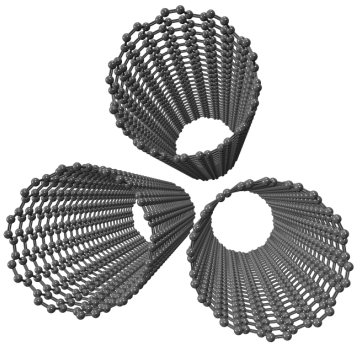
So far in this thesis, studies have focused on single-layer/walled forms of carbon nanomaterials and will be referred to as single layer graphene (SLG) and single wall carbon nanotubes (SWNTs) from this point onwards. Here we will extend the Murrell-Mottram potential to enable the capability for it to model the vibrational spectroscopy of few-layer graphene (FLG) and multi-wall carbon nanotubes (MWCNTs), and further multi-layer systems such as bundles and graphitic nanofibres. Using this capability we study the vibrational spectroscopy of the aforementioned multi-layered carbon nanomaterials with focus on Van der Waals based vibrational modes.

6.1 Introduction

Multi-layer carbon nanomaterials are of considerable interest with numerous studies found in the literature spanning MWCNT's made up of multiple concentric single walled nanotubes inside one another,[136–138] nanotube



(a) Few-layer graphene (b) Multi-Wall carbon nanotube



(c) Carbon nanotube bundle

Figure 6.1: Representative structures of some multi-layer carbon nanomaterials.

bundles which are made up of collections of nanotubes held together by dispersion[139–141] and also FLG made up of Bi-, Tri-,... layers of graphene sheets. The high interest in these multi-layer systems comes from the unique electrical, mechanical and optical properties they exhibit compared to their single layer analogues with lower aspect ratios (length/diameter) as well as in some cases bypassing the limitations in processing and assembly of single layer systems.[10]

Here we extend the MM^{Vib} potential to include dispersion interaction to model these multi-layer carbon nanomaterials. We focus on the mod-

elling of vibrational frequencies and properties derived from the multi-layer structure hence the interlayer Van der Waals vibrational modes. Using this new dispersion interaction we derive parameters by fitting to experimental data via a random search. The resultant potential is then applied to model the vibrational spectroscopy of MWCNTs, FLGs, carbon nanotube bundles illustrated in figure 6.1 and further exotic structures.

6.2 Modelling Dispersion Interaction

In order to model multi-layer materials, we need to account for dispersion interaction within the MM^{Vib} potential, which has not been considered previously. Dispersion interactions are the main driving force and dominant interaction for the formation of a MWCNT via encapsulation and the interaction between layers of graphite.

The most common function form for modelling dispersion interaction in a simulation is the well known 6-12 Lennard-Jones potential,[142]

$$V_{LJ} = 4\epsilon\Big[\Big(\frac{\sigma}{r}\Big)^{12} - \Big(\frac{\sigma}{r}\Big)^{6}\Big] \tag{6.1}$$

where, r, is the distance between particles, ϵ is the depth of the potential well, σ is the collision diameter; the finite distance where the inter-atomic potential is zero.

In this study, we use the function form of Grimme *et al.*[143] This function form is most often employed as a dispersion correction in DFT calculations. The form of this potential provides a convenient way to extend the MM^{Vib} potential due to its mathematical simplicity and intuitive form for practical

implementation and speed in codes.

Utilising this function form for modelling dispersion interactions, the total energy, E, using the potential is now modelled as,[143]

$$E = \sum_{i}^{N} \sum_{j=i+1}^{N} V_{ij}^{(2)} + \sum_{i}^{N} \sum_{j=i+1}^{N} \sum_{k=j+1}^{N} V_{ijk}^{(3)} + \sum_{i}^{N} \sum_{j=i+1}^{N} V_{ij}^{(Disp)} \tag{6.2}$$

where $V_{ij}^{(2)}$ and $V_{ij}^{(3)}$ are the two body and three body contributions from the Murrell-Mottram potential and $V_{ij}^{(Disp)}$ is the dispersion interaction. $V_{ij}^{(Disp)}$ takes the following form:

$$V_{ij}^{(Disp)} = -s_6 \sum_{i}^{N-1} \sum_{j=i+1}^{N} \frac{C_6^{ij}}{R_{ij}^6} f_{dmp}(R_{ij}) \tag{6.3}$$

Here, N is the number of atoms in the system, C_6^{ij} is the dispersion coefficient for atom pair ij, s_6 is a global scaling factor to account for the different behaviour of the intermolecular potential especially at intermediate distances, α is a damping parameter and R_{ij} is the inter-atomic distance between atoms ij. $f_{dmp}(R_{ij})$ takes the form,

$$f_{dmp}(R_{ij}) = \frac{1}{1 + e^{-\alpha(R_{ij}/R_0 - 1)}} \tag{6.4}$$

where R_0 is the sum of atomic Van der Waals radii. This function is chosen because it decays at small R fast enough to zero such that the dispersion corrections between atoms well below typical Van der Waals distances are negligible and thus covalent bonds are being modelled by the MM^{Vib} part are not significantly affected by the correction.

The $V_{ij}^{(Disp)}$ term should ideally have the correct R^{-6} behaviour up to typical Van der Waals distances between carbon atoms (about 3.3 - 3.4 Å in graphite). It should also have significant interactions in regions down to

about 2.7 - 2.8 Å where the overlap of the electron densities would be small, while there is a negligible contribution for distances below 2.5 Å where the Murrell-Mottram potential will start to account for chemical bonding between carbon atoms.

It is important to note that $V_{ij}^{(Disp)}$ is a model-dependent quantity with no real physical meaning, the atomic C_6^{ij} coefficients are scaled by the factor s_6 to account for the different behaviour of the intermolecular potential especially at intermediate distances, whereas previously mentioned the Murrell-Mottram chemical bonding becomes dominant.

The existing BPM used in chapter 3 was only applicable to covalent bonds and with the addition of dispersion this model needs to be modified to account for Van der Waals type bonding. In this section, the focus is to analyse the particular set of interlayer modes which result from this type of bonding and so we use the same method of SuYing *et al.*[144] In this approach Van der Waals interactions are treated as weak covalent bonds between layers and that the BPM now becomes a sum over all interlayer bonds as opposed to intralayer bonds. With this separate treatment, it allows the Raman spectrum to be decomposed to analyse purely Van der Waals interlayer modes and covalent modes. Here we employ the same set of parameters used previously since the focus of this work is on whether these modes are Raman active and their trends. We also utilise polarisation dependencies to assist in the identification of shear modes, such as XY polarisation configuration to enhance modes in the xy plane such as the shear modes in FLG in section 6.4.

6.3 Development of Dispersion Parameters, Random Search Parametrisation

Before considering how to develop parameters for this dispersion interaction, we must consider the previous development of MM^{Vib}. Here we did a random search fitting the data to the Hessian of C_{60} from DFT with the B3LYP exchange-correlation functional. It is important to note that this DFT data lacked a significant dispersion component and hence dispersion interactions were not accounted for in the fitting. As a consequence, the dispersion interactions can be included as an additive term to the original potential. However, obtaining an equivalent Hessian for dispersion data will be difficult due to the computational cost of accurate methods to obtain one. Consequently, we have fitted the dispersion to experimental data of bilayer graphene, and fit the data to the frequency of the doubly degenerate shear mode (31 cm^{-1}) shown in figure 6.3 and the structural interlayer spacing of 3.35 Å.

As with the previous search method we do a random search for parameters. It is important to note that the existing B3LYP parameters were tested for dispersion and found to be unsuitable since a shear frequency of 11.1 cm^{-1} was obtained and an interlayer spacing of 3.16 Å. In the fitting, the parameter C_6 is not varied but values of 1.65 J nm^6 mol^{-1} [143] or 1.75 J nm^6 mol^{-1} [145] were used since these are intrinsic coefficients and two commonly used values in the literature. The parameter, α, was varied between 23 and 28, R_0 between 1.45 and 1.80 Å since this value is related to the Van der Waals radii, the value employed by Grimme at 1.452 Å, for the B3LYP

exchange-correlation functional deviates a lot from the experimental value of 1.70 Å[146] and s_6 was varied between 1 and 3. The goal of this random search was to minimise the error in the frequency of the shear mode and the interlayer spacing of bilayer graphene.

Two sets of parameters denoted MM^{Vib+D1} and MM^{Vib+D2} were found after the search, and are shown table 6.1. With MM^{Vib+D1} an interlayer spacing of 3.33 Å and a shear mode frequency of 35.8 cm^{-1} is obtained and with MM^{Vib+D2} an interlayer spacing of 3.35 Å and a shear mode frequency of 31.0 cm^{-1} is obtained replicating the experimental values. Figure 6.2 shows the new potentials interactions for two carbon atoms, it shows that MM^{Vib+D1} is almost a shift of the existing B3LYP dispersion and that MM^{Vib+D2} is the same but the magnitude of the interaction is lower. Since the focus of this potential is in the modelling of structure and vibrational frequencies, MM^{Vib+D2} is chosen since it better matches experimental data and will be referred to as MM^{Vib+D} from this point onward.

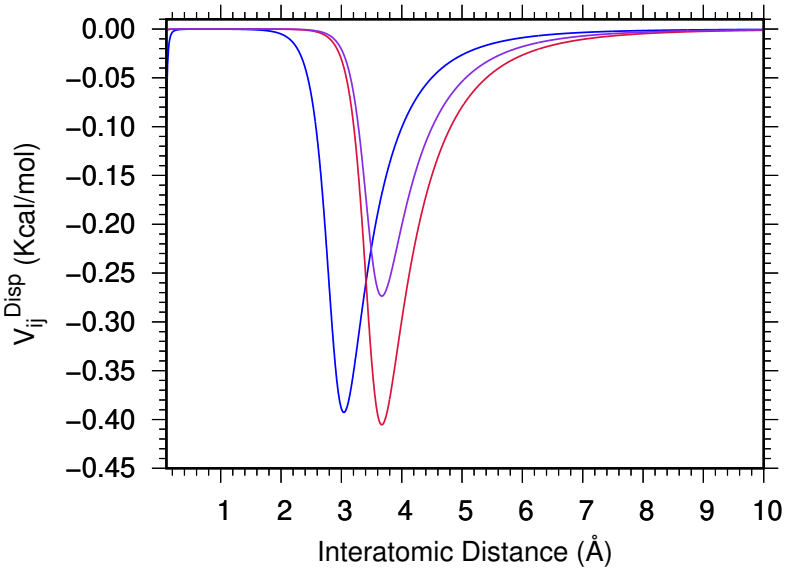


Figure 6.2: A plot of equation 6.3 using Grimme *et al.*'s[145] existing parameters (blue), MM^{Vib+D1} (crimson) and MM^{Vib+D2} (violet) for two carbon atoms.

Table 6.1: Dispersion parameters for B3LYP by Grimme et al.[145] and MM^{Vib} with corresponding shear mode frequency and interlayer spacing (Å)

Parameter	B3LYP	MM^{Vib+D1}	MM^{Vib+D2}
s_6	1.05	3.02	2.06
C_6^{ij} (J nm^6 mol^{-1})	1.75	1.75	1.75
R_0 (Å)	1.452	1.75	1.75
α	23.00	27.72	28.00
Shear frequency (cm^{-1})	11.1	35.8	31.0
Interlayer spacing (Å)	3.16	3.33	3.35

6.4 Few-Layer Graphene

Few-layer graphene is a model system for new emerging 2D layered materials, primarily with each layer thickness leading to unique properties related to its electronic structure[147] and optical activity[148] as well the ability to tune chemical reactivity.[149] Therefore, the characterisation of this class of graphitic material is essential in its study and development of its applications. Raman spectroscopy can provide a direct probe of interlayer interactions and determination of stacking sequence and layer number (N_l), all of which are essential for its characterisation.

The determination of interlayer coupling and the number of graphene layers (N_l) in FLG samples via Raman spectroscopy has been of large interest using a variety of specific vibrational modes. Ferrari *et al.*[150] recently carried out Raman measurement of FLGs from bi-, tri- to 10- layers revealing the Raman active interlayer shear mode which involves the relative motion of adjacent planes of carbon as shown in figure 6.3. The bulk shear

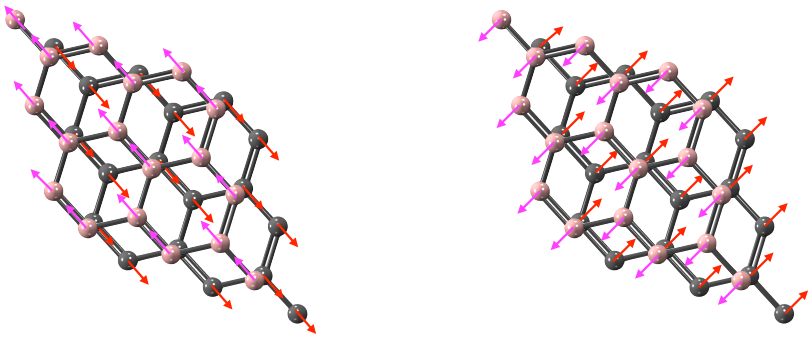


Figure 6.3: The normal mode displacement of the doubly degenerate E_{2g} shear mode (31.0 cm^{-1}) in bilayer graphene.

mode of graphite sits between 43.0 - 44.0 cm^{-1}. It was found in this study that the shearing frequency is linked to the number of layers and addi-

tionally also allows for the measure of interlayer coupling. Heinz *et al.*[151] extended this work to characterised layers (N_l) by utilising the frequencies of the overtones of different interlayer breathing modes up to 20 layers.

The work of Ferrari *et al.* showed that while the G-band of a N_l layered FLG system remained constant the interlayer shear mode between layers of graphene increases according to the following (in cm^{-1}) with layers, N_l,

$$\omega_N = \frac{1}{\sqrt{2}\pi c}\sqrt{\frac{\alpha}{\mu}}\sqrt{1+\cos\left(\frac{\pi}{N}\right)} \tag{6.5}$$

where α is the interlayer coupling strength which was found to be 12.8×10^{18} N m^{-1} , $\mu = 7.6 \times 10^{-27}$ kg $Å^{-2}$ and c is the speed of light cm s^{-1}. In the case of graphite, $N \to \infty$ and $\omega = \frac{1}{\pi c}\sqrt{\frac{\alpha}{\mu}}$. Figure 6.4 shows the relationship of graphene layers N_l with the shear mode frequency computed using MM^{Vib+D} with PBC (unit cell 5 nm by 5 nm) for N_l up to 8 layers and for bulk with the experimental fit. A good match between the theoretical curve and the experimental is found suggesting the potential is performing well. Fitting the theoretical data to equation 6.5 we get an interlayer coupling value of 13.1×10^{18} N m^{-1} in excellent agreement with the experimental value. Furthermore, the G-band was found to be constant with increasing layers.

Figure 6.5 shows the shear modes for 2LG to 5LG and bulk graphite. For a given N_l number of layers there will always be $N_l - 1$ shear modes. These additional shear modes display different displacement patterns and hence frequencies compared to the highest intensity (and frequency) shear mode which produces the relationship shown in figure 6.4. These modes can be either Raman active, IR active or both, however, experiments have

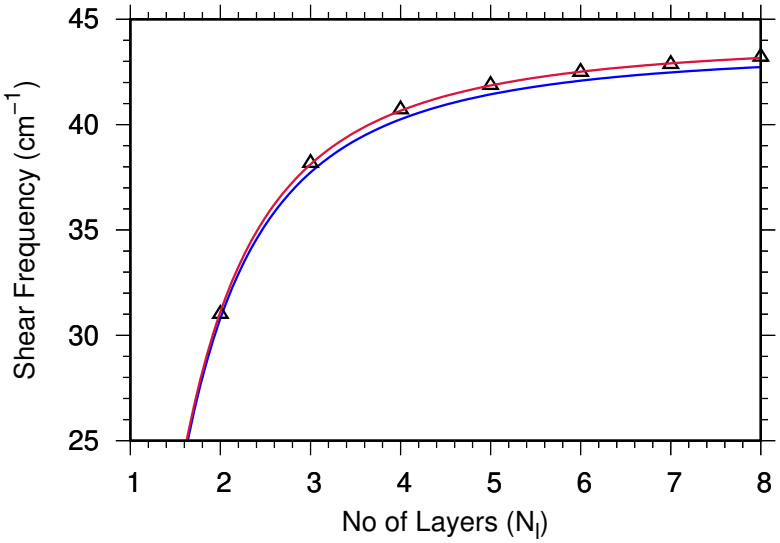


Figure 6.4: The variation in the shear mode frequency as a function of the number of layers, N_l, of graphene computed using MM^{Vib+D} (triangles) and its fitting to equation 6.5 (red) and experimental fitting (blue).[150]

not yet been able to probe these modes due to their low intensities. Figure 6.5 shows a comparison of the frequencies from MM^{Vib+D} with DFT-LDA results,[150] there is close agreement with the DFT frequencies, showing the potential is working well.

6.5 Multi-Wall Carbon Nanotubes

MWCNTs have inner diameters which range from 1 nm to about 20 nm, the interlayer distance between concentric tubes is reported to be approximately 3.4 Å measured by transmission electron microscopy.[153] As such the successive tube circumferences need to increase by about 21 Å which is

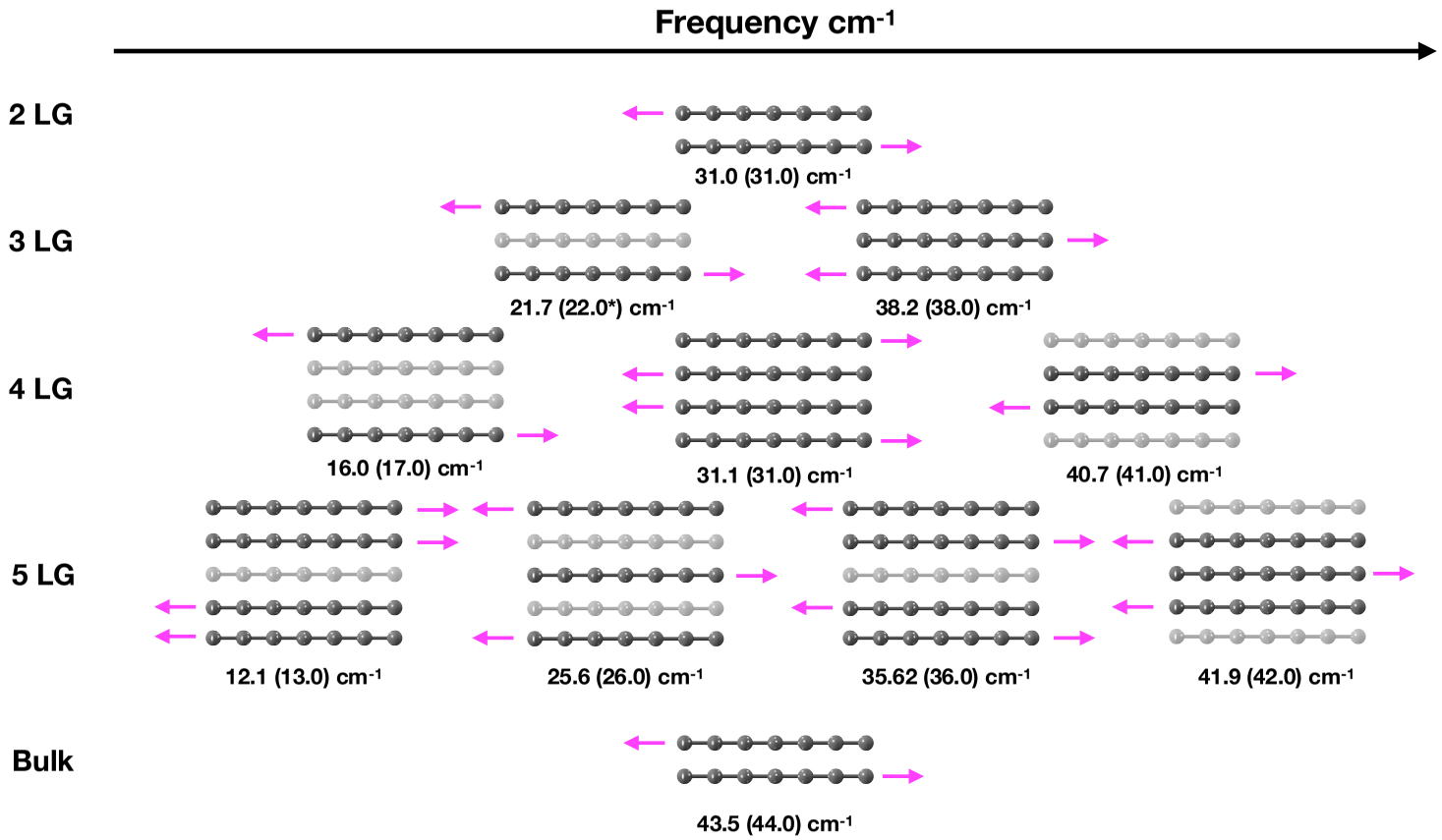


Figure 6.5: The normal mode displacements and frequencies for in-plane shear modes of N_lLG for $N_l = 2 - 5$ and bulk graphite computed using MM^{Vib+D}. Ab initio DFT-LDA frequencies by Ferrari *et al.*[150] are given in the parenthesis. *Value taken from Ping-Heng *et al.*[152]

not easily possible for zig-zag tubes without dislocations.[154] For armchair tubes, concentric tubes are much easier since successive tubes are able to meet very close to the required 21 Å, allowing multi-walled structures with an ABAB graphitic like stacking order possible, and an interlayer spacing close to 3.4 Å. MWCNTs are much more commercially available, and hence cost favours the use of MWCNTs. MWCNTs exhibit a variety of unique mechanical and electronic properties with potential applications in spintronics and field emission devices.[155]

Double walled carbon nanotubes (DWCNT) are the simplest class of MWCNTs that have received a lot of attention in the literature. This is primarily because they are prototypical systems of MWCNT's whilst also showing very unique properties at the same time, such as the fact that DWCNT bundles can adsorb twice as much H_2 compared with a close-packed SWNT bundles.[156] Additionally DWCNT, unlike a SWNT, can have one of four possible electronic configurations with each wall being either semiconductor (S) or metallic (M): S@S, M@S, M@M, and S@M (inner-tube@outer-tube), which has been investigated using resonance Raman spectroscopy.[157] DWCNTs have higher mechanical strength and better thermal and chemical stability compared to SWNTs. The unique double wall structure allows the outer wall to be selectively functionalised while maintaining an intact inner-tube.

Several studies have measured the Raman spectra of MWCNTs in aid of the characterisation of samples. In purified samples, low-frequency modes which are related to RBMs are revealed.[158–160] As with SWNTs, MWCNTs

RBMs are of large interest since they can allow for the characterisation of MWCNT structures, in particular, the diameters of the concentric tubes. However, the situation for MWCNTs is more complex since the RBMs of the concentric tubes will not act as independent oscillators since the Van der Waals interaction between the tubes is large enough that the individual vibrations will couple together. Here we investigate the RBMs modes of armchair MWCNTs and examine the effects on the RBMs relative to its single wall counterparts. Furthermore, we study the shearing modes of these systems and compare them with the shearing modes of FLG.

Here we use MM^{Vib+D} to investigate the following set of prototype armchair double wall tubes: (10,10)@(15,15), (15,15)@(20,20), (20,20)@(25,25), (10,10)@(15,15)@(20,20) and (10,10)@(15,15)@(20,20)@(25,25). These were modelled with PBCs with a 4 nm unit cell. Structurally, the interlayer separation of these tubes lies between ∼3.37-3.45 Å consistent with what is seen experimentally.[161] Non-chiral tubes MWCNTs are not studied here since they cannot be studied periodically and need to be studied using a finite modelling framework which is also possible with MM^{Vib+D}.

In MWCNTs two types of shear modes are seen as a result of its rolled structure, a linear set as shown in figure 6.6 and a rotational set shown in figure 6.7 computed from MM^{Vib+D}. Like FLG, for a given N_w number of walls, there will always be $N_w - 1$ rotational and linear shear modes. These two sets of modes show two very different sets of frequencies with different magnitudes. The frequencies of the linear shear modes tend to be much larger in magnitude, with an analogous progression to the modes seen in

FLG. The same can be said for the rotational modes, but the shearing frequencies tend to be much lower with these modes. These lower frequencies relate to the lower energy of rotation in the direction perpendicular to the nanotube axis. No reliable comments can be made about the intensity of these modes since no parameters for BPM for VDW bonds are developed, therefore the BPM has only been used to identify them.

The work of Popov *et al.*[162] utilised a fixed force constant model to study RBMs of MWCNTs, with a Lennard-Jones potential between concentric tubes, with this model structural optimisation of the layers isn't possible due to the fixed bonds and only interwall distance was optimised. Furthermore, tubes of greater than 3 layers were treated using continuum models. In this study, it was identified that the RBMs in MWCNTs with frequencies that are nearly equal to each other interact, leading to vibrational modes of strongly mixed character, i.e. the closer in frequency the modes are, the more strongly coupled the breathing mode. These modes are known as Coupled Radial Breathing modes (CRBM). Hence MWCNTs with large layer radii have RBMs that are the motion of many walls mixed in-phase and out of phase, an example is shown in figure 6.8. Figure 6.9 shows the CRBMs computed using MM^{Vib+D} for a series of armchair MWCNTS with the corresponding SWNT RBM, the contributing tubes to the normal mode shown with arrows and the phases of the CRBMs categorised. It can be seen that as we increase the number of walls in the tube the degree of mixing of the RBM tends to increase. This is reflected in the frequencies of the vibrational modes even for the double wall case where there is a small mixing, the hardening of both RBMs is seen, with

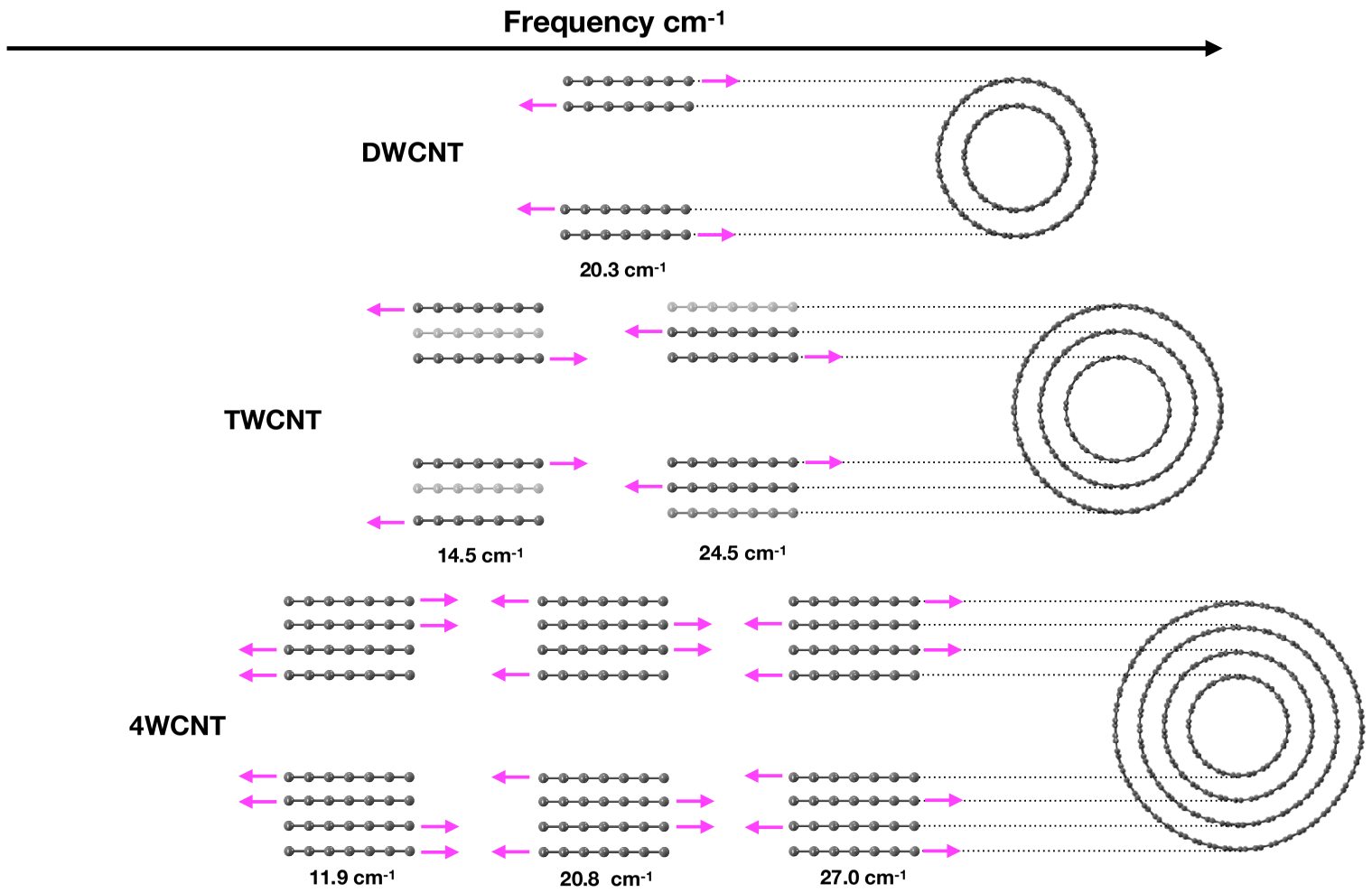


Figure 6.6: The normal mode displacements and frequencies for linear shear modes of MWCNTs computed using MM^{Vib+D} for (10,10)@(15,15), (10,10)@(15,15)@(20,20) and (10,10)@(15,15)@(20,20)@(25,25).

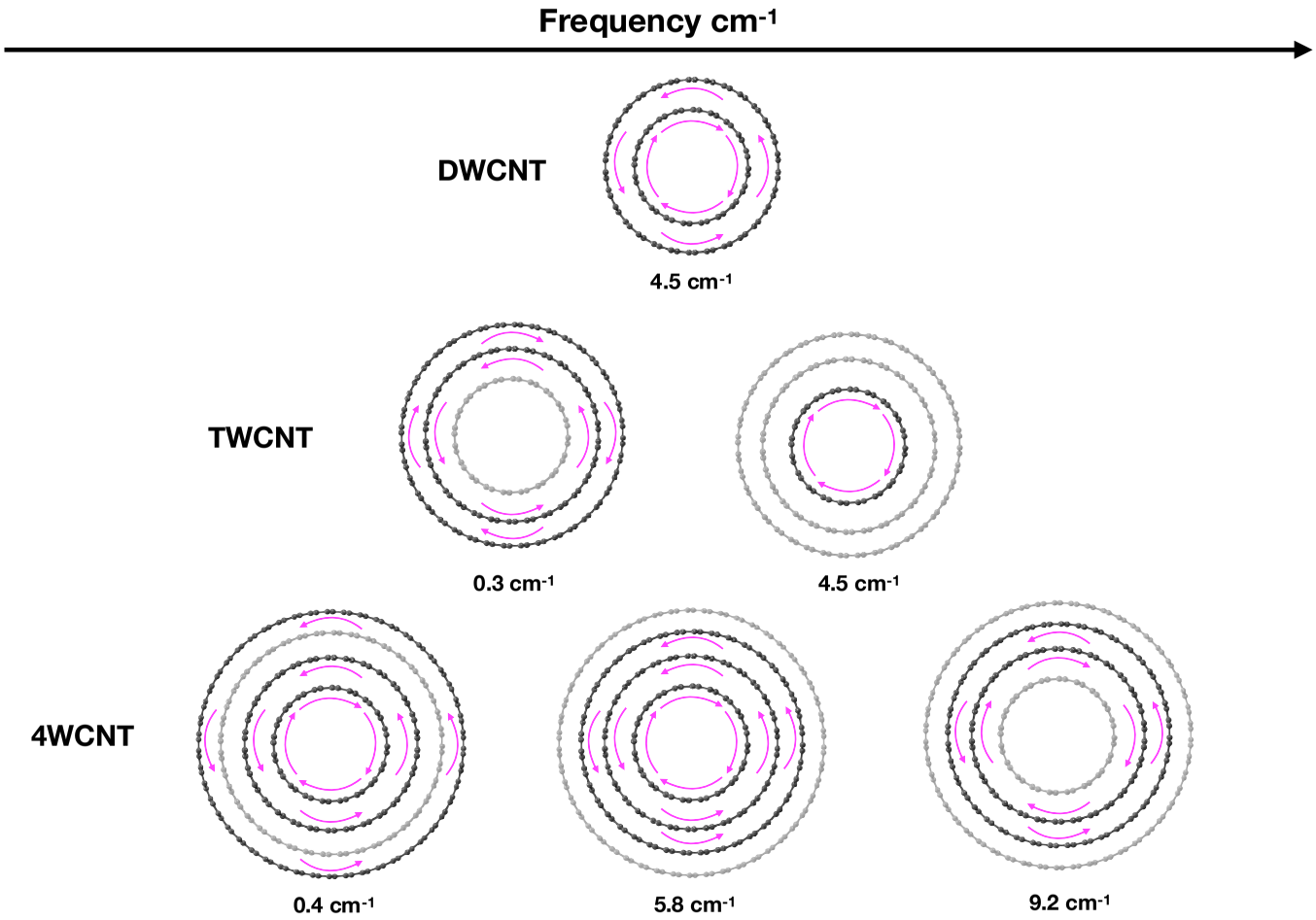


Figure 6.7: The normal mode displacements and frequencies for rotational shear modes of MWCNTs computed using MM^{Vib+D} for (10,10)@(15,15), (10,10)@(15,15)@(20,20) and (10,10)@(15,15)@(20,20)@(25,25).

a shift of 16.9 cm^{-1} for the (15,15) and an even larger shift of 38.7 cm^{-1} for the (10,10), this is unsurprising since it has become fully restrained by the outer (15,15) tube. Similarly, for the triple wall case, we see an even larger increase in the (15,15) RBM of 58.4 cm^{-1}, which becomes completely restrained from the inner direction by the (10,10) tube and from the outer by the (20,20) tube. Additionally, in all cases the in-phase mode is always the lowest frequency CRBM, the out of phase mode is always the highest frequency CRBM and all CRBMs between are a mixture of in-phase and out of phase motions. The energy ordering can be rationalised simply by the energy barriers of motion being lower for 100 % in-phase motions and the barriers for the counter-phase motions being higher.

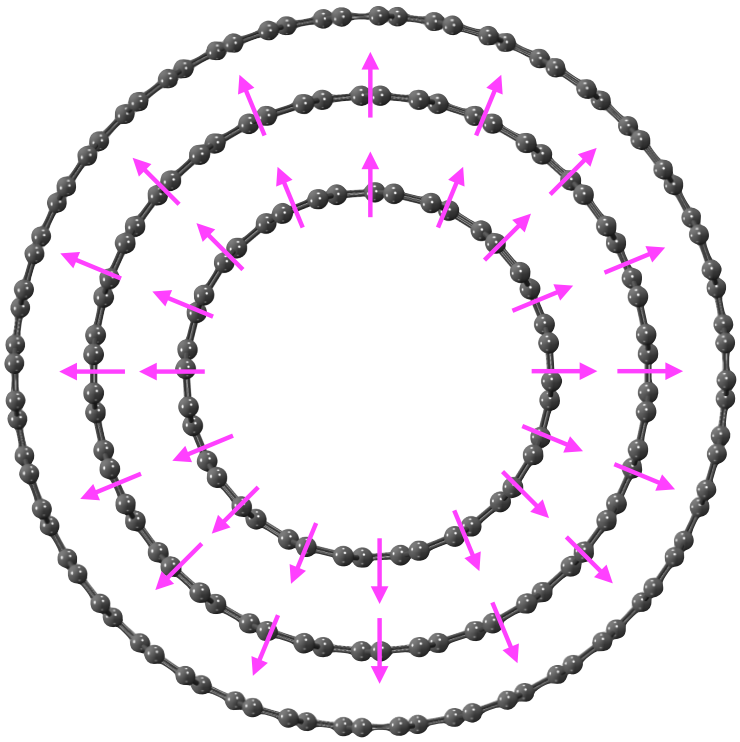


Figure 6.8: Representation of a coupled radial breathing mode in a TWCNT.

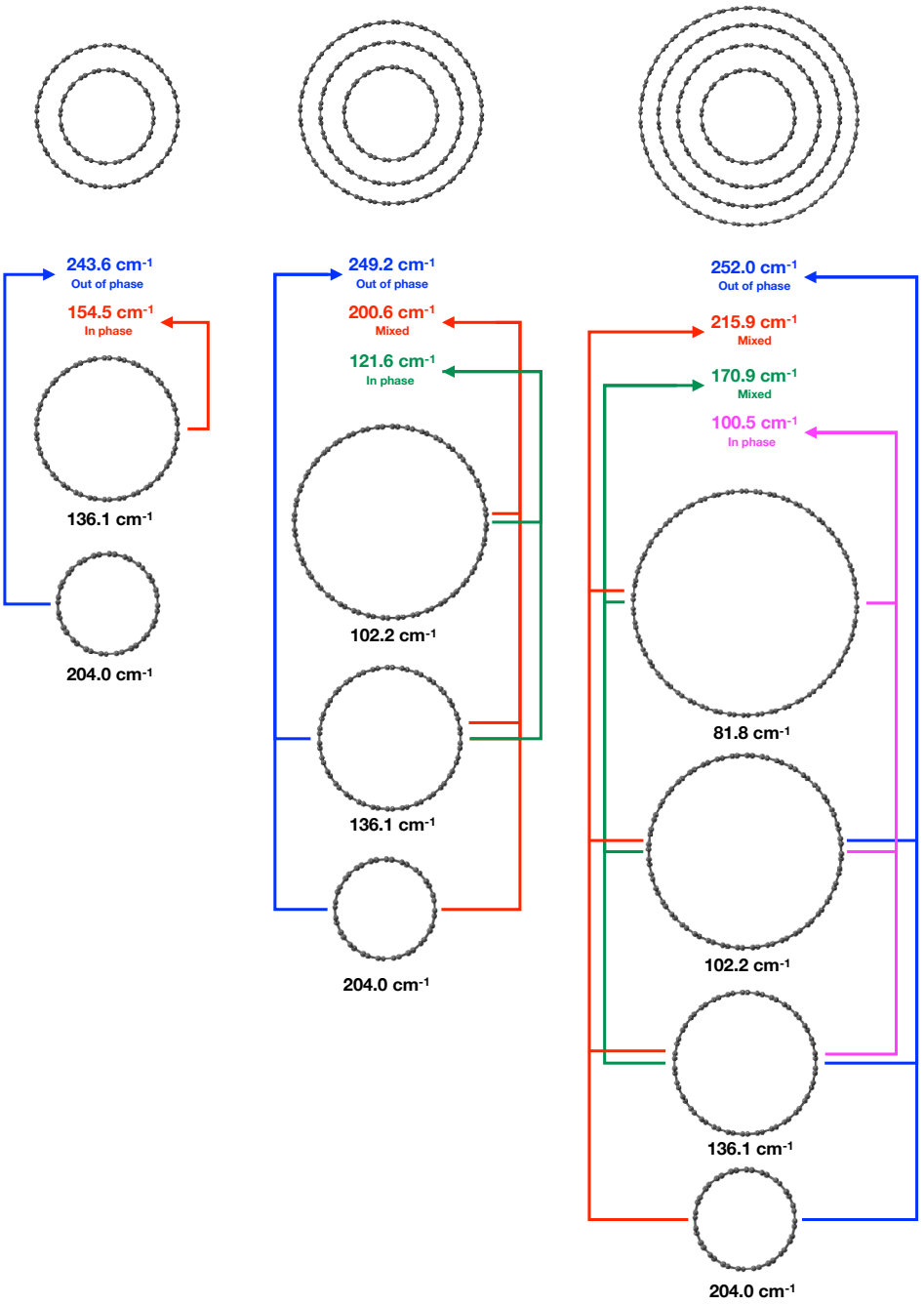


Figure 6.9: RBMs and CRBMs of SWNT ((10,10), (15,15) and (20,20)) and their MWCNT counterparts ((10,10)@(15,15), (10,10)@(15,15)@(20,20) and (10,10)@(15,15)@(20,20)@(25,25)) with the contributing SWNTs shown with arrows and phases of motions.

If we examine the change in the CRBMs for the DWCNT series (5,5)@(10,10), (10,10)@(15,15), (15,15)@(20,20) and (20,20)@(25,25). Figure 6.10 shows the CRBMs of the aforementioned DWCNTs with their normal modes. Generally, we see that the in-phase CRBMs originate from the outer tube, which can be identified from its frequency since it will have the lowest RBM frequency, corresponding to the wider diameter outer tube. Complimentary to this, the out of phase motioned CRBMs which originate from the inner tube can also be identified from its frequency since it will have the lowest RBM frequency, corresponding to the narrow diameter inner tube. For (20,20)@(25,25) we get a small amount of graphitisation between the walls of the tubes which results in the structure becoming a polygonal shape resulting in the CRBM becoming perturbed and difficult to assign but frequencies for an equivalent CRBM modes (polygonal-CRBM) could be found to be (with SWNT frequency in parentheses) 91.7 (81.8) cm^{-1} (in-phase) and 145.7 (102.2) cm^{-1} (out of phase).

Furthermore, as mentioned previously in work of Popov *et al.*,[162] we see that for small DWCNTs where the difference in frequencies are very large, there is no coupling in CRBMs. This can be seen from the normal mode displacement of the (5,5)@(10,10) DWCNT in figure 6.10, where the characteristic features of the RBM remain the same with negligible mixing. For larger DWCNTs (10,10)@(15,15) and (15,15)@(20,20), we see increasing coupling which is reflected in the normal mode displacements where significant coupling between the constituent walls is observed.

DWCNTS show only one rotational and one linear shear mode as we

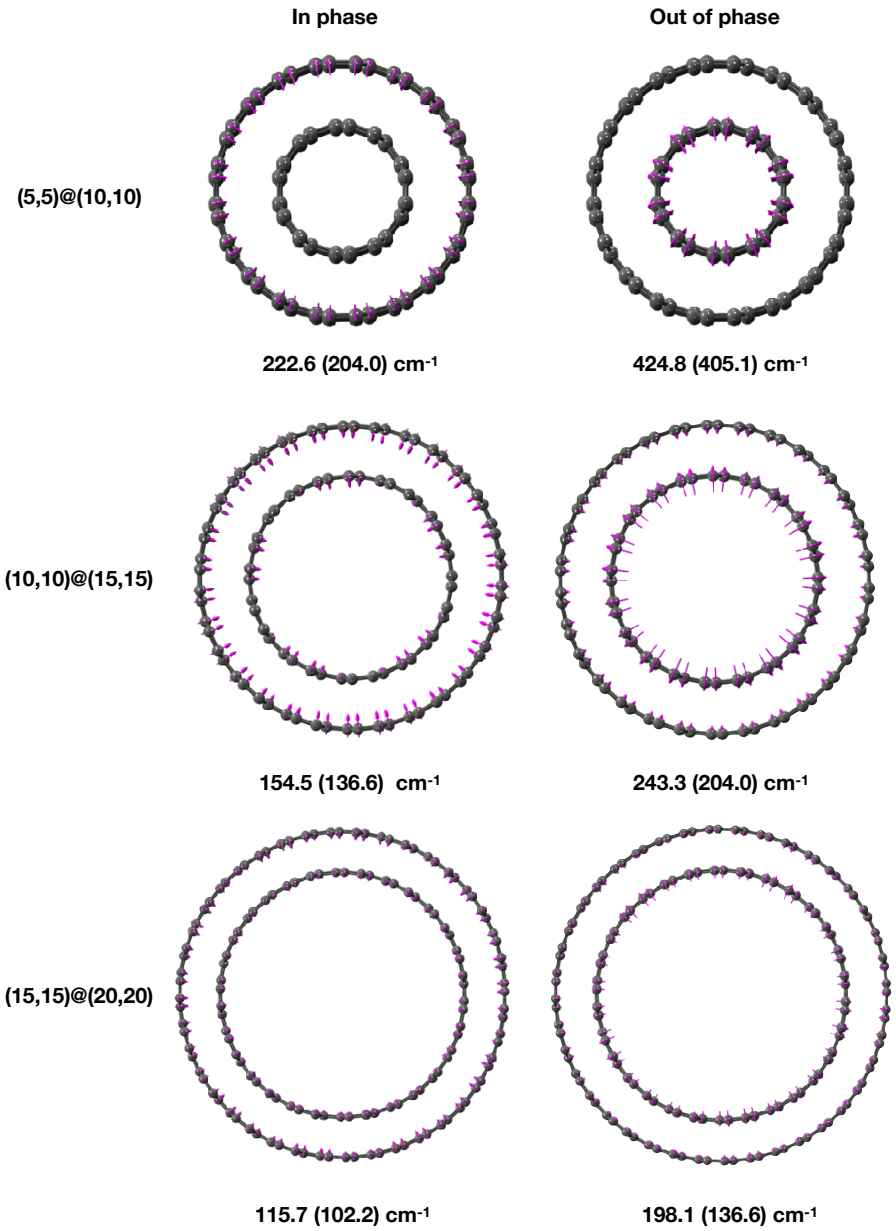


Figure 6.10: CRBM frequencies and normal modes of DWCNT. Constituent SWNT frequencies are given in parentheses.

saw in figures 6.6 and 6.7. Here we examine these shear modes of the DWCNTs as a function of inner diameter as shown in figure 6.11. It is clear that the linear shear mode is independent of the DWCNT diameter and stays constant at $\sim$20.5 cm^{-1}. In contrast, the rotational shear mode rapidly decreases in frequency with increasing diameter converging very close to zero. This indicates that the barrier to rotation decreases with diameter as well.

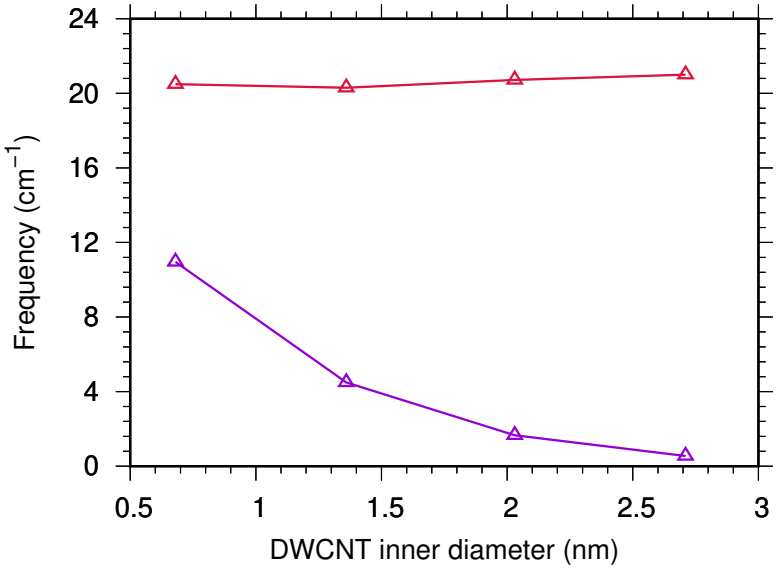


Figure 6.11: DWCNT rotational (purple) and linear (crimson) shear modes as a function of DWCNT inner diameter.

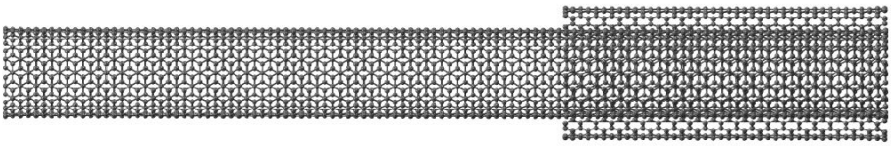
6.6 Coaxial Nanomotor

An area of current interest in the literature is the possibility of utilising DWCNTs as molecular motors. This can be achieved by exploiting the small interwall resistance of DWCNTs, in which a rotation or slide between

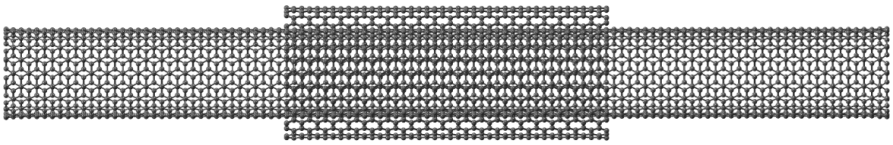
the inner and outer shells of DWCNTs can be easily performed, examples shown by Zettl *et al.*[163] include repeated extension and retraction of telescoping MWCNT segments, studied by transmission electron microscopy. The low friction interaction between inner and outer walls also makes it possible for the fabrication of a possible gigahertz oscillators, in which the repeated extension and retraction can be performed by the Van der Waals interactions between two concentric tubes.[164] Furthermore Zettl *et al.* has utilised DWNTs as a mass sensor, exploiting its increased rigidity to measure the resonant frequency change, which is proportional to the mass of the atom or molecule adsorbed, therefore they were able to measure the mass of gold atoms.[165]

In the spirit of the work by Zettl *et al.*,[163] we look at a DWNT system, where we have a mismatch in lengths as shown in figure 6.12. This nanomotor should allow for linear or rotational motion using carbon nanotubes as the primary components. The nanomotor system in which one short carbon nanotube moves relative to another coaxial nanotube has been studied by Bachtold *et al.*[166] The motion in this study was initiated by imposing a thermal gradient along the nanotube allowing for subnanometer displacements of the outer tube. These systems also represent interesting structures since they are similar to the junctions that were studied in section 3.3.8 and are prototypical components of molecular machines and could be thought as a macromolecular rotaxane analogue since they are threaded systems.[167]

Here we investigate a coaxial system of a 14 nm in lenght (10,10) SWNT with an outer 5 nm in length (15,15) SWNT (denoted as (10,10)-



(a) Coaxial 1



(b) Coaxial 2

Figure 6.12: The structures of a (10,10)-14nm@(15,15)-5nm coaxial nanotube.

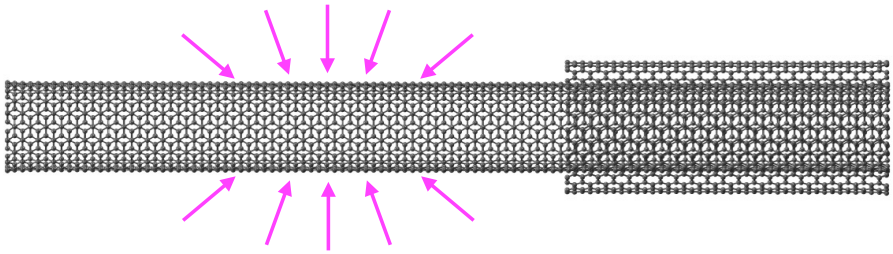
14nm@(15,15)-5nm) shown in figure 6.12 and examine the affect of moving the outer (15,15) component on key vibrational modes as shown in figures 6.12a and 6.12b, these structure will be referred to as coaxial 1 and coaxial 2, respectively.

Firstly, we examine the RBMs of the coaxial systems. The RBM frequencies of the component tubes are 182.8 cm^{-1} for the inner (10,10)-14nm and 133.5 cm^{-1} for the outer (15,15)-5nm. Upon forming coaxial 1 (figure 6.12a), there is a shift of the (10,10)-14nm RBM from 182.8 cm^{-1} to 185.8 cm^{-1}, a small increase, which likely results from the movement constraints imposed at the edge of the inner (10,10)'s RBM due to the outer tube, this mode also doesn't couple to the outer tube. For the (15,15)-5nm RBM there is a shift from 133.5 cm^{-1} to 146.7 cm^{-1} a large increase in frequency,

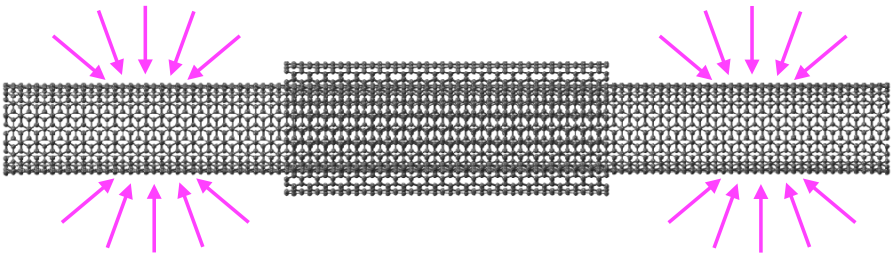
a result of becoming a CRBM. This however is localised to the 5 nm double walled portion of coaxial 1 with no normal mode components on the exposed single wall (10,10) section.

For coaxial 2 with the outer (15,15) positioned in the middle (figure 6.12b), there is a shift of the (10,10)-14nm RBM from 182.8 cm^{-1} to 192.6 cm^{-1}, a larger increase compared to coaxial 1, which is due to its central position allowing maximum Van der Waals interactions (and coupling) and constraint of movement on the inner tube at central position. For the (15,15)-5nm CRBM there is a shift of 133.5 cm^{-1} to 146.2 cm^{-1} showing no difference compared to the coaxial 1. As with coaxial 1, the CRBM is localised to 5 nm double walled portion of the tube, with no normal mode components on the exposed single wall (10,10) section on either side of the double walled section.

In figure 4.6a we saw that the RBM in finite tubes centre's in the middle of the tube, however upon becoming a coaxial DWCNT this may no longer be possible. Figure 6.15b and 6.14b show the normal modes of the inner (10,10) in coaxial 1 and coaxial 2, respectively. It can be seen that the (15,15) outer section essentially acts as a node on the RBM. In coaxial 1 the centre of the RBM mode is shifted along the tube to the centre between the end of the outer tube (15,15) and end of the inner (10,10). In contrast, with the placement of the outer tube to the middle in coaxial 2, we see there are 2 RBM centres on either side of the outer (15,15) on the (10,10) tube.



(a) Coaxial 1



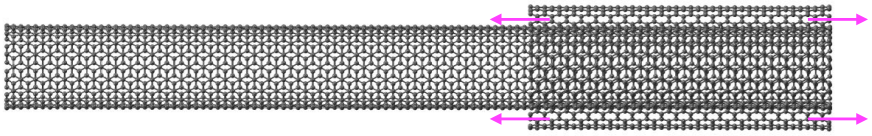
(b) Coaxial 2

Figure 6.13: Representation of the RBM of the inner (10,10) tube in a (10,10)-14nm@(15,15)-5nm coaxial nanotube.

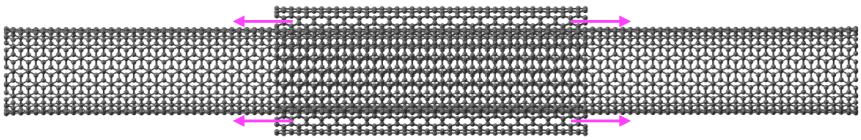
As with MWCNTs, we see an axial and rotational shear mode. Upon moving the outer (15,15) tube from the side to the middle, the rotational shear mode shifts from 1.3 cm^{-1} to 1.9 cm^{-1} and the axial shear mode shifts from 10.3 cm^{-1} to 14.8 cm^{-1}. The larger increase in the axial shear mode can be attributed to the increase in the Van der Waals interactions in the longitudinal direction upon being placed in the middle.

For the G-band modes, we see that there is an overall shift of the frequency of these modes of by approximately 30 cm^{-1} upon threading. However, there are few significant differences seen upon comparison of coaxial 1 and coaxial 2 structures.

The work by Bachtold *et al.*[166] aimed to utilise the shearing motions of



(a) Coaxial 1



(b) Coaxial 2

Figure 6.14: Representation of the axial shear mode of a (10,10)-14nm@(15,15)-5nm coaxial nanotube.

the outer tube to ship molecular cargo along a carbon nanotube rail. Although temperature gradient was used to induce motion, a possible solution was suggested to selectively excite specific vibrational modes in particularly exciting the breathing modes. Using MM^{Vib+D} could provide potential target modes to excite for such an approach, such as the combination of the RBM in 6.15b and exciting the axial shear mode to provide an effective route in transferring momentum to move the outer cargo tube. Furthermore, the shifts in frequencies of RBMs could potentially provide a method for locating the cargo's positions along the carbon nanotube rail.

6.7 Graphitic Nanofibres

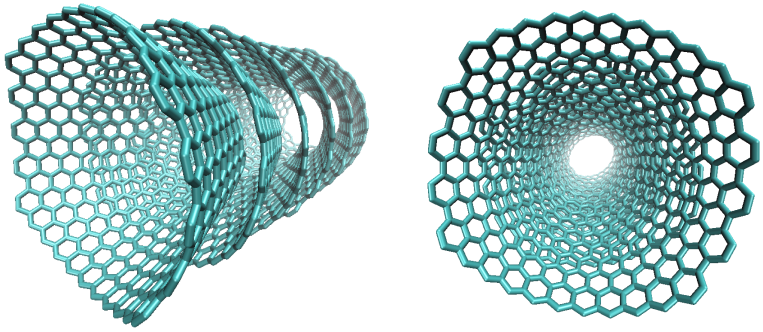
A more recent class of carbon nanomaterials are graphitic nanofibres. They are fibres that comprise of layers of graphite planes/nanocones stacked par-

allel or at a certain angle from the fibre axis. In this section, we focus our attention to the simulation of the vibrational spectroscopy of cup stacked graphitic nanofibres (or hat stacked carbon nanofibres). This material can be thought of as the multi-layer analogues of the nanocones studied in section 3.3.9. The attraction of this material is for its applications in polymer conductive composites, which are materials that exhibit superior electrical and thermal properties compared to conventional conductive polymer composites.[168] Furthermore its application as a support for metal nanoparticle catalysts is being explored as well as its use as an electrochemical capacitor.[169–172]

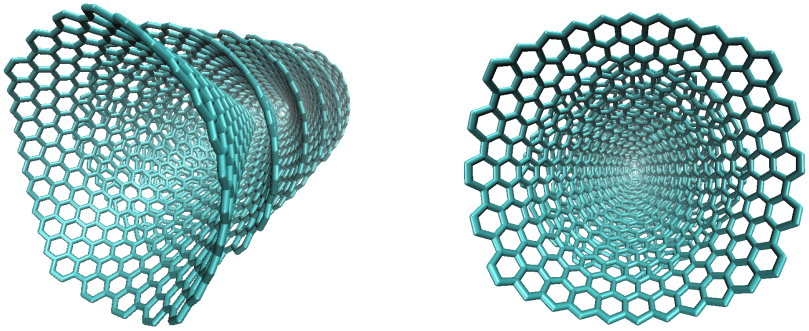
The nanofibre has been observed in TEM to be either solid or have a hollow core surrounded by concentric cup stacked planes, and their structure is shown in figure 6.15. These types of structures have a large number of reactive edges both inside and outside the nanofibre making it a versatile material.[173,174] The spacing between these cups are similar to that of graphene sheets and are reported to be 0.34 nm.

The vibrational spectroscopy of graphitic nanofibres is not as well established as its carbon nanotube counterparts, hence here the explore the relationship between structure and Raman spectra of graphitic nanofibres.

To study a nanofibre we require a unit nanocone to build its structure, here the model fibre is finite and built from $n = 4$, $\chi = 60.0°$ nanocone with either 3 or 4 units. As shown earlier, the graphitic nanofibre can either have a solid or hollow core. Naturally, we draw the question of whether this can



(a) Hollow core graphitic nanofibre



(b) Solid core graphitic nanofibre

Figure 6.15: Representation of the structure of a solid and hollow cup stacked graphitic nanofibre built from a $n = 4$, $\chi = 60.0°$.

be identified to aid in its characterisation. More specifically, we ask the question of how can we check if a graphitic nanofibre has a hollow or solid core. Additionally, how can the diameter, d_t, of a hollow core graphitic nanofibre be identified just as the diameter of a carbon nanotube can be determined.

Since the graphitic nanofibres modelled here are made up of $n = 4$, $\chi = 60.0°$ nanocones, their hollow core is no longer a perfect circle but rather an ellipse. To define the diameter d_t of this ellipse we use the major axis as shown in figure 6.16. Figure 6.17 and 6.18 show the change in frequency of two Raman active modes from a Raman spectrum simulated using a covalent BPM in the low-frequency region. These are sensitive to the hollow core diameter with the first being a disordered bending mode (DBM), and the second being a disordered RBM (d-RBM). Both of these show an inverse relationship with the elliptical diameter of the hollow core. In comparison with carbon nanotubes where the RBM decreases with increasing diameter, we find that both these modes increase with increasing elliptical diameter. Both these modes can be fitted to an inverse equation of the form:

$$\omega = \frac{A}{d_t - B} + C \tag{6.6}$$

For the d-RBM, we get following coefficients after fitting, A = -1203.8 cm^{-1} Å, B = 3.4 Å and C = 114.6 cm^{-1}. For the DBM we get following coefficients after fitting, A =-10363.2 cm^{-1} Å , B = 24.4 Å and C = 11.5 cm^{-1}. The values of A show that the frequencies vary at largely different rates between the two modes. This variation overall shows that these modes could potentially be utilised to identify diameters (or diameter distributions) of graphitic nanofibres. One thing to note is that these values may

show specificity depending on the graphitic fibre of interest since there are numerous nanocone units that could be used to build its structure. Therefore these values are unique to a nanofibre built from $n = 4$, $\chi = 60.0°$ nanocones.

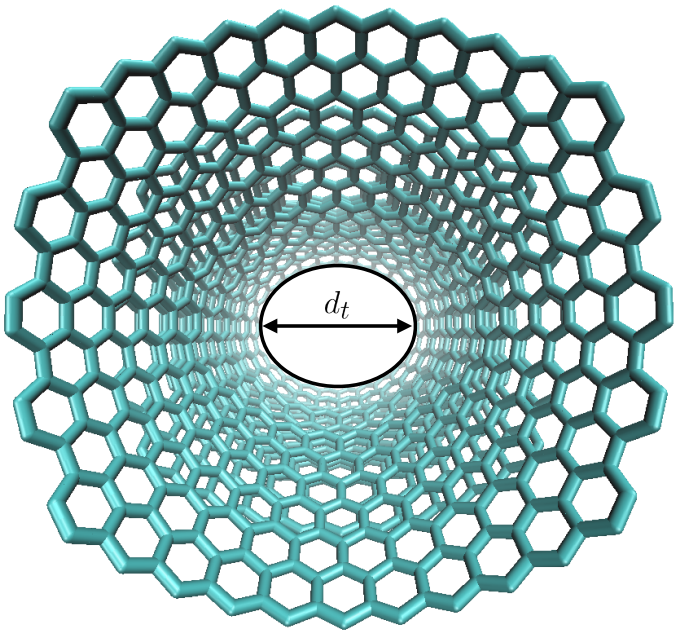


Figure 6.16: Diameter, d_t, of a graphitic nanofibre hollow core taken as the major axis.

Figure 6.19 shows the variation in the G-band from a solid graphitic nanofibre to a hollow fibre with a diameter of 20 Å. As with carbon nanotubes, these are in-plane vibrations of carbon atoms. We see a similar splitting of the G-band up to a $d_t = 12.9$ Å, however, this splitting is merely an artifact of the finite structure of the simulation, where the lower band is associated with the end nanocone unit as such we should actually expect a single band that is continuous, a larger number of units would be more appropriate to get a better representation of this band. Nonethe-

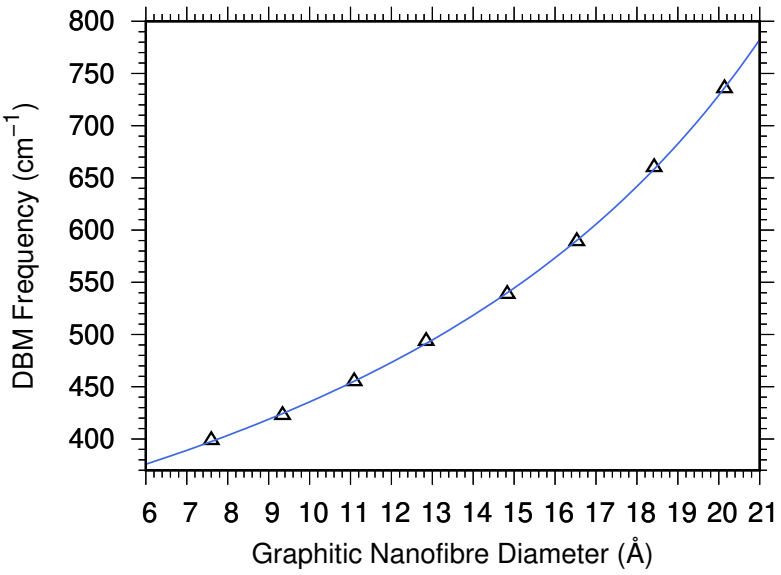


Figure 6.17: Change in DBM frequency of a graphitic nanofibre with increasing core diameter.

less, the inset line shown marks the G-band position, where the intensity is made up of both tangential and longitudinal in-plane modes, generally with increasing diameter we see the G-band broadens which can be associated with decreasing graphitic planes as the hollow core diameter increases.

The modes investigated here are identified on the Raman activity based on a covalent BPM hence some VDW modes maybe under represented. A consistent set of combined parameters need to be developed for both VDW and covalent bonds to allow for a balance treatment to produce more representative spectra. However, it has still been shown that the vibrational modes and Raman of these systems are sensitive to their structure and could be used for the extraction of a key geometrical parameter like the hollow core diameter.

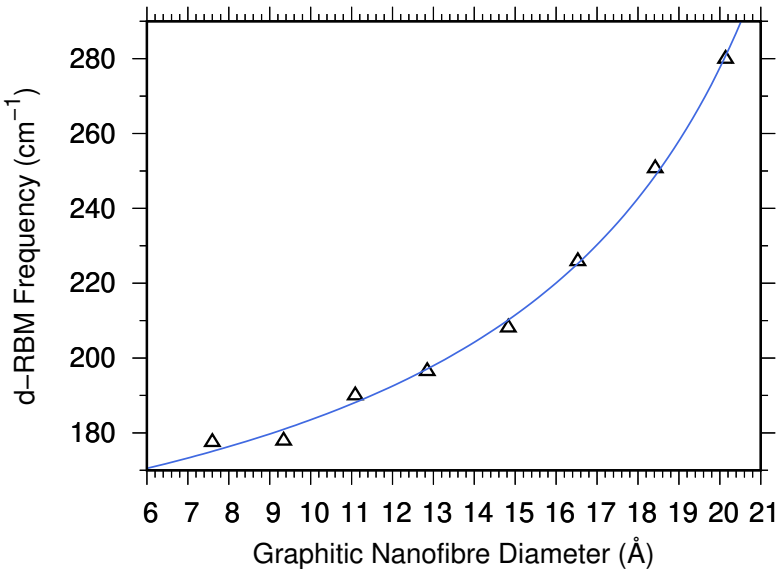


Figure 6.18: Change in d-RBM frequency of a graphitic nanofibre with increasing core diameter.

6.8 Conclusions

MM^{Vib} has been extended to study multi-layer carbon nanomaterials by the addition of dispersion, MM^{Vib+D}. The new parameters for the dispersion model have been developed and accurately describe the shearing modes of FLG, comparing well with experiment. This potential was then applied to study MWCNTs, and a set of linear and rotational shear modes were identified similar to that of FLG. The CRBMs of a MWCNT were investigated showing coupling increases with increasing number of layers and that the highest frequency CRBM is out of phase and the lowest CRBM is in-phase. DWCNTs were also shown to have a rotational shear mode which varied with diameter and a linear shear mode which remained constant regardless of diameter. The coupling of CRBMs of the DWCNTs

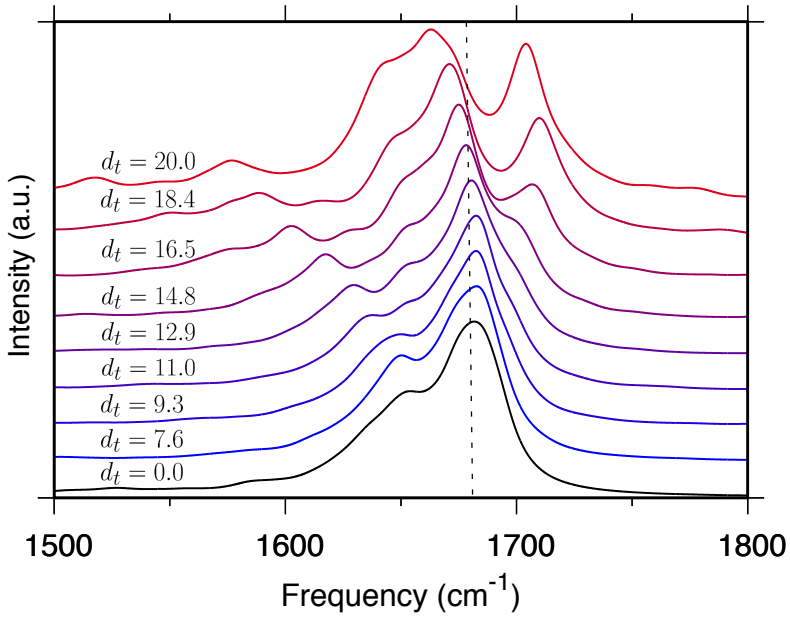


Figure 6.19: Change in G-band of a graphitic nanofibre with increasing core diameter.

was shown to increase with the DWCNT inner diameter as the frequencies of constituent SWNTs get close in energy. MM^{Vib+D} was then applied to study solid and hollow graphitic nanofibres. A set of possible Raman active modes were identified and found to vary with an inverse relationship with the hollow core diameter, allowing an analogues method of characterising the structure of these materials like nanotube diameter.

Chapter 7

Concluding Remarks and Future Directions

This thesis has covered several projects focusing on the main aim of studying the vibrational spectroscopy of carbon nanomaterials using an empirical potential. The Murrell-Mottram potential was parameterised and combined with the bond polarisability model to simulate both single and multilayer carbon systems.

In chapter 3, we developed the potential using a random search Hessian-matching approach which successfully produced a set of good parameters which yielded good structures for both graphene and carbon nanotubes. For vibrational spectroscopy, we found that for nanotubes the potential worked well giving experimentally comparable Raman spectra and properties like RBM-diameter relations. However, limitations were found when considering nanotubes where quantum mechanical effects are dominant on its vibrational modes, in particular, metallic tubes. For graphene, we found the potential worked reasonably well with an overestimation in frequencies

and was attributed to the potential being parameterised with a curved structure. The potential was then applied to study the effects of the inclusion of Stone-Wales defects showing new bands and modes. Furthermore, carbon nanotube junctions were studied showing that the Raman spectra are a superposition of the component nanotubes and carbon nanocones were shown to have a Raman band which could be used to assign cone apex angles.

In chapter 4, we used the potential to compare the various types of modelling methods exploring how vibrational properties compare when doing simulations within a periodic, finite and tethered framework. It was clear that the logical outcome of the periodic results matching the finite at larger enough system sizes was shown. However, it was demonstrated that different modes/properties converge at very different rates. In particular, when comparing the key Raman active modes, the G-band and RBM in carbon nanotubes, it was shown that all methods lead to different normal mode vectors for some modes, most interestingly was the RBM. In the case of graphene these difference's lead to different sets of modes in particular in the case when graphene edges are present in finite simulations and are free to move. Here we saw a large progression of Raman active modes from these free edges "flapping" which was not present in experiment since free graphene is not a good approximation to graphene's form in experimental setups where it's supported on some form of substrate or grid.

In chapter 5, we applied the potential to model the vibrational spectroscopy of carbon nanotubes under strain. Here we found that consistent

with experimental studies, the LO band is shifted under strain. However, the shift rates were found to be almost constant regardless of chirality or diameter of nanotubes which was found in ab initio studies but not observed in experiment. Overall the potential reproduced qualitative effects of strain, but with limitations and difficulty in experiment, a quantitative comparison isn't possible.

In chapter 6, we extended the Murrell-Mottram potential to include dispersion interactions. A variety of multi-layer systems were studied including few-layer graphene, MWCNTs, a coaxial nanomotor and graphitic nanofibres. A set of new parameters to model dispersion yielded good interlayer distances for FLG and MWCNTs. The new dispersion interaction accurately modelled the frequencies of FLG's shearing mode and was subsequently applied to study the linear and rotation shear modes of a series of armchair MWCNTs and DWCNTS. Furthermore, it was found for armchair MWCNTs the lowest CRBM is always in-phase and the highest CRBM is out of phase. Lastly, the potential was applied to study a new emerging carbon nanomaterial, graphitic nanofibres. In particular cup stacked fibres were studied and modes sensitive to the hollow core diameter were found and an inverse relationship was identified.

Looking into the future for this work, there are several possible directions to take. The first is utilising the potential in molecular dynamics and simulating vibrational spectra through the use of the Fourier transform of auto-correlation functions of velocity for VDOS and polarisability for Raman spectra. These approaches are known to take account of anhar-

monicity in vibrational modes and hence provides a route to more accurate spectra without the use of scaling factors and a chance to actually examine the anharmonic effects in carbon nanotubes.

Secondly would be extending the potential to include further elements such as hydrogen for modelling hydrogen terminated tubes, carbon nanoribbons and poly-aromatic hydrocarbons. This could be implemented through the addition of a single two-body interaction term for hydrogen with carbon since they are always sp^2 terminating atoms. Additionally would be to include inorganic species which are popularly encapsulated into carbon nanotubes and studying the effects on encapsulations on a nanotube vibrational properties.

Thirdly would be investigating the use of nanotubes as mass sensors utilising the shift in vibrational frequencies which can be easily studied using the current MM potential at a low computational cost. This is by incrementally increasing the mass of atoms in particular regions such as end of a nanotube or the middle and repeated diagonalisation of the hessian matrix with increasing (or decreasing) atomic mass of carbon atoms. This will allow for mass-frequency relationships to be determined, but also can be further be extended to the relationship of the dependence of frequency, on the spread on mass over increasingly large areas on a nanotube.

Lastly would be attempting to simulate Raman images. Spectroscopic imaging techniques have become a popular tool in materials characterisation and Raman is no exception. With the capability to simulate many thousands of atoms it may be possible to attempt to simulate Raman im-

ages based on shifts in frequency, intensity ratios or changes. Examples include image simulation of stepped edges in FLG samples using the frequency changes in shears modes or using the RBM of a tube to simulate a large networked carbon nanotube junction to map out its structure. Such capability would provide a complementary approach to experiment and deeper insights.

Bibliography

[1] R. P. Feynman, *Journal of Microelectromechanical Systems*, 1992, **1**, 60–66.

[2] M. Fulekar, *Nanotechnology: Importance and Applications*, I.K. International Publishing House, 2010.

[3] P. O'Brien, H. Craighead, H. Kroto and M. Amer, *Raman Spectroscopy, Fullerenes and Nanotechnology*, Royal Society of Chemistry, 2010.

[4] T. Susi, T. Pichler and P. Ayala, *Beilstein Journal of Nanotechnology*, 2015, **6**, 177192.

[5] M. Greene, C. Kinser, D. Kramer, L. Pingree and M. Hersam, *Microscopy Research and Technique*, **64**, 415–434.

[6] Z. Bingsen and S. D. Sheng, *Small*, **10**, 222–229.

[7] S. Logothetidis, *Nanostructured Materials and Their Applications*, Springer Berlin Heidelberg, 2012.

[8] P. O'Brien, H. Craighead and H. Kroto, *Raman Spectroscopy, Fullerenes and Nanotechnology*, The Royal Society of Chemistry, 2010, pp. P001–P288.

[9] J. M. Yuk, J. Park, P. Ercius, K. Kim, D. J. Hellebusch, M. F. Crommie, J. Y. Lee, A. Zettl and A. P. Alivisatos, *Science*, 2012, **336**, 61–64.

[10] R. H. Baughman, A. A. Zakhidov and W. A. de Heer, *Science*, 2002, **297**, 787–792.

[11] J. Ferraro, *Introductory Raman Spectroscopy*, Elsevier Science, 2003.

[12] I. Kopova, L. Bacakova, V. Lavrentiev and J. Vacik, *International Journal of Molecular Sciences*, 2013, **14**, 9182–9204.

[13] H. W. Kroto, J. R. Heath, S. C. O'Brien, R. F. Curl and R. E. Smalley, *Nature*, 1985, **318**, 162 EP –.

[14] K. S. Novoselov, A. K. Geim, S. V. Morozov, D. Jiang, Y. Zhang, S. V. Dubonos, I. V. Grigorieva and A. A. Firsov, *Science*, 2004, **306**, 666–669.

[15] M. Dresselhaus, *Graphite fibers and filaments*, Springer-Verlag, 1988.

[16] J. Klett, R. Hardy, E. Romine, C. Walls and T. Burchell, *Carbon*, 2000, **38**, 953–973.

[17] E. B. Barros, N. S. Demir, A. G. Souza Filho, J. Mendes Filho, A. Jorio, G. Dresselhaus and M. S. Dresselhaus, *Physical Review B*, 2005, **71**, 165422.

[18] L. G. Cançado, M. A. Pimenta, B. R. A. Neves, G. Medeiros-Ribeiro, T. Enoki, Y. Kobayashi, K. Takai, K. Fukui, M. S. Dresselhaus, R. Saito and A. Jorio, *Physical Review Letters*, 2004, **93**, 047403.

[19] M. Dresselhaus, G. Dresselhaus and P. Eklund, *Science of Fullerenes and Carbon Nanotubes: Their Properties and Applications*, Elsevier Science, 1996.

[20] M. Dresselhaus, G. Dresselhaus, R. Saito and A. Jorio, *Physics Reports*, 2005, **409**, 47–99.

[21] R. Saito, G. Dresselhaus and M. Dresselhaus, *Physical Properties of Carbon Nanotubes*, 1998.

[22] L. Malard, M. Pimenta, G. Dresselhaus and M. Dresselhaus, *Physics Reports*, 2009, **473**, 51–87.

[23] A. Jorio, M. A. Pimenta, A. G. S. Filho, R. Saito, G. Dresselhaus and M. S. Dresselhaus, *New Journal of Physics*, 2003, **5**, 139.

[24] F. Jensen, *Introduction to Computational Chemistry*, John Wiley & Sons, 2006.

[25] C. Cramer, *Essentials of Computational Chemistry: Theories and Models*, Wiley, 2005.

[26] D. W. Brenner, O. A. Shenderova, J. A. Harrison, S. J. Stuart, B. Ni and S. B. Sinnott, *Journal of Physics: Condensed Matter*, 2002, **14**, 783.

[27] S. J. Stuart, A. B. Tutein and J. A. Harrison, *The Journal of Chemical Physics*, 2000, **112**, 6472–6486.

[28] S. G. Srinivasan, A. C. T. van Duin and P. Ganesh, *The Journal of Physical Chemistry A*, 2015, **119**, 571–580.

[29] P. Zhang, L. Ma, F. Fan, Z. Zeng, C. Peng, P. E. Loya, Z. Liu, Y. Gong, J. Zhang, X. Zhang, P. M. Ajayan, T. Zhu and J. Lou, *Nature Communications*, 2014, **5**, 3782.

[30] C. Herbig, E. H. Ahlgren and T. Michely, *Nanotechnology*, 2017, **28**, 055304.

[31] T. Takai, C. Lee, T. Halicioglu and W. A. Tiller, *The Journal of Physical Chemistry*, 1990, **94**, 4480–4482.

[32] B. R. Eggen, R. L. Johnston and J. N. Murrell, *Journal of the Chemical Society, Faraday Transactions*, 1994, **90**, 3029–3037.

[33] J. N. Murrell and R. E. Mottram, *Molecular Physics*, 1990, **69**, 571–585.

[34] H. Cox, R. L. Johnston and J. N. Murrell, *Journal of Solid State Chemistry*, 1999, **145**, 517–540.

[35] S. Guha, J. Menéndez, J. B. Page and G. B. Adams, *Physical Review B*, 1996, **53**, 13106–13114.

[36] R. Saito, M. Furukawa, G. Dresselhaus and M. S. Dresselhaus, *Journal of Physics: Condensed Matter*, 2010, **22**, 334203.

[37] R. Saito, T. Takeya, T. Kimura, G. Dresselhaus and M. S. Dresselhaus, *Physical Review B*, 1998, **57**, 4145–4153.

[38] P. Hohenberg and W. Kohn, *Physical Review*, 1964, **136**, B864–B871.

[39] Y. A. Wang, N. Govind and E. A. Carter, *Physical Review B*, 1999, **60**, 16350–16358.

[40] S. S. Iyengar, M. Ernzerhof, S. N. Maximoff and G. E. Scuseria, *Physical Review A*, 2001, **63**, 052508.

[41] W. Kohn and L. J. Sham, *Physical Review*, 1965, **140**, A1133–A1138.

[42] C. Lee, W. Yang and R. G. Parr, *Physical Review B*, 1988, **37**, 785–789.

[43] G. Ortiz and P. Ballone, *Physical Review B*, 1991, **43**, 6376–6387.

[44] J. Tao, J. P. Perdew, V. N. Staroverov and G. E. Scuseria, *Physical Review Letters*, 2003, **91**, 146401.

[45] Y. Zhao and D. G. Truhlar, *The Journal of Chemical Physics*, 2006, **125**, 194101.

[46] R. Peverati and D. G. Truhlar, *The Journal of Physical Chemistry Letters*, 2012, **3**, 117–124.

[47] T. Yanai, D. P. Tew and N. C. Handy, *Chemical Physics Letters*, 2004, **393**, 51–57.

[48] O. A. Vydrov and T. V. Voorhis, *The Journal of Chemical Physics*, 2010, **133**, 244103.

[49] R. Ditchfield, W. J. Hehre and J. A. Pople, *The Journal of Chemical Physics*, 1971, **54**, 724–728.

[50] A. D. Becke, *The Journal of Chemical Physics*, 1993, **98**, 5648–5652.

[51] C. Lee, W. Yang and R. G. Parr, *Physical Review B*, 1988, **37**, 785–789.

[52] S. H. Vosko, L. Wilk and M. Nusair, *Canadian Journal of Physics*, 1980, **58**, 1200–1211.

[53] P. J. Stephens, F. J. Devlin, C. F. Chabalowski and M. J. Frisch, *The Journal of Physical Chemistry*, 1994, **98**, 11623–11627.

[54] A. P. Scott and L. Radom, *The Journal of Physical Chemistry*, 1996, **100**, 16502–16513.

[55] J. P. Merrick, D. Moran and L. Radom, *The Journal of Physical Chemistry A*, 2007, **111**, 11683–11700.

[56] Y. Shao, Z. Gan, E. Epifanovsky, A. T. Gilbert, M. Wormit, J. Kussmann, A. W. Lange, A. Behn, J. Deng, X. Feng, D. Ghosh, M. Goldey, P. R. Horn, L. D. Jacobson, I. Kaliman, R. Z. Khaliullin, T. Ku, A. Landau, J. Liu, E. I. Proynov, Y. M. Rhee, R. M. Richard, M. A. Rohrdanz, R. P. Steele, E. J. Sundstrom, H. L. W. III, P. M. Zimmerman, D. Zuev, B. Albrecht, E. Alguire, B. Austin, G. J. O. Beran, Y. A. Bernard, E. Berquist, K. Brandhorst, K. B. Bravaya, S. T. Brown, D. Casanova, C.-M. Chang, Y. Chen, S. H. Chien, K. D. Closser, D. L. Crittenden, M. Diedenhofen, R. A. D. Jr., H. Do, A. D. Dutoi, R. G. Edgar, S. Fatehi, L. Fusti-Molnar, A. Ghysels, A. Golubeva-Zadorozhnaya, J. Gomes, M. W. Hanson-Heine, P. H. Harbach, A. W. Hauser, E. G. Hohenstein, Z. C. Holden, T.-C. Jagau, H. Ji, B. Kaduk, K. Khistyaev, J. Kim, J. Kim, R. A. King, P. Klunzinger, D. Kosenkov, T. Kowalczyk, C. M. Krauter, K. U. Lao, A. D. Laurent, K. V. Lawler, S. V. Levchenko, C. Y. Lin, F. Liu, E. Livshits, R. C. Lochan, A. Luenser, P. Manohar, S. F. Manzer, S.-P. Mao, N. Mardirossian, A. V. Marenich, S. A. Maurer, N. J.

Mayhall, E. Neuscamman, C. M. Oana, R. Olivares-Amaya, D. P. ONeill, J. A. Parkhill, T. M. Perrine, R. Peverati, A. Prociuk, D. R. Rehn, E. Rosta, N. J. Russ, S. M. Sharada, S. Sharma, D. W. Small, A. Sodt, T. Stein, D. Stck, Y.-C. Su, A. J. Thom, T. Tsuchimochi, V. Vanovschi, L. Vogt, O. Vydrov, T. Wang, M. A. Watson, J. Wenzel, A. White, C. F. Williams, J. Yang, S. Yeganeh, S. R. Yost, Z.-Q. You, I. Y. Zhang, X. Zhang, Y. Zhao, B. R. Brooks, G. K. Chan, D. M. Chipman, C. J. Cramer, W. A. G. III, M. S. Gordon, W. J. Hehre, A. Klamt, H. F. S. III, M. W. Schmidt, C. D. Sherrill, D. G. Truhlar, A. Warshel, X. Xu, A. Aspuru-Guzik, R. Baer, A. T. Bell, N. A. Besley, J.-D. Chai, A. Dreuw, B. D. Dunietz, T. R. Furlani, S. R. Gwaltney, C.-P. Hsu, Y. Jung, J. Kong, D. S. Lambrecht, W. Liang, C. Ochsenfeld, V. A. Rassolov, L. V. Slipchenko, J. E. Subotnik, T. V. Voorhis, J. M. Herbert, A. I. Krylov, P. M. Gill and M. Head-Gordon, *Molecular Physics*, 2015, **113**, 184–215.

[57] R. Fletcher and C. M. Reeves, *The Computer Journal*, 1964, **7**, 149–154.

[58] C. H. Choi, M. Kertesz and L. Mihaly, *The Journal of Physical Chemistry A*, 2000, **104**, 102–112.

[59] V. Schettino, M. Pagliai, L. Ciabini and G. Cardini, *The Journal of Physical Chemistry A*, 2001, **105**, 11192–11196.

[60] V. Schettino, M. Pagliai and G. Cardini, *The Journal of Physical Chemistry A*, 2002, **106**, 1815–1823.

[61] G. Sun and M. Kertesz, *The Journal of Physical Chemistry A*, 2002, **106**, 6381–6386.

[62] J. J. Adjizian, A. Vlandas, J. Rio, J.-C. Charlier and C. P. Ewels, *Philosophical Transactions of the Royal Society of London A: Mathematical, Physical and Engineering Sciences*, 2016, **374**, 20150323.

[63] H. Chen, M. R. Golder, F. Wang, R. Jasti and A. K. Swan, *Carbon*, 2014, **67**, 203–213.

[64] H. Chen, M. R. Golder, F. Wang, S. K. Doorn, R. Jasti, S. Tretiak and A. K. Swan, *The Journal of Physical Chemistry C*, 2015, **119**, 2879–2887.

[65] E. López-Chávez, A. Cruz-Torres, F. de Landa Castillo-Alvarado, J. Ortíz-López, Y. A. Peña-Castañeda and J. M. Martínez-Magadán, *Journal of Nanoparticle Research*, 2011, **13**, 6649–6659.

[66] M. Aydin and D. L. Akins, *Vibrational Spectroscopy*, 2010, **53**, 163–172.

[67] T. Kupka, M. Stachw, E. Chemecka, K. Pasterny and L. Stobiski, *Synthetic Metals*, 2012, **162**, 573–583.

[68] T. Yumura, D. Nozaki, S. Bandow, K. Yoshizawa and S. Iijima, *Journal of the American Chemical Society*, 2005, **127**, 11769–11776.

[69] T. Kupka, M. Stachow, L. Stobinski and J. Kaminsky, *Phys. Chem. Chem. Phys.*, 2016, **18**, 25058–25069.

[70] W. A. Saidi, *The Journal of Physical Chemistry A*, 2014, **118**, 7235–7241.

[71] S. Guha, J. Menéndez, J. B. Page and G. B. Adams, *Physical Review B*, 1996, **53**, 13106–13114.

[72] J. Kapitn, M. Dransk, J. Kaminsk, L. Benda and P. Bou, *The Journal of Physical Chemistry B*, 2010, **114**, 3574–3582.

[73] B. Nikoli, I. Miloevi and M. Damnjanovi, *The Journal of Physical Chemistry C*, 2014, **118**, 20576–20584.

[74] D. Kahn and J. P. Lu, *Physical Review B*, 1999, **60**, 6535–6540.

[75] H. A. Witek, S. Irle, G. Zheng, W. A. de Jong and K. Morokuma, *The Journal of Chemical Physics*, 2006, **125**, 214706.

[76] A. Rahmani, J.-L. Sauvajol, S. Rols and C. Benoit, *Physical Review B*, 2002, **66**, 125404.

[77] G. Wu, J. Zhou and J. Dong, *Physical Review B*, 2005, **72**, 115411.

[78] K. Sbai, A. Rahmani, H. Chadli, J. Bantignies, P. Hermet and J. Sauvajol, *The Journal of Physical Chemistry B*, 2006, **110**, 12388–12393.

[79] V. N. Popov, L. Henrard and P. Lambin, *Physical Review B*, 2005, **72**, 035436.

[80] V. N. Popov and P. Lambin, *physica status solidi (b)*, 2009, **246**, 2602–2605.

[81] H. Do and N. A. Besley, *Physical Chemistry Chemical Physics*, 2015, **17**, 3898–3908.

[82] R. L. Johnston and J. Fang, *The Journal of Chemical Physics*, 1992, **97**, 7809–7821.

[83] J.-Y. Fang, R. L. Johnston and J. N. Murrell, *Journal of the Chemical Society, Faraday Transactions*, 1993, **89**, 1659–1665.

[84] F. Gao, R. L. Johnston and J. N. Murrell, *The Journal of Physical Chemistry*, 1993, **97**, 12073–12082.

[85] N. A. Besley, R. L. Johnston, A. J. Stace and J. Uppenbrink, *Journal of Molecular Structure: THEOCHEM*, 1995, **341**, 75–90.

[86] J. E. Hearn, R. L. Johnston, S. Leoni and J. N. Murrell, *Journal of the Chemical Society, Faraday Transactions*, 1996, **92**, 425–432.

[87] L. D. Lloyd and R. L. Johnston, *Chemical Physics*, 1998, **236**, 107–121.

[88] H. Cox, R. L. Johnston and A. Ward, *Journal of Physics: Condensed Matter*, 1998, **10**, 9419.

[89] I. D. Hands, J. L. Dunn and C. A. Bates, *The Journal of Chemical Physics*, 2004, **120**, 6912–6921.

[90] F. Ercolessi and J. B. Adams, *EPL (Europhysics Letters)*, 1994, **26**, 583.

[91] H. Do and A. Troisi, *Physical Chemisty Chemical Physics*, 2015, **17**, 25123–25132.

[92] S. Grimme, *Journal of Chemical Theory and Computation*, 2014, **10**, 4497–4514.

[93] V. Schettino, M. Pagliai, L. Ciabini and G. Cardini, *The Journal of Physical Chemistry A*, 2001, **105**, 11192–11196.

[94] J. R. Sanchez-Valencia, T. Dienel, O. Gröning, I. Shorubalko, A. Mueller, M. Jansen, K. Amsharov, P. Ruffieux and R. Fasel, *Nature*, 2014, **512**, 61.

[95] V. Skakalova, J. Maultzsch, Z. Osvath, L. P. Biro and S. Roth, *Physica Status Solidi - Rapid Research Letters*, 2007, **1**, 138–140.

[96] N. Anderson, A. Hartschuh, S. Cronin and L. Novotny, *Journal of the American Chemical Society*, 2005, **127**, 2533–2537.

[97] M. Kalbac, L. Kavan, M. Zukalov and L. Dunsch, *Chemistry A European Journal*, 2006, **12**, 4451–4457.

[98] N. Souza, M. Zeiger, V. Presser and F. Mucklich, *RSC Adv.*, 2015, **5**, 62149–62159.

[99] M. Dresselhaus, G. Dresselhaus and M. Hofmann, *Vibrational Spectroscopy*, 2007, **45**, 71–81.

[100] C. Fantini, A. Jorio, M. Souza, M. S. Strano, M. S. Dresselhaus and M. A. Pimenta, *Physical Review Letters*, 2004, **93**, 147406.

[101] A. G. Souza Filho, S. G. Chou, G. G. Samsonidze, G. Dresselhaus, M. S. Dresselhaus, L. An, J. Liu, A. K. Swan, M. S. Ünlü, B. B. Goldberg, A. Jorio, A. Grüneis and R. Saito, *Physical Review B*, 2004, **69**, 115428.

[102] J. Maultzsch, H. Telg, S. Reich and C. Thomsen, *Physical Review B*, 2005, **72**, 205438.

[103] M. Dresselhaus, G. Dresselhaus, A. Jorio, A. S. Filho and R. Saito, *Carbon*, 2002, **40**, 2043–2061.

[104] S. Piscanec, M. Lazzeri, J. Robertson, A. C. Ferrari and F. Mauri, *Physical Review B*, 2007, **75**, 035427.

[105] M. S. Dresselhaus and P. C. Eklund, *Advances in Physics*, 2000, **49**, 705–814.

[106] Y.-J. Kang, J. Kang and K. J. Chang, *Phys. Rev. B*, 2008, **78**, 115404.

[107] X. F. Fan, W. T. Zheng, V. Chihaia, Z. X. Shen and J.-L. Kuo, *Journal of Physics: Condensed Matter*, 2012, **24**, 305004.

[108] A. Stone and D. Wales, *Chemical Physics Letters*, 1986, **128**, 501–503.

[109] Y. Miyamoto, A. Rubio, S. Berber, M. Yoon and D. Tománek, *Physical Review B*, 2004, **69**, 121413.

[110] S. K. Jain, G. T. Barkema, N. Mousseau, C.-M. Fang and M. A. van Huis, *The Journal of Physical Chemistry C*, 2015, **119**, 9646–9655.

[111] G. Wu and J. Dong, *Physical Review B*, 2006, **73**, 245414.

[112] P. M. Tailor, R. J. Wheatley and N. A. Besley, *Carbon*, 2017, **113**, 299 – 308.

[113] J. Li, C. Papadopoulos and J. Xu, *Nature*, 1999, **402**, 253˙–.

[114] S. Melchor and J. A. Dobado, *Journal of Chemical Information and Computer Sciences*, 2004, **44**, 1639–1646.

[115] S. N. Naess, A. Elgsaeter, G. Helgesen and K. D. Knudsen, *Sci Technol Adv Mater*, 2009, **10**, 065002.

[116] L. R. Baylor, V. I. Merkulov, E. D. Ellis, M. A. Guillorn, D. H. Lowndes, A. V. Melechko, M. L. Simpson and J. H. Whealton, *Journal of Applied Physics*, 2002, **91**, 4602–4606.

[117] C. Qu, L. Qiao, C. Wang, S. Yu, Q. Jiang and W. Zheng, *Physics Letters A*, 2010, **374**, 782–787.

[118] A. G. Cano-Marquez, W. G. Schmidt, J. Ribeiro-Soares, L. Gustavo Cançado, W. N. Rodrigues, A. P. Santos, C. A. Furtado, P. A. S. Autreto, R. Paupitz, D. S. Galvão and A. Jorio, *Scientific Reports*, 2015, **5**, 10408.

[119] C. J. L. Elias, M. Hudson, R. Cassiano, S. Emil, P. Sugandha, R. Juha, C. A. G. and J. Ado, *Journal of Raman Spectroscopy*, **49**, 54–65.

[120] C. Li and T. W. Chou, *International Journal of Solids and Structures*, 2003, **40**, 2487–2499.

[121] A. N. Khlobystov, D. A. Britz and G. A. D. Briggs, *Accounts of Chemical Research*, 2005, **38**, 901–909.

[122] J. Kotakoski, A. V. Krasheninnikov and K. Nordlund, *Physical Review B*, 2006, **74**, 245420.

[123] F. Ding, *Physical Review B*, 2005, **72**, 245409.

[124] A. Santana, A. M. Popov and E. Bichoutskaia, *Chemical Physics Letters*, 2013, **557**, 80–87.

[125] M. Dresselhaus, G. Dresselhaus and M. Hofmann, *Vibrational Spectroscopy*, 2007, **45**, 71–81.

[126] C. Y. Guo, B. M. Pettitt and L. T. Wheeler, *Molecular Simulation*, 2006, **32**, 839–848.

[127] S. B. Cronin, A. K. Swan, M. S. Ünlü, B. B. Goldberg, M. S. Dresselhaus and M. Tinkham, *Physical Review Letters*, 2004, **93**, 167401.

[128] S. B. Cronin, A. K. Swan, M. S. Ünlü, B. B. Goldberg, M. S. Dresselhaus and M. Tinkham, *Physical Review B*, 2005, **72**, 035425.

[129] U. Venkateswaran, E. Brandsen, U. Schlecht, A. Rao, E. Richter, I. Loa, K. Syassen and P. Eklund, *physica status solidi (b)*, 2001, **223**, 225–236.

[130] A. G. Souza Filho, N. Kobayashi, J. Jiang, A. Grüneis, R. Saito, S. B. Cronin, J. Mendes Filho, G. G. Samsonidze, G. Dresselhaus and M. S. Dresselhaus, *Physical Review Letters*, 2005, **95**, 217403.

[131] X. Duan, H. Son, B. Gao, J. Zhang, T. Wu, G. G. Samsonidze, M. S. Dresselhaus, Z. Liu and J. Kong, *Nano Letters*, 2007, **7**, 2116–2121.

[132] Z. Liu, J. Zhang and B. Gao, *Chemical Communications*, 2009, 6902–6918.

[133] M. J. Peters, L. E. McNeil, J. P. Lu and D. Kahn, *Physical Review B*, 2000, **61**, 5939–5944.

[134] J. Sandler, M. S. P. Shaffer, A. H. Windle, M. P. Halsall, M. A. Montes-Morán, C. A. Cooper and R. J. Young, *Physical Review B*, 2003, **67**, 035417.

[135] M. Lucas and R. J. Young, *Physical Review B*, 2004, **69**, 085405.

[136] C. Li and T.-W. Chou, *Composites Science and Technology*, 2003, **63**, 1517–1524.

[137] F. Darkrim, P. Malbrunot and G. Tartaglia, *International Journal of Hydrogen Energy*, 2002, **27**, 193–202.

[138] T. A. Saleh and V. K. Gupta, *Journal of Colloid and Interface Science*, 2012, **371**, 101–106.

[139] J. Zhao, A. Buldum, J. Han and J. P. Lu, *Nanotechnology*, 2002, **13**, 195.

[140] A. Govindaraj, B. C. Satishkumar, M. Nath and C. N. R. Rao, *Chemistry of Materials*, 2000, **12**, 202–205.

[141] Y. Zhou, S. Sreekala, P. M. Ajayan and S. K. Nayak, *Journal of Physics: Condensed Matter*, 2008, **20**, 095209.

[142] *Proceedings of the Royal Society of London A: Mathematical, Physical and Engineering Sciences*, 1924, **106**, 463–477.

[143] S. Grimme, *Journal of Computational Chemistry*, 2004, **25**, 1463–1473.

[144] X. Luo, X. Lu, C. Cong, T. Yu, Q. Xiong and S. Ying Quek, *Scientific Reports*, 2015, **5**, 14565.

[145] S. Grimme, *Journal of Computational Chemistry*, 2006, **27**, 1787–1799.

[146] A. Bondi, *The Journal of Physical Chemistry*, 1964, **68**, 441–451.

[147] S. Latil, V. Meunier and L. Henrard, *Phys. Rev. B*, 2007, **76**, 201402.

[148] K. F. Mak, M. Y. Sfeir, J. A. Misewich and T. F. Heinz, *Proceedings of the National Academy of Sciences*, 2010, **107**, 14999–15004.

[149] R. Sharma, J. H. Baik, C. J. Perera and M. S. Strano, *Nano Letters*, 2010, **10**, 398–405.

[150] P. H. Tan, W. P. Han, W. J. Zhao, Z. H. Wu, K. Chang, H. Wang, Y. F. Wang, N. Bonini, N. Marzari, N. Pugno, G. Savini, A. Lombardo and A. C. Ferrari, *Nature Materials*, 2012, **11**, 294.

[151] C. H. Lui and T. F. Heinz, *Physical Review B*, 2013, **87**, 121404.

[152] M. L. Lin, J. B. Wu, X. L. Liu and P. H. Tan, *Journal of Raman Spectroscopy*, 2018, **49**, 19–30.

[153] S. Iijima, *Nature*, 1991, **354**, 56.

[154] X. Zhang, X. Zhang, G. V. Tendeloo, S. Amelinckx, M. O. de Beeck and J. V. Landuyt, *Journal of Crystal Growth*, 1993, **130**, 368–382.

[155] C. Schnenberger and L. Forr, *Physics World*, 2000, **13**, 37.

[156] J. Miyamoto, Y. Hattori, D. Noguchi, H. Tanaka, T. Ohba, S. Utsumi, H. Kanoh, Y. A. Kim, H. Muramatsu, T. Hayashi, M. Endo and K. Kaneko, *Journal of the American Chemical Society*, 2006, **128**, 12636–12637.

[157] F. Villalpando-Paez, H. Son, D. Nezich, Y. P. Hsieh, J. Kong, Y. A. Kim, D. Shimamoto, H. Muramatsu, T. Hayashi, M. Endo, M. Terrones and M. S. Dresselhaus, *Nano Letters*, 2008, **8**, 3879–3886.

[158] S. Lefrant, *Current Applied Physics*, 2002, **2**, 479–482.

[159] J. M. Benoit, J. P. Buisson, O. Chauvet, C. Godon and S. Lefrant, *Phys. Rev. B*, 2002, **66**, 073417.

[160] X. Zhao, Y. Ando, L.-C. Qin, H. Kataura, Y. Maniwa and R. Saito, *Physica B: Condensed Matter*, 2002, **323**, 265–266.

[161] C. H. Kiang, M. Endo, P. M. Ajayan, G. Dresselhaus and M. S. Dresselhaus, *Phys. Rev. Lett.*, 1998, **81**, 1869–1872.

[162] V. N. Popov and L. Henrard, *Phys. Rev. B*, 2002, **65**, 235415.

[163] J. Cumings and A. Zettl, *Science*, 2000, **289**, 602–604.

[164] C. Shen, A. H. Brozena and Y. Wang, *Nanoscale*, 2011, **3**, 503–518.

[165] K. Jensen, K. Kim and A. Zettl, *Nature Nanotechnology*, 2008, **3**, 533.

[166] A. Barreiro, R. Rurali, E. R. Hernández, J. Moser, T. Pichler, L. Forró and A. Bachtold, *Science*, 2008, **320**, 775–778.

[167] C. A. Schalley, K. Beizai and F. Vgtle, *Accounts of Chemical Research*, 2001, **34**, 465–476.

[168] M. H. Al-Saleh and U. Sundararaj, *Carbon*, 2009, **47**, 2–22.

[169] M. Endo, Y. A. Kim, M. Ezaka, K. Osada, T. Yanagisawa, T. Hayashi, M. Terrones and M. S. Dresselhaus, *Nano Letters*, 2003, **3**, 723–726.

[170] S. Lee, J. Park and S. Park, *International Journal of Hydrogen Energy*, 2014, **39**, 16468 – 16473.

[171] I. Y. Jang, H. Ogata, K. C. Park, S. H. Lee, J. S. Park, Y. C. Jung, Y. J. Kim, Y. A. Kim and M. Endo, *The Journal of Physical Chemistry Letters*, 2010, **1**, 2099–2103.

[172] A. N. Khlobystov, *ACS Nano*, 2011, **5**, 9306–9312.

[173] M. Endo, Y. A. Kim, T. Hayashi, Y. Fukai, K. Oshida, M. Terrones, T. Yanagisawa, S. Higaki and M. S. Dresselhaus, *Applied Physics Letters*, 2002, **80**, 1267–1269.

[174] Y. Sato, K.-I. Shibata, H. Kataoka, S.-I. Ogino, F. Bunshi, A. Yokoyama, K. Tamura, T. Akasaka, M. Uo, K. Motomiya, B. Jeyadevan, R. Hatakeyama, F. Watari and K. Tohji, *Mol. BioSyst.*, 2005, **1**, 142–145.